Iontronic Devices for Neuromorphic Computing and Health Monitoring

by

Qingzhou Wan

B.S. in Materials Science and Engineering, Wuhan University of Technology, 2015

M.S. in Materials Science and Engineering, University of Florida, 2017

Submitted to the Graduate Faculty of the

Swanson School of Engineering in partial fulfillment

of the requirements for the degree of

Doctor of Philosophy

University of Pittsburgh

2022

UNIVERSITY OF PITTSBURGH

SWANSON SCHOOL OF ENGINEERING

This dissertation was presented

by

Qingzhou Wan

It was defended on

June 22, 2022

and approved by

Kevin P. Chen, Ph.D., Professor, Department of Electrical and Computer Engineering

Jingtong Hu, Ph.D., Associate Professor, Department of Electrical and Computer Engineering

Nathan Youngblood, Ph.D., Assistant Professor, Department of Electrical and Computer Engineering

Ryad Benosman, Ph.D., Professor, Department of Ophthalmology, School of Medicine

Dissertation Director: Feng Xiong, Ph.D., Assistant Professor, Department of Electrical and Computer Engineering

Iontronic Devices for Neuromorphic Computing and Health Monitoring

Qingzhou Wan, Ph.D.

University of Pittsburgh, 2022

Iontronics is an emerging interdisciplinary field that bridges electronics and ionics, exploring the electronic properties or functions of the materials controlled by ionic movement and arrangement. Two intriguing mechanisms in iontronics are electrochemical charge doping and electrostatic effects at the electric-double-layer (EDL) interface, which can be leveraged to modulate the carrier density of low-dimensional materials and achieve the supercapacitance at the EDL interface. In this dissertation, we develop two types of iontronic devices: electrochemical synapses and supercapacitive pressure sensors for neuromorphic computing and health monitoring applications, respectively.

We first report three-terminal electrochemical synapses with programmable spatio-temporal dynamics using novel materials such as two-dimensional layered topological insulator $(Bi_xSb_{1-x})_2Te_3$ and perovskite tungsten trioxide. Inspired by the Li-ion battery, the channel conductance (i.e., synaptic weight) of the electrochemical synapses can be continuously and controllably modulated via electrochemical reactions (e.g., involving Li^+ ion flows) through a gate terminal. Our electrochemical synapses exhibit a large dynamic range, a high precision (multiple analog states), a linear and symmetric synaptic weight update, and small variations that are ideal for traditional artificial neural networks (ANNs). Additionally, time-dependent synaptic functions such as short-term and long-term plasticity, pair-pulse facilitation, and temporal filtering are demonstrated. The excellent energy efficiency and potential cognitive capabilities of our

electrochemical synapses could lead to the hardware acceleration of brain-inspired, neuro-realistic ANNs.

We also propose a high-fidelity iontronic tonometric sensor (ITS) with high sensitivity (4.82 kPa^{-1}), high linearity ($R^2 > 0.995$), and a large dynamic range (up to 180 % output change) over a broad working range (0-38 kPa) that can fully cover the normal blood pressure (BP) range (5-25 kPa). Our ITS demonstrates a low limit of detection at 40 Pa, a fast load (35 ms) and release time (35 ms), and a stable response over 5000 load/release cycles. We further explore the application of our ITS in monitoring real-time beat-to-beat BP by measuring the brachial and radial pulse waveforms. Our ITS work provides a rational design for a wearable pressure sensor with high sensitivity, high linearity, and a large dynamic range for real-time continuous and non-invasive BP monitoring.

Table of Contents

List of Tables

List of Figures

Preface

First, I really appreciate the unwavering support and patient advice from my advisor Prof. Feng Xiong, who has been inspiring consistent motivation and passion in me during my PhD research. Aside from his professional mentorship, I also would like to thank him for offering me precious life lessons and guidance in the past five years. It would not be possible for me to have arrived at this step without his generous and persistent help. Meanwhile, I greatly appreciate the financial support from our ECE department, the Mascaro Center for Sustainable Innovation, the Central Research Development Fund at Pitt, and the NSF that has enabled me to conduct this research.

Next, I would like to thank Prof. Kevin P. Chen, Prof. Jingtong Hu, Prof. Nathan Youngblood, and Prof. Ryad Benosman for serving on my committee and providing precious mentorship and advice.

I also would like to express great gratitude to my colleagues Mohammad T. Sharbati, Yanhao Du, John R. Erickson, Yihan Liu, and Xingyu Zhang. I will always remember in my heart that we worked hard together, had stimulating and inspirational discussions, and enjoyed all the fun and great moments at our best ages in college.

I sincerely thank my wife Xinruo for her warm love, companionship, and encouragement whenever I feel depressed or pessimistic. I am very lucky to have had her around since we met for the first time. I also would like to thank her for bringing Woody, our cute dog, into our home. He provides endless fun and love to me. Most importantly, I would like to express my greatest gratitude and appreciation to my parents, who have provided me the most unselfish love and unconditional support for my whole life.

1.0 Introduction

In this chapter, section 1.1 will present the iontronics fundamentals, including the focus of the iontronic devices in this dissertation: electrochemical synapses and supercapacitive pressure sensors. Section 1.2 will introduce the concept of neuromorphic computing and artificial neural networks (ANNs), and the requirements for the building blocks of the ANNs: artificial synapses. Section 1.3 will review various types of emerging artificial electronic synapses and list the special advantages of electrochemical synapses for ANNs. Section 1.4 will give a brief introduction to arterial blood pressure monitoring methods and present the sensor requirements for continuous, non-invasive applanation tonometry monitoring. Section 1.5 will review various types of flexible pressure sensors and their advantages for applanation tonometry monitoring.

1.1 Iontronics Fundamentals

1.1.1 What is Iontronics?

The term "Iontronics" is thought[1] to originate from the organic semiconductor community, first appearing in a 2016 book titled *Iontronics: Ionic Carriers in Organic Electronic Materials and Devices,* written by Janelle Leger, Magnus Berggren and Sue Carter.[2] In this book, the concept of iontronics only refers to ion-based organic electronics. However, with the fast development of emerging materials and devices, the concept of iontronics has since that original mention been extended to all related devices by which electronic properties or functions are

controlled by ionic movement and arrangement.[1, 3] This includes a large variety of devices consisting of any substances or materials, including electrochemical batteries, field-effect transistors, memory devices, light-emitting devices, sensors, actuators, thermoelectric devices, neuromorphic devices, and energy-harvesting devices. The typical materials for iontronics can be categorized into three types: electronic conductors (but ionic insulators), ionic conductors (but electronic insulators), and mixed ionic conductors (both electronic and ionic conductors). Electronic conductors commonly include conductive metals. Ionic conductors include ionic solutions, polymer electrolytes and polyelectrolytes, ceramics (oxides, sulfides, phosphates), ionic liquids, and ion gels.[1] Mixed ionic conductors include organic materials (conjugated polymers) and inorganic materials (transition metal chalcogenides, nonstoichiometric perovskite, layered oxides, oxyhydroxides).[4, 5]

The typical structure of iontronics consists of an ionic conductor layer sandwiched by two electronic conductors or mixed ionic conductors, as shown in **Figure 1.1**. Iontronic devices generally use one of two underlying mechanisms: electrochemical ion intercalation via redox reactions and electrostatic supercapacitive effects via EDL.[5, 6] Figure 1.1a illustrates the electrochemical ion intercalation and deintercalation (or ion insertion and extraction) processes. In these processes, the ions are transported and inserted (extracted) into (from) the layered host materials under external applied potential while the electrons from the external circuit compensate the host materials to reach charge neutrality. Figure 1.1b shows the electrostatic effects via EDL, similar to field-effects in traditional semiconductors, where a high density of carriers accumulates at the ionic/electronic interface, accompanied by an ultra-high electric field as well as a large capacitance at the EDL interface. By leveraging these two fundamental mechanisms, along with

different materials systems and device structure designs, we can design various iontronic devices aimed at different applications.

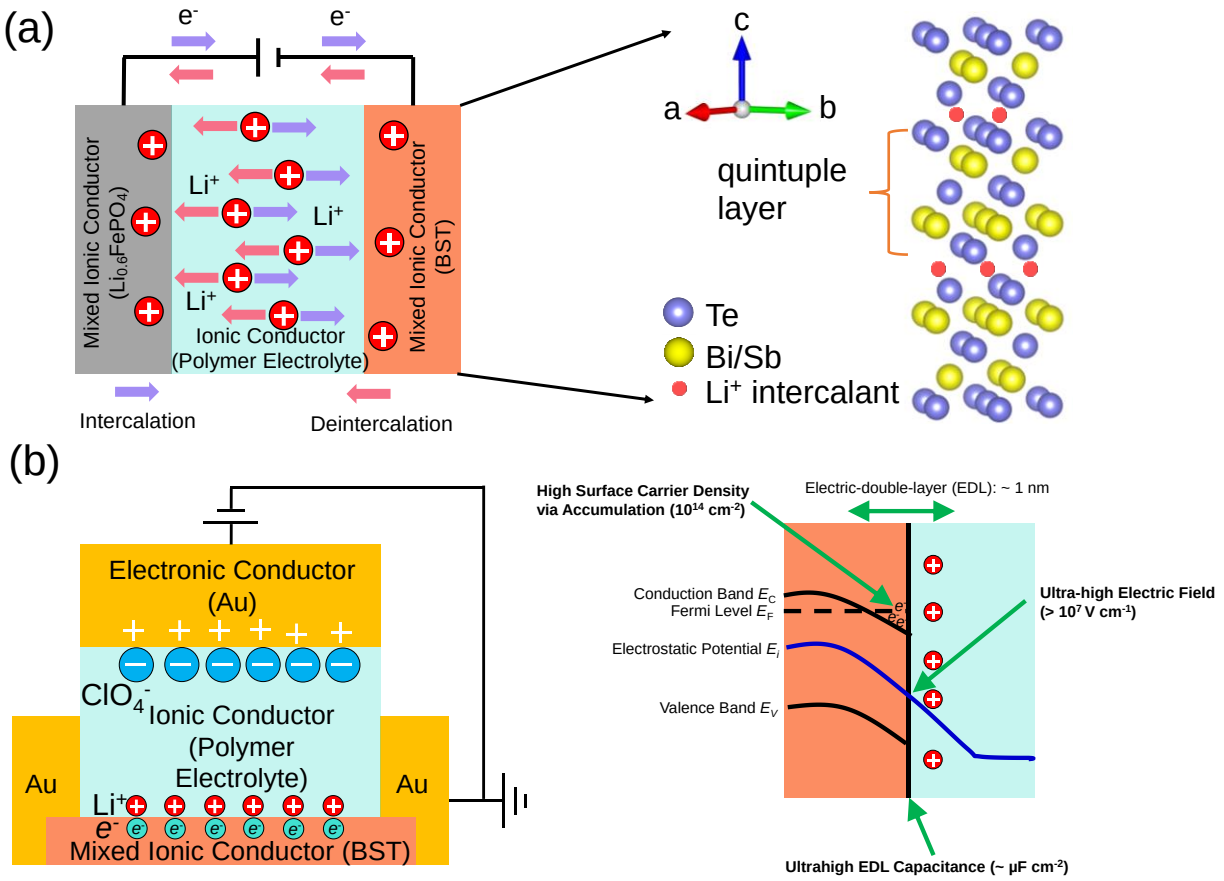

Figure 1.1. Iontronic underlying mechanisms. a) Electrochemical intercalation/deintercalation via redox reactions. b) Electrostatic effects via electric-double-layer.

1.1.2 Advantages of Solid-State Iontronic Devices

In this dissertation, solid-state iontronic devices refer to iontronics that work in solid-state environments, characterized by usage of ceramics (e.g., oxides, sulfides, phosphates), solid polymers, or broadly ionic gels as solid-state ionic conductors (electrolytes). Traditional liquid electrolyte-based devices usually suffer from safety issues (leakage, flammability) and low

stability.[4] By replacing the liquid electrolyte with the solid electrolyte, the iontronic devices are more practical and portable for use in ambient environments mainly due to the following advantages: 1) offering more convenience for encapsulation and packaging of the device; 2) avoiding usage of flammable or toxic aqueous solvents; 3) boosting thermal and mechanical stability; 4) providing better scalability and flexibility for device design; 5) enabling easier device characterization and testing; 6) facilitating the device integration with other solid-state systems; and 7) opening up more opportunities in flexible, wearable device applications.[1, 4] Though they offer numerous exciting advantages, it is very challenging to develop low-cost solid-state electrolytes that have high ionic conductivity and mobility at room temperature, easy processibility, cheap deposition techniques, and excellent compatibility with complementary metal-oxide semiconductor (CMOS) fabrication. However, different approaches combining the use of inorganic ceramics and organic polymers to form composite electrolytes have great potential to overcome the bottlenecks in current solid-state electrolytes.[4]

1.1.3 The Focus of Iontronic Devices in This Dissertation

In this dissertation, we will focus on developing innovative iontronic devices such as electrochemical synapses or electrochemical random access memory (ECRAM) and wearable supercapacitive sensors, aiming for applications in neuromorphic computing and blood monitoring, respectively.

Recently, emerging three-terminal electrochemical redox transistors, or ECRAM, have become a promising candidate for mimicking biologic synapses due to their low power, high precision, linear and symmetric response, low variation, and good endurance performance.[7-14] The channel conductance (i.e., synaptic weight) of the electrochemical synapses can be

continuously and controllably modulated via electrochemical reactions (e.g., involving Li^+ or H^+ ion flows) through a gate terminal. In addition, the three-terminal configuration of these transistors enables the decoupling of the energy barrier for retention and programming,[12] hence leading to both good retention and low-power programming, an accomplishment that is difficult to achieve in two-terminal memory devices such as RRAMs.[15, 16] While the Li^+ ion in the gel electrolyte could potentially be a source of contamination for CMOS fabrications, it is a good material for proof-of-concept of our electrochemical redox transistors due to its well-known electrochemical behaviors. Our developed electrochemical synapses exhibit excellent spatio-temporal dynamics, opening up great possibilities for bio-inspired and cognitive computing.

We have also developed wearable supercapacitive sensors for health monitoring. A new type of sensing mechanism, known as supercapacitive or iontronic sensing, has been developed to achieve high fidelity and high sensitivity in pressure sensors.[17-19] Previously, to amplify the sensing signal and enhance sensitivity, organic field-effect transistors[20, 21] or two-dimensional transistors[22] have been utilized coupled with piezocapacitive sensors. However, those transistor-based piezocapacitive devices require complex fabrication and device integration methods. Iontronic sensors, replacing the conventional dielectric layer with an ionic film, take advantage of the supercapacitive nature of the EDL at electrolytic-electronic interface[23] and exhibit ultrahigh unit area capacitance (UAC), which is on the order of several $\mu F\ cm^{-2}$ (1000 times higher than that of traditional piezocapacitive sensors). This ultrahigh UAC improves the sensing signal-to-noise ratio, increases immunity to external electromagnetic and transmission line noises, and boosts sensitivity. Our work in wearable sensors provides a rational design for a flexible pressure sensor with high sensitivity, high linearity, and a large dynamic range for real-time continuous and non-invasive blood pressure monitoring.

1.2 Neuromorphic Computing and Artificial Neural Networks

As transistor technology has moved closer and closer to the limits of Moore's law, the need for next generation devices with higher performance and better energy efficiency has rapidly increased. With this in mind, researchers have turned their attentions to mimicking the performance of the most efficient known computational entity, the human brain. The human brain excels at complex cognitive tasks, such as pattern recognition and all of the constant small calculations needed to keep a body functioning through everyday life, and all of this with an energy consumption as low as 20 W.[24] In contrast, the number one publicly reported super computer at Oak Ridge National Laboratory (as of 2018) uses an astonishing 9.78 MW of power.[25] Both of these offer computational capabilities on the peta-flop scale, making the brain a truly extraordinarily efficient device.[24]

One of the major causes of the disparity in energy usage is what is referred to as the von Neumann bottleneck.[26] In modern computing systems, the dedicated central processing units (CPUs) are physically separated from the main memory areas. In addition, these CPUs are programmed to execute operations sequentially, where relevant information needs to be shuttled back and forth between the CPU and the memory.[27] This shuttling of bits not only puts an inherent cap on the speed of computations, but also drastically increases energy usage.

In contrast, biological and biologically inspired systems use synapses that are capable of both storing information and performing complex operators at the same location.[28] This property enables biological systems to carry out computations in massively parallel networks, reducing the energy cost per operation. Hence, researchers are motivated to develop neuromorphic computing systems that can rival or even exceed the cognitive capabilities and energy efficiency of the human brain.

In this pursuit, ANNs have been developed and successfully applied in various fields including: image and pattern recognition,[29] speech recognition,[30] machine translation,[31] and beating humans at chess and, more recently, Go.[32] Despite these recent strides in neuromorphic computing, the hardware implementation of these ANNs has been hampered by the fact that the digital transistors, the basic computing unit of modern computers, do not behave in the same manner as analog synapses, the basic building block of the biological neural network.

In the following sections, we will review the basic neural network operations including neuromorphic computation, deep neural networks (DNNs) and spiking neural networks (SNNs), followed by a review of a number of different approaches currently being investigated that aim to improve the performance of synaptic devices towards the hardware acceleration of ANNs. After that, we will introduce numerous types of emerging artificial electronic synapses including PCM-based synapses, RRAM-based synapses, Electrochemical synapses and 2D materials-based synapses. Finally, we will finish this chapter with a comparison of different device metrics and specifically introduce the advantages of electrochemical synapses based on 2D materials.

The human brain presents an interesting computing model, made up of extremely dense networks of computing elements (neurons) with versatile memory elements (synapses), all operating at extremely low power levels.[33] The human brain has ~10^{11} neurons, with a corresponding ~10^{15} total synapses.[34] A single neuron in the brain can have around 10,000 inputs/outputs to other neurons in the brain through synapses.[33] The neuron is composed of many different parts, as demonstrated in **Figure 1.2**. The soma makes up the main body of the neuron and is connected to the network via dendrites and an axon. Dendrites are responsible for receiving information from other neurons (inputs) and the axon, with its terminal branches, is responsible for transmitting information out (output). The synapses are small (20-40 nm) gaps between the

axon end of the previous neuron and the dendrites of the next neuron. The "weight" of the synapse, i.e., the connection strength between neurons, can become stronger (potentiation) or weaker (depression) through a process called synaptic plasticity, as the brain adapts to new information. As synaptic plasticity is widely believed to dictate the learning and memory processes in the brain, mimicking the weight update during learning epochs is at the heart of neuromorphic computing.

When a neuron is excited, it will release a signal (pulse) that will travel down the axon and through the synapses into the dendrites of the next neurons. The amount of this signal that makes it to the next neuron is dependent on the strength of these connections (synaptic weight). If the neuron has enough input signal, it too fires, propagating the signal throughout the network.

In order to implement an ANN that can be scaled up, many systems adopt a crossbar synaptic array structure, as pictured in Figure 1.2. Each input line is connected to output lines through programmable resistors, as such the total output of each line is influenced by each input. It is these connection resistors (synaptic devices) that determine how much of the input signal goes to each output signal. Modern arrays also include different selection devices, to prevent errors arising from so called sneak currents falsely influencing the output.[35]

Extensive research efforts have been devoted to optimizing the performance of these synaptic devices and building the best neuromorphic system possible. Towards that end, we will briefly review the operating principles behind ANNs, as well as discuss the device characteristics that impact the performance of these networks.

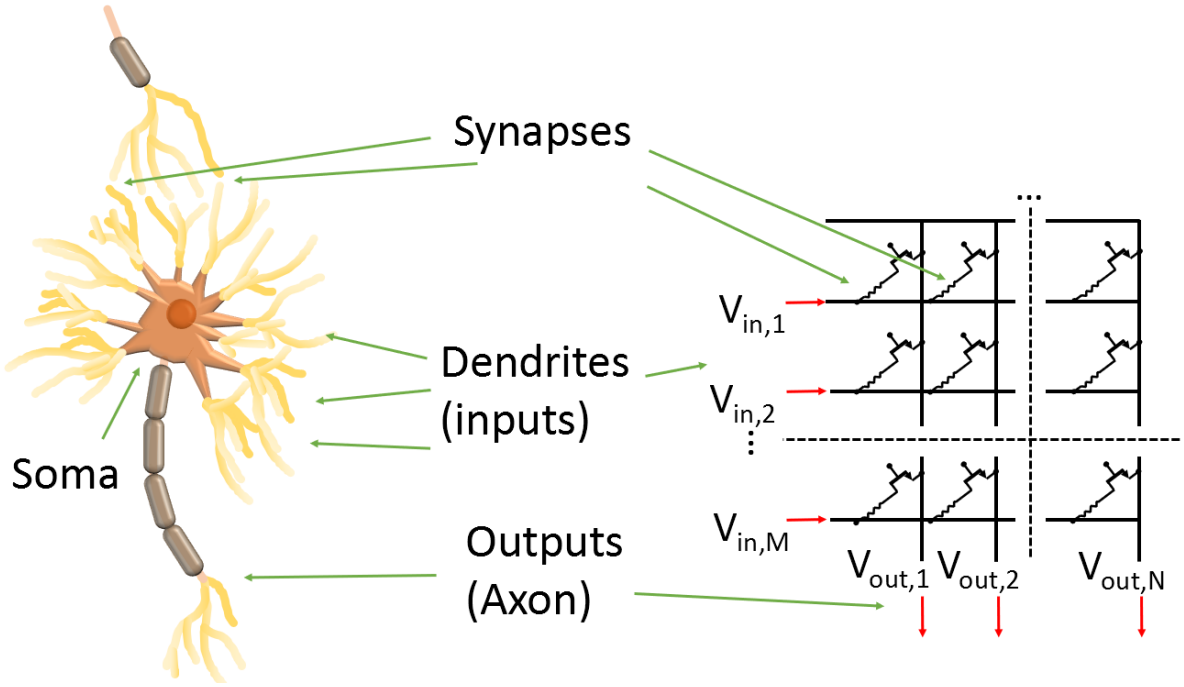

Figure 1.2. Comparison of biological and artificial neurons. Schematics of a biological neuron (left) vs. an artificial neural network (right).

1.2.1 Neuromorphic Computation

To illustrate how ANNs perform their computations, we use a simple example here on the recognition of handwritten digits through a basic feed-forward network, as shown in **Figure 1.3**. The initial image is broken up into N binary inputs (black or white), each corresponding to a specific area of the image, which are then put through one hidden layer, where the computation takes place. Each input element here is connected to each of the M hidden neurons, just as each hidden neuron is connected to each of the 10 output neurons.

The total inputs into a neuron is summed and if the amount of signal input passes a SET threshold, then that neuron propagates its signal down into the next layer. This happens in each layer of the network until eventually it hits the output layer, in this case 10 output neurons

corresponding to the digits zero through nine. Depending on which final neuron fires, the system can detect which digit is in the initial image.

The important concept here then is how to determine the threshold on the amount of input that a neuron needs to fire, as well as how to determine the connection strength between the neurons, i.e., the synaptic weight. This weight is what determines how much of each input signal gets distributed through to each neuron in the next layer. These synaptic weights can then be trained through different algorithms, usually by putting a large series of known data into the system and adjusting the relevant synaptic weights until the output is the known correct output. This method is known as offline learning, and while successful, it has some drawbacks. Mostly, there needs to be an already established, extensive data sets need to be fed into the networks, and the training process can take lots of time. Another method of training called online training does exist that is used for data sets that are more dynamic.This type of network is being trained as the data comes in. However this process needs extensive peripheral circuits to perform the large number of weight update calculations in real time as well as more on-chip memory to store the new weight values.[36] Since the synapses are typically updated more often on-the-fly, synaptic devices used for online training have higher endurance requirements. In addition, these devices should also have a large number of conductance states with a preferably linear weight change characteristic to make it easier for the network to converge to an error minima.

Once training is complete, the network will be able to operate on its own, with varying degrees of success depending on the efficiency of the training scheme. There are several different ways to train the network, both online or offline, depending on the network type and what the intended task is.[37] Of the many different network types, most fall under two major categories: DNNs and SNNs. DNNs have been shown to be powerful in many applications such as image

classification and speech recognition; SNNs are a burgeoning field. They resemble biological neural systems more closely with the hope that they can be used to push ANNs to their maximum potential.

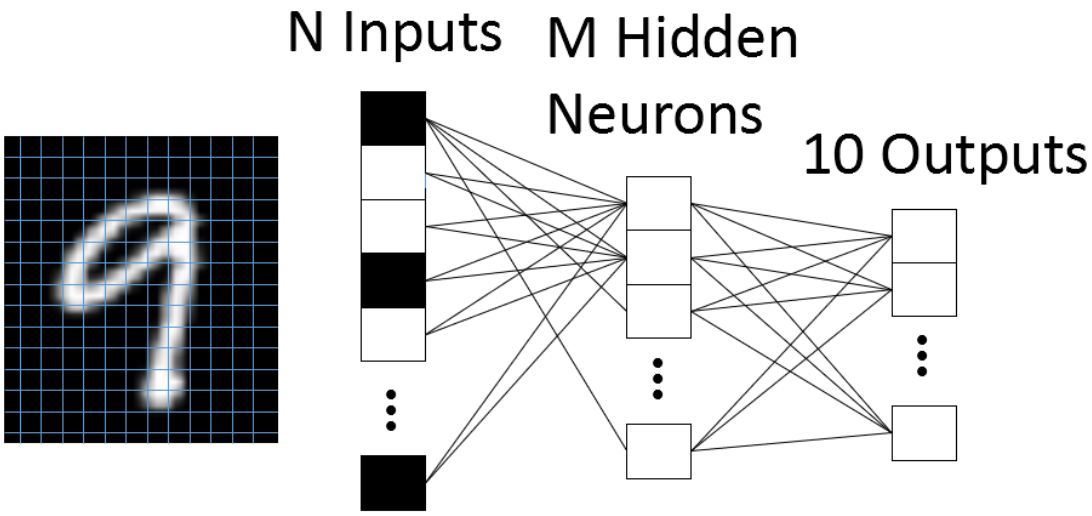

Figure 1.3. Simple pattern recognition example. 2-Layer multilayer perceptron example of a simple network structure for handwritten digits recognition. The image is broken into a grid of N total areas, (the N input elements) those elements are all connected into a Hidden Neuron layer of size M, and those Hidden Neurons are then connected to the 10 Output Neurons, representing the digits 0-9. Reproduced with permission.[38] Copyright 2017, IEEE.

1.2.2 Deep Neural Networks (DNNs)

The original work for neural networks was developed by McCulloch and Pitts in 1943, and was implemented in the first perceptron in 1958.[39] However, due to the lack of computing power at the time, these first devices were largely forgotten until the 1980s. With the discovery of error backpropagation techniques as well as the chain rule, neural networks were able to steadily increase in accuracy and sophistication through the end of the 20th century.[39]

With the advent of modern computational power in the early 21st century, DNNs (Multilevel Perceptrons, Deep Belief Networks, Convolutional Neural Networks etc.) rapidly exploded as the driving force behind modern day neural network advances. DNNs are networks with a large amount of complexity along with many layers. These networks were capable of supervised, semi-supervised and unsupervised learning, and excelled in tasks that had large amounts of training data.[39] Furthermore, with the recent commercial availability of powerful parallel computation devices like graphic processor units (GPUs) and field programmable gate arrays (FPGAs), the field of DNN has blossomed as researchers develop new learning algorithms as well as network structures.[40]

However, as DNNs continued to progress, it requires a huge amount of computational resources for the training, due to the rise of its complexity. As such, extensive research efforts have been devoted into the development of custom-designed DNN accelerators. By using on-chip buffers, current CMOS devices are employed to fabricate certain DNN accelerators.[41] However, the scalability of these solutions remains in question as the amount of needed memory devices, typically static random access memories (SRAMs), is quite large. Not only do these memory devices drastically increase the size of the device (as each SRAM cell consists of eight transistors) but the energy efficiency of the chip is low due to the power consumed by the leakage current in the memory devices.[41] In order to advance the existing DNN schemes, further progress on synaptic devices are necessary to provide the device density as well as energy efficiency needed to rival human cognitive capabilities.

1.2.3 Spiking Neural Networks (SNNs)

SNNs have recently attracted a lot of attention due to their close similarity to biological systems. In SNNs, the input signals are spikes, rather than the constant feed found in traditional neurons. Being able to process spikes is widely believed to be one of the main reasons that the brain is so spectacular at sequence recognition as well as memory.[42] Sequence recognition is one of the more important topics in computing, as it directly impacts the system's capabilities of working with stimuli that are strongly timing dependent, such as speech recognition and image detection.[43]

In order to make SNNs a reality, there needs to be a method in place to govern spike-timing-dependent plasticity (STDP), which is postulated to be what governs causality in the brain. If one event seems to cause/correlate another event multiple times, this causality/correlation is reinforced in the brain through changes of synaptic connections,[44] as summarized by the quote from Löwel and Singer – "neurons that fire together, wire together."[45] Consider a single post synaptic neuron, with a pre-synaptic neuron in the layer behind it, as shown in **Figure 1.4a**. If the pre-synaptic neuron continuously fires before the considered post-synaptic neuron, then it would seem that the pre-synaptic neuron has a direct effect on whether or not the post synaptic neuron fires, and the connection between the two would be strengthened (excitatory) or weakened (inhibitory), depending on the type of the synapse However, if the post-synaptic neuron continuously fires before the pre-synaptic neuron does, then it would seem that that pre-synaptic neuron has no effect on the considered post-synaptic neuron and that connection should be weakened (excitatory) or strengthened (inhibitory). Different forms of STDP and the associated synaptic weight change are depicted in Figure 1.4b. In addition to STDP, other factors such as

firing rate, spiking orders, and dendritic locations have shown to affect plasticity in the brain as well.[46]

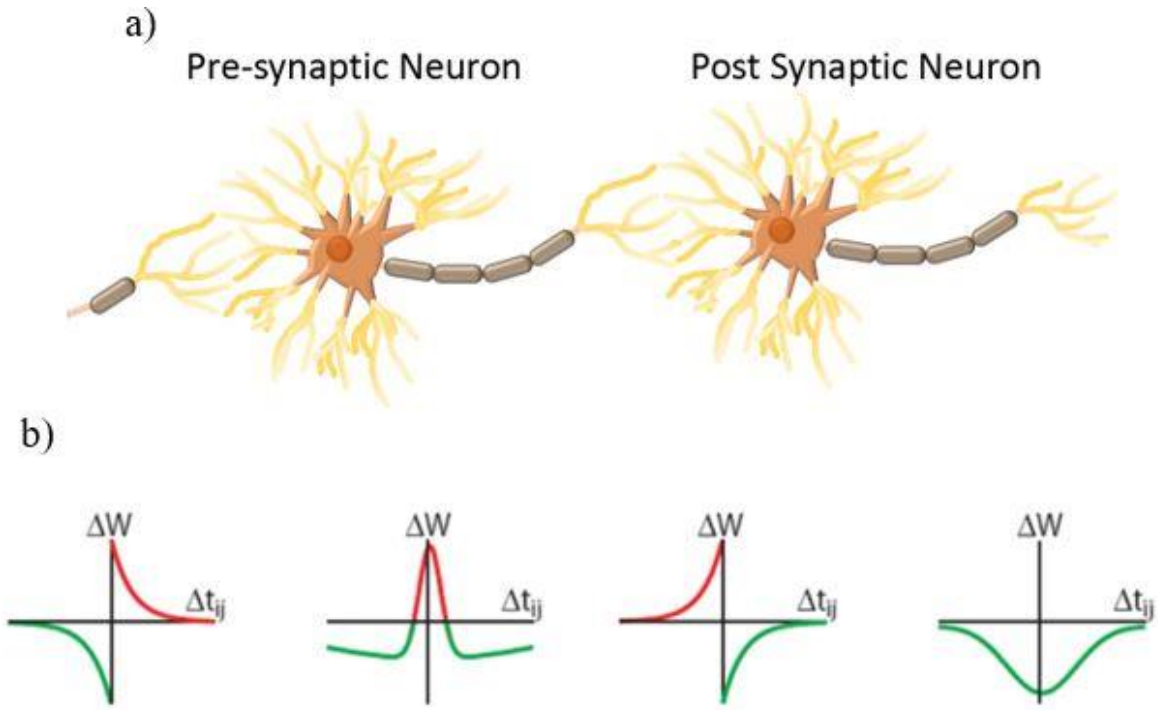

Figure 1.4. Spike-timing-dependent plasticity (STDP) models. a) Example of a neuron (Neuron A) with its prior neuron layer (Neuron B). b) Examples of STDP desired weight change based on the time difference between Neuron A and Neuron B firing. Reproduced with permission.[47] Copyright 2018, John Wiley and Sons.

Like DNNs, there have been several approaches to building SNNs, depending heavily on the desired application as well as the type of synaptic device involved.[48] However, all of these traditional techniques require strict timing mechanisms, as well as extraneous peripheral circuity to accomplish. These peripheral circuits not only require large physical chip areas, but also demand massive amounts of memory, making the scalability of these circuits unrealistic.[48] As such, there

has been a need for a new type of synaptic device that can inherently incorporate STDP like characteristics for the implementation of the next generation of SNNs.

1.2.4 Existing Approaches and Synaptic Device Requriements

There have been a number of existing neuromorphic systems adopted for the hardware acceleration of ANNs. TrueNorth is a DNN system, which uses 4096 CMOS-based neurosynaptic cores.[49] These cores form a total of 1 million neurons and 256 million synapses and are capable of a reported 58 G-synaptic operations per second (GSOPS). While its power efficiency is decent at ~2.5 pJ/op, there is still lots of room for improvement when compared to the human brains, which are reported at ~2 fJ/op.[49, 50] SpiNNaker, on the other hand, is a SNN based system.[51] It uses 18 general purpose CPUs which can each model a few hundred neurons. Each of these neurons has synapses numbering on the order of 1000, although software considerations take up a significant portion of the computing resources. While SpiNNaker doesn't have the same raw computational power of other systems, it excels at training speed. SpiNNaker is designed to efficiently simulate large scale SNNs in real time, whereas other spiking systems might take hours if not days to be trained and start running.[52]

However, as discussed in previous sections, due to their dependence on traditional digital CMOS technology, these systems have difficultly scaling up their sizes due to constraints in power and area. In this vein, researchers are actively working on the development of synaptic devices for the hardware implementation and acceleration of ANNs.

Many synaptic devices have been proposed in recent years with varying device properties. At a first glance, synaptic devices share a lot of common properties with emerging non-volatile memories (NVMs) as both devices need to facilitate programming, reading, and retention of

information. That is why emerging NVMs such as PCM, RRAM, and spin-torque transfer random access memory (STT-RAM) have been adopted as synaptic devices, as some of the preferred metrics of NVMs such as low programming energy, fast switching speed, good scalability etc. are equally useful for artificial synapses.[38] However, synaptic devices and NVMs are geared towards different applications and therefore have different (or even conflicting) requirements in many device metrics. Most notably, NVMs typically are designed to be binary or multi-level cells (MLC) with no more than 8 states (i.e. 3 bits) per device, whereas an artificial synapse requires much higher precisions (~8-bit or 256 states per device) to achieve the desired learning accuracy and device density. Another example is that even though a high on/off ratio is always preferred to improve the signal-to-noise ratio in NVMs, an unusually large on/off ratio can potentially result in low sensitivity to individual synapses in larger arrays. In addition, certain traits that are inconsequential in NVMs may play important roles in an ANNs. For example, linearity and symmetry of the current-voltage (*I*-*V*) characteristics do not affect the performance in NVMs but can dictate the learning accuracy in DNNs. Requirements on endurance and retention of the synaptic devices are application-dependent. A neural network that is trained online and performs weight update on-the-fly needs good endurance and is less stringent on retention performance. On the other hand, an offline neural network with presynaptic weights requires better long-term retention behavior with less emphasis on the endurance.

Now that the basic operating principles of different types of neural networks have been established, the types of synaptic devices being developed can now be discussed. The major types of device we will focus on are PCMs, RRAMS (including conductive-bridging, filamentary, and interfacial), electrochemical based, and finally synapses based on 2D materials. Each of these devices will have their working principles presented, as well as reported device metrics from recent

literature that assess their capability of being incorporated into existing ANN frameworks: operating speed and energy, precision (number of analog states), the degree of symmetry and linearity of the state switching, reliability (device variations, endurance, and retention), and finally their potential in spatio-temporal dynamics for SNNs.

1.3 Emerging Artificial Electronic Synapses

1.3.1 Phase Change Memory (PCM)

PCM has recently emerged as a promising NVM technology with its fast programming speed, good scalability, and high packing density.[53-58] **Figure 1.5a** shows a typical PCM mushroom cell (or T-cell), where the phase change material between the electrodes can be reversibly switched between a crystalline phase (i.e. low resistance state or LRS) and an amorphous phase (i.e. high resistance state or HRS) via Joule heating.[59] The concept of using phase change materials for memory application was originally proposed by Ovshinsky in 1969,[60] but it was the discovery of a family of fast switching (<100 ns) chalcogenides (Ge, Sb, and Te alloys) by Yamada et al. (Figure 1.5b),[61] which prompted the commercialization of PCM based optical data storage (DVDs and blu-rays) in 1990s and subsequently the development of electrically programmable phase change random access memory.[62] During the SET step (Figure 1.5c),[63] an applied electric field induces the threshold switching (a sudden increase in electrical conductivity) in amorphous phase change materials and subsequently heats up the cell to above its crystallization temperature (typically ~150 °C)[64] via Joule heating, inducing an amorphous (HRS) to crystalline (LRS) transition. In the RESET step, an even higher current density is needed to heat

up the cell to above its melting temperature, usually >650 °C.[65] This is then followed by a fast quenching step to freeze the molten material back to the amorphous phase. The SET process is the rate limiting step in PCM since the crystallization process involves atomic movement; whereas RESET is the power limiting step as the cell needs to be heat up to its melting temperature.

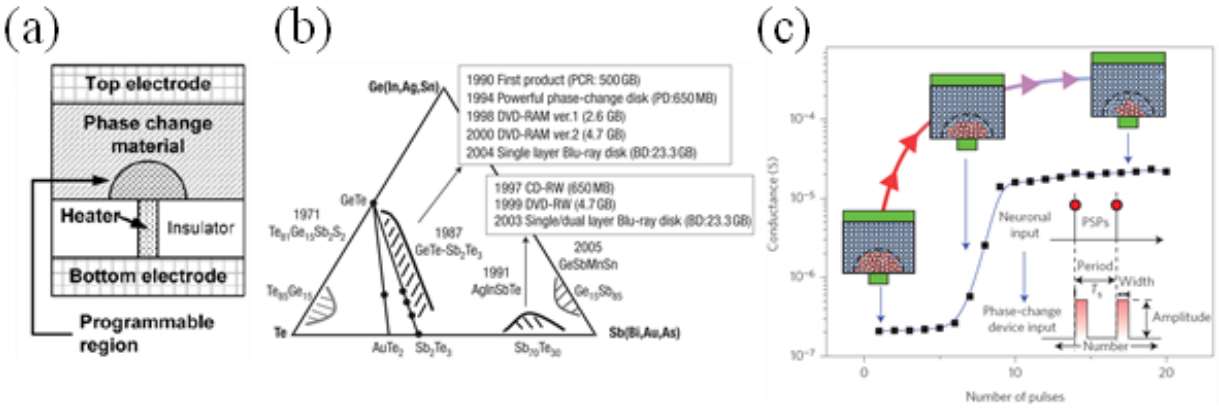

Figure 1.5. PCM synapse. a) The cross-section schematic of the mushroom PCM device. b) The family tree of fast switching chalcogenides. c) The schematic for implementing synaptic plasticity in PCM synapses. a) Reproduced with permission.[59] Copyright 2010, IEEE. b) Reproduced with permission.[61] Copyright 2007, AIP. c) Reproduced with permission.[63] Copyright 2016, Nature.

Recently, PCM has been employed as artificial synapses for the hardware acceleration of ANNs due to its fast speed, good scalability, and its potential for analog switching. To implement synaptic plasticity, various pulsing schemes (**Figure 1.6a**) have been explored to program the PCM cell into intermediate states, where the device conductance (synaptic weight) can be modulated by tuning the ratio of the amorphous (resistive) and crystalline (conductive) phases in the cell.[63] Figure 1.6b shows the cross-section transmission electron microscopy (TEM) images of PCM cell in its fully SET, partially RESET, and fully RESET states.[34, 66] This concept has been utilized for multi-level cell operation in PCM devices to improve the array density for NVM applications, but

a higher precision (# of levels per device) is needed for synaptic devices. An earlier study by Wright et al. reported PCM synaptic devices based on $Ge_2Sb_2Te_5$ (GST) with 10 levels per device (**Figure 1.7a**) and a dynamic range of 50×.[67] Zhong et al. demonstrated similar results in their GST synapses (Figure 1.7b) with a dynamic range of 5× and 10× levels per device.[68] In 2012, Kuzum et al. were able to push the precision level in their GST synapses to over 120 states per device (equivalent to 7-bit per device), while maintaining a good dynamic range (~50×) by using pulse trains with increasing amplitudes (Figure 1.7c).[66] This significant increase in precision level boosted the prospect of using PCM synapses for the hardware implementation of neural networks. However, while the conductance response in these PCM shows decent symmetry, it is highly non-linear with large variations owing to the stochastic nature of the crystallization and melt-quench processes, which negatively affects the learning performance in PCM synaptic arrays.[69-72]

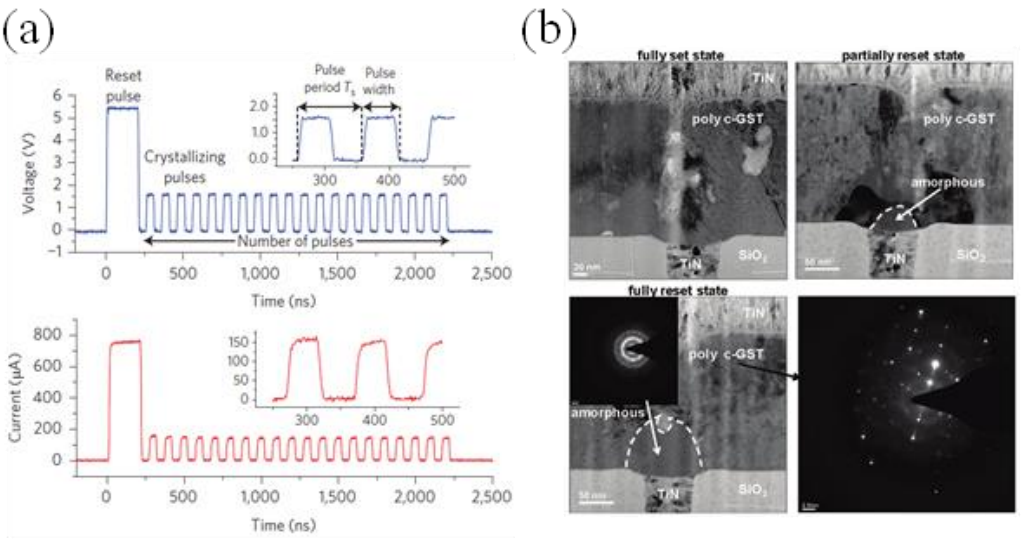

Figure 1.6. Set and reset in PCMs. a) A series of set pulses with low amplitude for set cycle and single high amplitude pulses required for reset cycle in blue (top), and corresponding set and reset current in red (bottom). b) TEM images illustrating the phase transition from fully set state to partially reset state with small amorphous region shown by small mushroom, and fully reset state. a) Reproduced with permission.[63] Copyright 2016, Nature. b) Reproduced with permission.[66] Copyright 2012, ACS.

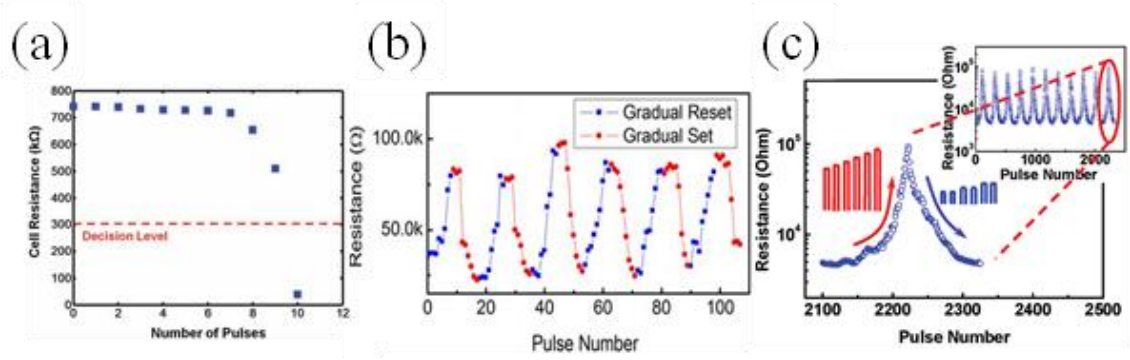

Figure 1.7. Synaptic plasticity in PCMs. a) Resistance changes of the PCM device upon the application of 10 pulses (~1 V, 60 s). b) Resistance change using simple square pulse for the both set and reset cycles. c) Gradual reset and set using pulses with increasing amplitude. a) Reproduced with permission.[67] Copyright 2013, John Wiley and Sons. b) Reproduced with permission.[68] Copyright 2015, John Wiley and Sons. c) Reproduced with permission.[66] Copyright 2012, ACS.

1.3.2 Resistive Random Access Memory (RRAM)

RRAM devices, where information is encoded in the programmable resistance levels, have garnered a lot of research interest in recent years as an emerging NVM technology because of their two-terminal device structure, fast switching speeds, low power consumption, good scaling potential and CMOS compatibility. Recently, RRAM devices have also been employed for the hardware acceleration of artificial neural networks because of their non-volatility and minimal standby leakage power compared to SRAM devices, as well as their potential for large-scale integration with the crossbar array structure. Based on current understanding of switching mechanisms in various RRAM systems, which are still under active investigations, RRAM can be generally categorized into the following three types: CBRAM, filamentary RRAM, and interfacial

RRAM (**Figure 1.8**). We will discuss the working principle of each type of these devices and their suitability as artificial synapses in the next sections.

CBRAM can be switched between LRS and HRS through the formation and dissolution of a conductive bridge (Figure 1.8a), consisting of metallic cation such as Ag or Cu, in an otherwise insulating switching layer, which can be metal oxides,[73] amorphous silicon,[74] or solid electrolyte (chalcogenide glasses mixed with metal).[75] During the SET, the cations are injected into the switching layer from the active electrodes, move under the applied electric field (*E*-field), and eventually form a metallic pathway that bridges to the other electrode. During the RESET, the conductive bridges are disrupted by an *E*-field with opposite polarity, resulting in a high resistance state.

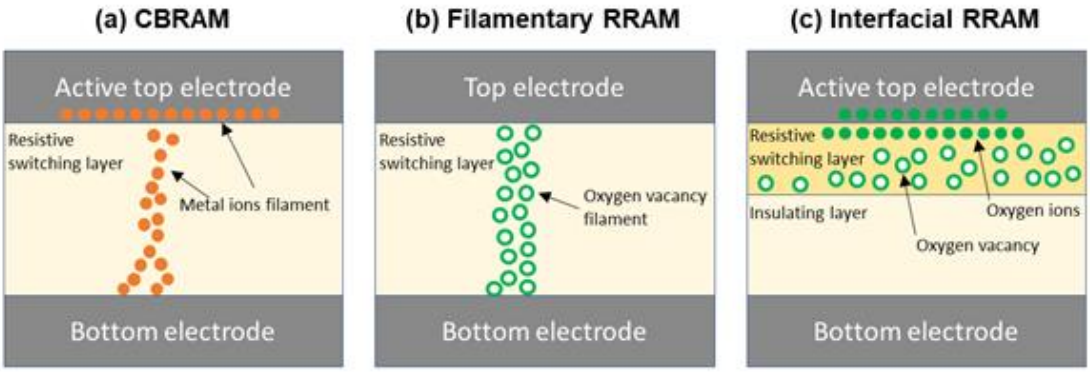

Figure 1.8. Device structure and working principle of various types of RRAMs. a) CBRAM is based on the conductive metal-ions filament formed electrochemically between active top electrode and resistive switching layer. b) Filamentary RRAM is based on oxygen vacancy filament through the resistive switching layer sandwiched between two inert metal electrodes. c) Interfacial-type RRAM, is based on the barrier modulation effect at the metal /switching material interface layer where the migration of oxygen ions towards the electrode reduces the effective barrier width of electron tunneling whereas the immobile oxygen vacancies randomly distribute in the resistive switching layer.

Attractive traits such as fast speed switching, good retention and scalability, and low power consumption have driven the development of CBRAM based artificial synapses. However, the abrupt and stochastic nature of the filament formation and dissolution processes may lead to non-linear and asymmetrical conductive responses as well as large device variations, both of which can negatively impact the performance of ANNs. Another potential issue is that the LRS states in CBRAM are often too conductive (typically ranging from 300 Ω to 1 kΩ),[76] which may cause large leakage currents in crossbar arrays.

Similar to CBRAM, the change in conductance in filamentary RRAM is based on the formation and rupture of filamentary bridges, which consists of oxygen vacancies instead of cations, in an otherwise insulating layer between metal electrodes. A typical metal-insulator-metal (MIM) structure of the filamentary RRAM device is shown in Figure 1.8b. The switching layer is usually simple metal oxide such as TiO_x,[77, 78] HfO_x,[79-82] AlO_x,[77, 79] WO_x,[83, 84] and TaO_x.[85, 86] During SET, an applied *E*-field induces a soft breakdown (which needs to be limited with a current compliance in a DC sweep) in the oxide and creates a conductive pathway consisting of oxygen vacancies, switching the device from a HRS to a LRS. For RESET, the filament is ruptured either through a recombination of oxygen vacancies with oxygen ions under an applied *E*-field with opposite polarity (bipolar) or via Joule heat under a larger *E*-field (unipolar as polarity of the *E*-field does not matter), inducing the LRS to HRS transition.[87] Advantages of filamentary RRAM include the use of highly accessible (in terms of today's CMOS fabrication facilities) CMOS-compatible switching materials, a simple structure, low cost, good scalability, and low power consumption. However, like CBRAM, it suffers from the abrupt and stochastic nature of the switching mechanism, as the filament growth and rupture processes are difficult to control. This

results in large device variations, non-linear conductance response, and limited analog states, which can limit their performance as artificial synapses.[85]

Compared to CBRAMs, filamentary RRAMs are expected to have slightly better endurance and retention performance due to the fact that oxygen vacancy filaments are typically more stable than metal cations filaments. In addition, the RESET process is less sensitive to the *E*-field induced drift effect. However, filamentary RRAM, especially those metal oxide based RRAMs, suffer from the so-called voltage-time dilemma,[88, 89] implying that there is a trade-off between ultra-fast programming speed and a long retention time under the reading voltage stress test. Yu et al. showed good endurance behavior with $>10^5$ cycles and mediate high temperature retention (7200 s at 100 °C) in their TiN/HfO_x/AlO_x/Pt devices although the device exhibited 50-ns programming speed.[79] Moreover, the Pt/TiO_{2-x}/Al_2O_3/Pt device developed by Prezioso et al. were cycled >5000 times without signs of degradation and were expected to have a long retention time of 10 years at room temperature at the expense of a relatively slow programming speed of 500 μs.[77] Besides this, large device variations are still an issue for synapses based on filamentary RRAM due to the stochastic nature of switching process involved in random distribution of oxygen defects.

Interfacial RRAM, or non-filamentary RRAM, is based on the tunnel barrier modulation effect at the interface of the metal/switching layer, through the migration of oxygen ions. Unlike filamentary RRAM, an additional oxide layer (typically called the insulating layer) is present to act as a load resistor to prevent thermal runaway and to eliminate the need for current compliance (Figure 1.8c). Common resistive switching layers include exotic oxides such as TaO_x and $Pr_{1-x}Ca_xMnO_3$ (PCMO).[90-92] During SET, the oxygen ions in the resistive switching layer migrate towards the metal/switching material interface under the applied *E*-field. This reduces the barrier

height for electrons to tunnel from metal into switching layer, leading to the HRS to LRS transition. With an oppositely applied *E*-field during RESET, oxygen ions migrate back to the switching layer, thus increasing the tunnel barrier height, and resulting in a HRS. The switching process for interfacial RRAM is more gradual (and without the need for forming), making it a suitable candidate for artificial synapses. It features unique advantages such as self-compliance, forming-free, and gradual switching with good analog precision. However, the programming speed in interfacial RRAM is relatively slow in order to satisfy the energy requirement needed to ensure that a high energy barrier is built for good retention.[33, 88] Additionally, the use of exotic switching materials may present fabrication challenges and increase the cost.

1.3.3 Electrochemical Devices

Besides technologies that are originally geared towards NVM applications (e.g., RRAM and PCM), researchers are also developing new device concepts for synaptic electronics. Recently, electrochemical based devices have emerged as a promising candidate due to their high precision levels, linear and symmetrical conductance responses, low switching energies, high scalability, and built-in timing mechanisms suitable for SNNs.[11, 12, 47, 93] In an electrochemical synapse, the synaptic weight (encoded in the channel conductance of the device) can be controllably and reversibly modulated via a gate terminal, which dictates the ionic concentration (and hence the synaptic weight) in the channel material. This process often involves electrochemical reactions through an electrolyte, which facilitates ionic exchanges but limits electron conduction.

In this section, we discuss the four pioneering electrochemical synapses (**Figure 1.9a-d**) with channel materials consisting of lithium cobalt oxide ($LiCoO_2$),[11] organic polymers (poly(3,4-ethylenedioxythiophene): polystyrene sulfonate or PEDOT:PSS),[12] tungsten diselenide

(WSe_2),[93] and graphene.[47] These types of synaptic devices have each demonstrated good precision, low switching energy, a highly linear response, and good scaling potentials. While these electrochemical synapses do require a third gate terminal, it offers a rare combination of low programming voltage/energy and good retention characteristics. In two-terminal NVM devices such as RRAM[85] and PCM[94], there is often a tradeoff between programming voltage/energy and retention because the programming and retention barrier is often the same (Figure 1.9e); whereas in the three-terminal electrochemical synapses, the programming and retention mechanisms are decoupled (Figure 1.9f), allowing us to achieve both low switching energy and good retention behaviors.

In 2017, Fuller et al.[11] developed a synaptic transistor (Figure 1.9a**)** consisting of $LiCoO_2$, a common cathode material for Li ion batteries (LIBs), and lithium phosphorus oxynitride (LiPON), a solid electrolyte with good chemical stability.[95] $LiCoO_2$ is chosen as the channel material for this solid-state synapse because of its good endurance and well-characterized electrochemical behaviors, based on its performance in LIBs.[96] Through reversible Li intercalation, the authors demonstrated controllable tuning of the channel conductance (synaptic weight) with a precision of 200 states per device from ~150 to 250 μS range (i.e. an on/off ratio ~1.67×) with good linear responses (**Figure 1.10a**). This proof-of-concept demonstration offers a new direction for synaptic electronic based on the insertion and extraction of mobile ions.

Around the same time in 2017, Burgt et al.[12] demonstrated a polymer synapse (Figure 1.9b) based on reversible electrochemical reactions in a PEDOT:PSS film partially reduced with poly-ethylenimine (PEI). The synaptic plasticity in this organic synapse is achieved by the controllable insertion and extraction of protons in the PEDOT:PSS/PEI channel. Through pulse measurements, a record-high precision of 400 states per devices was achieved with a less-than-

ideal dynamic range (between 550 to 850 μS), as illustrated in Figure 1.10b. This polymer synapse displays a symmetric, repeatable and highly linear conductance response with very low noise (<1%).

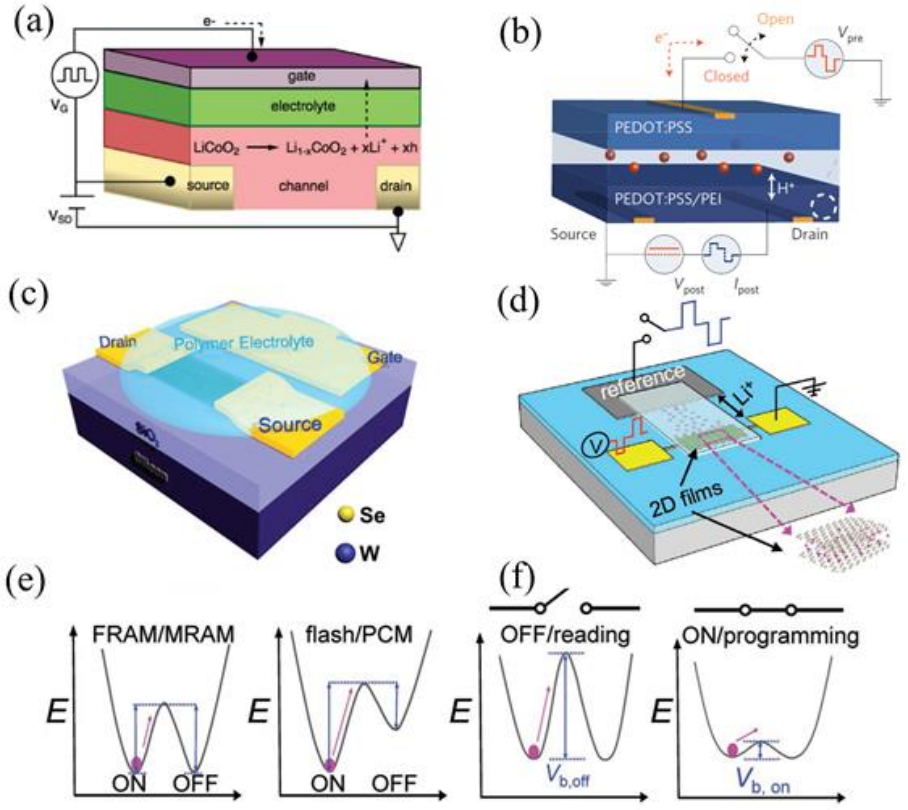

Figure 1.9. Electrical chemical synapses. a) A schematic of synaptic transistor with $LiCoO_2$ as active channel. b) An organic polymer synapse consisting of liquid electrolyte (NaCl or KCl) sandwiched by PEDOT:PSS and PEI treated PEDOT:PSS layers. c) An ionic-gated synaptic transistor based on metal dichalcogenide crystal (WSe_2) and phosphorus trichalcogenide ($NiPS_3$ and $FePSe_3$). d) An electrochemical graphene synapse. e) Schematics of energy barriers for conventional memory technologies. f) Energy barriers for electrochemical synapses are decoupled for reading and programming. a) Reproduced with permission.[11] Copyright 2017, John Wiley and Sons. b) Reproduced with permission.[12] Copyright 2017, Nature. c) Reproduced with permission.[93] Copyright 2018, John Wiley and Sons. d-f) Reproduced with permission.[47] Copyright 2018, John Wiley and Sons.

In 2018, two other groups reported electrochemical synapses based on 2D materials. 2D materials are attractive due to their interlayer spacings, which offer good sites for mobile ions to

move through electrochemical intercalation. Zhu et al.[93] built ionic gated synaptic devices based on WSe_2 and phosphorus trichalcogenide while Sharbati et al.[47] demonstrated graphene synapses through Li intercalation. In both studies, a gel electrolyte (lithium perchlorate ($LiClO_4$) dissolved in polyethylene oxide (PEO)) were used for ionic exchange. Zhu et al. adopted Au as the ionic gate, while Sharbati et al. employed lithium ion phosphate (LFP) as the ion reservoir (similar to the reference electrode in LIBs) in their graphene device to facilitate controllable electrochemical reactions. The reported precision level per device for WSe_2 based synapse was 60 states with dynamic range ~263 to 570 pS, while the graphene synapse showed > 250 precision states with a dynamic range 130 to 1130 μS (i.e., an on/off ratio ~ 8.7×), as shown in Figure 1.10c,d. The electrochemical synapses have better precision levels compared to technologies that are originally designed for binary or MLC NVMs (usually <16 levels per device), because the carrier concentration in their channels can be controllably tuned by modulating the ionic concentration via the gate terminal. This gradual change in conductance in electrochemical synapses has also led to more linear conductance responses compared to PCM and RRAM devices in general.

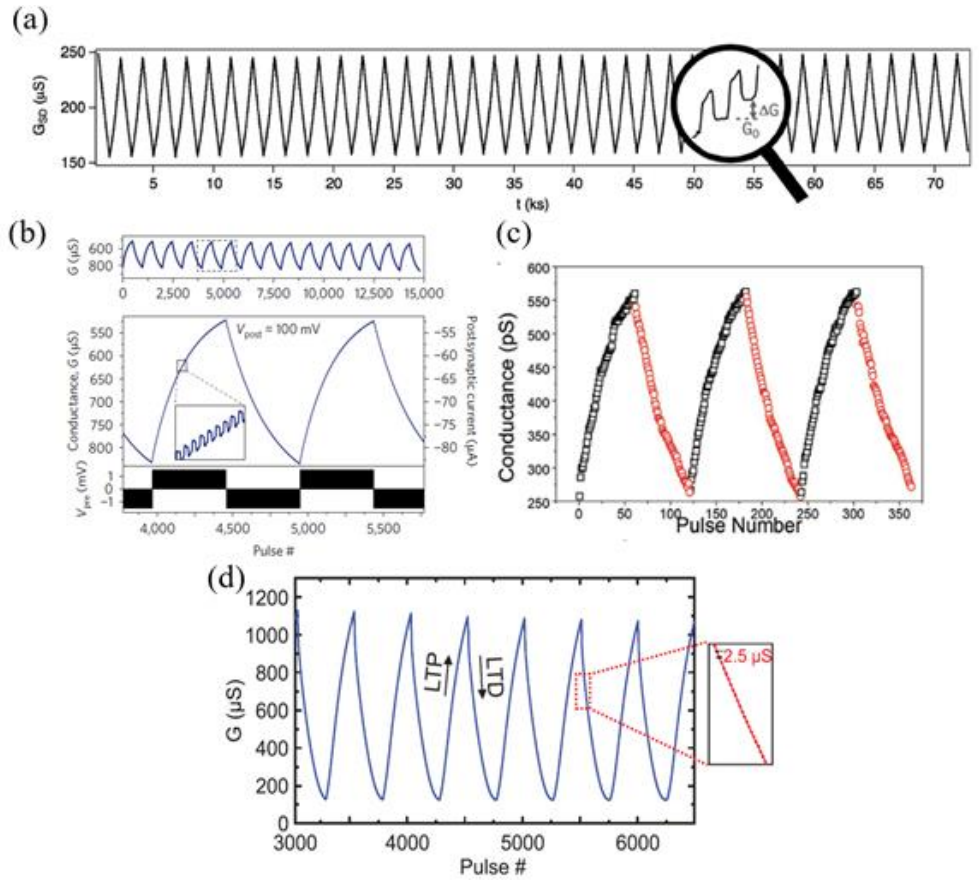

Figure 1.10. LTP and LTD in electrochemial synapses. a) the $LiCoO_2$ synaptic transistor by Fuller *et. al.* b) the polymer synapse by Burgt *et al.* c) the WSe_2 synapse by Zhu *et al.* d) the graphene synapse by Sharbati *et al*. a) Reproduced with permission.[11] Copyright 2017, John Wiley and Sons. b) Reproduced with permission.[12] Copyright 2017, Nature. c) Reproduced with permission.[93] Copyright 2018, John Wiley and Sons. d) Reproduced with permission.[47] Copyright 2018, John Wiley and Sons.

1.3.4 Two-Dimensional (2D) Devices

2D materials, consisting of graphene (**Figure 1.11a**), hexagonal boron nitride (h-BN) (Figure 1.11b), transition metal dichalcogenides (TMDs) with the form of MX_2 (where M = transition metal and X = chalcogen, such as MoS_2 in Figure 1.11c), and black phosphorus (BP) (Figure 1.11d), offer a set of uniquely attractive optical,[97] electrical,[98] and thermal properties.[99]

These include sub-nanometer thickness without dangling bonds, transition from indirect (bulk) to direct (monolayer) band gaps when thinned down (MoS_2, WS_2),[100] highly in-plane anisotropy (BP)[101] and anisotropic thermal transport (high in the in-plane direction[102] and low in the cross-plane direction[103]). These 2D materials also demonstrate various band structures: semi-metal (graphene, WTe_2),[104] small band gaps for low-power transistor applications ($MoTe_2$, $HfSe_2$),[105] semiconducting (MoS_2, WS_2, BP),[106] and large band gap or insulating h-BN, making them promising candidates for the next-generation computing devices.

Based on a rich collection of physical mechanisms such as charge trapping, resistive switching, Joule heating etc., researchers are developing 2D based artificial synapses as illustrated in Figure 1.11e-j. Tian et al. reported one of the first 2D synapses with tunable plasticity based on twisted bilayer graphene.[107] As shown in Figure 1.11e, the synaptic weight is encoded in the graphene channel conductance and can be modulated by the amount of trapped charges at the AlO_x defect sites, which in turn is controlled via the programming pulses from the top gate.[107] Shi et al. built a multilayer h-BN synapse (Figure 1.11f), where the device conductance was tuned through the generation of boron vacancies as well as the formation of metallic ions conductive pathways.[108] The switching mechanism in metal/h-BN/metal synapses is similar to that in CBRAM, with the difference being that the formation of cation pathways in h-BN synapses is accompanied by the generation of boron vacancies.[108]

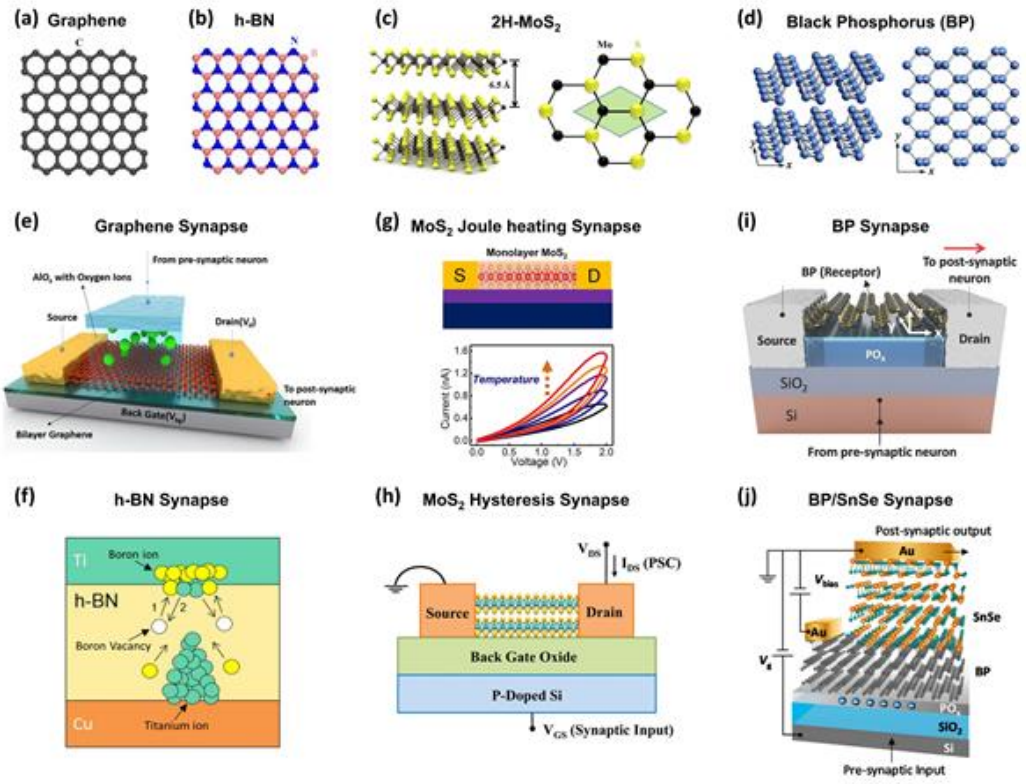

Figure 1.11. 2D synapses. a, b) Lattice structures of graphene and h-BN. Reproduced with permission.[109] 2017, Springer Nature. c) Lattice structure of MoS_2. Reproduced with permission.[110] 2013, American Chemical Society. d) Lattice structure of BP. Reproduced with permission.[111] 2014, American Physical Society. e) A schematic of a graphene dynamic synapse. Reproduced with permission.[107] 2015, American Chemical Society. f) A schematic of a h-BN synapse. Adapted with permission.[108] 2018, Springer Nature. g) A schematic of a MoS_2 synapses based on Joule heating. h) A schematic of a back-gated MoS_2 hysteresis synapse. i) A schematic of a BP synaptic device. j) A schematic of the BP/SnSe heterojunction synaptic device. a-g) Adapted with permission.[112] 2018, American Chemical Society. h) Reproduced with permission.[113] 2017, American Chemical Society. i) Reproduced with permission.[114] 2016, Wiley. j) Reproduced with permission.[115] 2017, American Chemical Society.

Sun et al. demonstrated synaptic plasticity through Joule heating effect in monolayer MoS_2 devices (Figure 1.11g).[112] Resistive heating in MoS_2 leads to a residual temperature increase, which can modulate the synaptic weight based on the temperature-dependence of the device

conductance.[112] Arnold et al. also built a MoS_2 synapse **(**Figure 1.11h) taking advantage of the hysteresis in its I-V characteristics, which is likely due to charge trapping by adsorbed gas molecules, and/or by MoS_2/SiO_2 interface and/or by defects in MoS_2.[113] Tian et al. reported a BP synapse exploiting the charge transfer between the BP channel and the native PO_x functional layer, where the channel conductance was modulated through charge transfer induced by gate pulses (Figure 1.11i).[114] Lastly, a BP/SnSe junction-based synaptic device was also demonstrated by Tian et al. employing the tunable electronic properties of the BP and SnSe heterojunction to mimic the synaptic plasticity (Figure 1.11j).[115]

1.3.5 Device Metrics Comparison

The development of synaptic electronics for the hardware implementations of ANNs has progressed rapidly in the last few years. Because of similar requirements in programming and retention, emerging NVM technologies such as PCM and RRAMs have attracted much attention as possible candidates for building large-scale artificial neural networks. It should also be noted that an ideal synaptic device also possesses properties that are traditionally less important (even irrelevant) in NVM applications such as good precision levels, high linearity, and symmetrical conductance responses. In addition, the specific requirements of synaptic devices are likely application-dependent, for e.g., good retention is more important for a neural network that is trained offline, where online training requires better endurance and more linear behaviors due to the frequent weight update. Hence, emerging devices based on electrochemical reactions or 2D materials, which are not originally geared towards NVM applications, are also being extensively investigated by researchers and reviewed here.

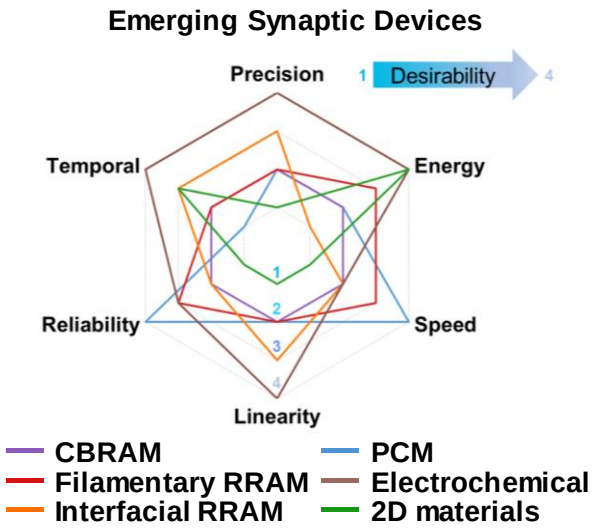

Figure 1.12. Radar graph comparing the device metrics among emerging synaptic devices. PCM (blue lines), CBRAM (purple lines), Filamentary RRAM (red lines), Interfacial RRAM (Orange lines), Electrochemical synaptic devices (brown lines) and 2D Materials-based synaptic devices (green lines) are compared in terms of precision, energy, speed, linearity, reliability, temporal characteristics. 1 to 4 represents the four different degrees of desirability, respectively.

Figure 1.12 summarizes the performances of a number of synaptic devices based on PCM, the three types of RRAMs (CBRAM, filamentary, and interfacial), electrochemical devices, and 2D materials in terms of crucial device metrics such as precision (# of states), switching energy, operating speed, the degree of linearity and symmetry of the conductance response, reliability (device variations, endurance, and retention), and the potential in spatio-temporal dynamics for SNNs. PCM synapses have fast speed, decent precision and adequate endurances; but its non-linear behavior, high RESET power, and large variation from the melt-quench process may hamper its performance. RRAMs offer CMOS compatibility, simple structure, and good scalability; however large device variation from the stochastic nature of the switching mechanisms can limit learning accuracy in large-scale neural networks. In addition, the abrupt SET process in CBRAM and filamentary RRAM can result in non-linear and asymmetrical response and also limit the device precision. Interfacial RRAMs have shown more gradual switching with better precision,

though it typically comes with a smaller dynamic range and has a slower switching speed compared to other RRAM devices.

Nanoscale devices based on electrochemical reactions offer good precision, linearity, and potentially low device variations. The low operating speed due to the slow ionic movement may be mitigated by device scaling. But reactive cations (e.g., Li^+) can pose contamination issues and may be incompatible with CMOS devices. 2D materials offer good scalability and the potential for in-memory computing as 2D devices are considered as promising candidates for next-generation logic devices. However, researchers are still looking for an ideal switching mechanism in 2D devices as current 2D synapses based on charge trapping offer limited precisions, non-linear and asymmetrical responses, and poor reliability.

To implement timing based plasticity for SNNs, many of the existing approaches employ complex timing circuitry and are thus not scalable. Techniques that utilize secondary effects with built-in temporal components such as electrostatic gating, Joule heating, or charge trapping are preferred.

While most existing synaptic device cannot fulfill the requirement of an ideal electronic synapse at the moment, there is an enormous opportunity to achieve orders of magnitude improvement in computation capability and energy efficiency through the hardware acceleration of ANNs. By combing electrochemical reaction effect with 2D materials, an artificial electronic synapse, optimized for the hardware acceleration of ANNs, can be achieved.

In the following chapters, electrochemical synapses based on topological insulator $(Bi_xSb_{1-x})_2Te_3$ film and perovskite tungsten trioxide will be presented with programmable spatio-temporal dynamics, high precision, linear and symmetric weight response, and great scalability in terms of

energy and speed, which shows its promising potential to lead to the hardware acceleration of truly neurorealistic ANNs with superior cognitive capabilities and excellent energy efficiency.

1.4 Arterial Blood Pressure Monitoring

1.4.1 Blood Pressure Monitoring Techniques

Blood pressure is one of the most vital hemodynamic parameters in the cardiovascular system, especially for patients with hypertension or hypotension.[116-118] Close monitoring of the arterial blood pressure (ABP) is beneficial to providing early disease intervention and treatment.[119] **Figure 1.13** demonstrates the common BP monitoring techniques. Invasive blood pressure monitoring via implanted catheter into the artery offers a continuous, accurate real-time BP measurement, which is regarded as the clinical reference method; it is used mostly in intensive care unit (ICU) settings.[120] Some disadvantages of invasive BP monitoring are that it requires high-risk surgical procedures, medical expertise, and long operation time, and it may cause complications such as embolism and ischemia.[118] Non-invasive blood pressure (NIBP) monitoring techniques including auscultation, palpation, and oscillometry, are quite popular in non-intensive settings such as for routine clinic care as well as ambulatory and at-home monitoring since they offer great accessibility and convenience. [116-118] However, they are intermittent and only produce systolic and diastolic BP values. Continuous non-invasive blood pressure (CNIBP) monitoring is advantageous in settings where the hemodynamic stability or BP stability of patients is of greater interest since it is able to more quickly recognize patients' hemodynamic status and reveal real-time BP levels consisting of comprehensive hypotensive and hypertensive episodes.

Thus, it renders earlier disease diagnosis and immediate treatment for patients where cases of stroke or heart failure can be prevented.[118, 120]

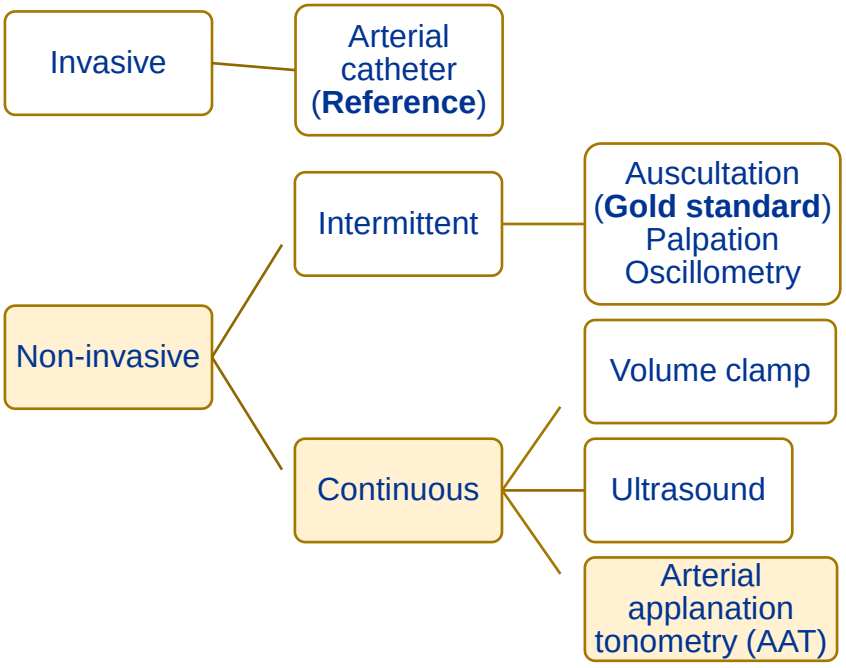

Figure 1.13. BP monitoring techniques.

1.4.2 Sensor Requirements for Arterial Applanation Tonometry

CNIBP monitoring can be achieved using volume-clamp based photo-plethysmography (PPG) sensors,[121-126] arterial applanation tonometric (AAT) sensors,[20, 127-129] and ultrasound sensors.[130] Of these sensor types, AAT sensors, which use transducers that press against an underlying artery on the skin to measure the external BP,[117] have garnered much research interest due to their simple sensing mechanism and convenient electro-mechanical signal acquisition and calibration. Mechanical pressure pulse waves that are associated with blood flow changes in the underlying artery are transduced into electrical signals detected by AAT sensors.[117] Commercial AAT sensors, called T-Line devices,[128, 129] have been clinically proven to be reliable, but they are

bulky and uncomfortable to wear due to the usage of rigid materials. It has been found by Pressman et.al[131] and Kemmotsu et. al[132] that an accurate AAT system must meet the following requirements: 1) the sensing element must be very sensitive; 2) the artery surface below the pressure sensor must be flattened under external force; and 3) the sensor must be positioned well, right on top of the artery surface and conformable to the skin. The metrics for evaluating AAT sensor performance are summarized in Figure **1.14a**[133]. Figure 1.14b indicates the basic working principles of the arterial applanation tonometry.[134] According to Laplace's law of cylindrical tubes, the transmural pressure is governed by $P_t = (T \times \mu) / r$, as shown in Figure 1.14b. The applied applanation pressure is used to flatten the underlying blood vessels in order to maximize the detected BP signals. Ideally, the maximized BP signals occur when the applanation pressure equals arterial blood pressure.[134] Therefore, developing an ATT sensor that is soft, conformable to the skin, linear and sensitive over a large pressure range, with high fidelity signals and a large dynamic range would greatly enhance the BP sensing accuracy.

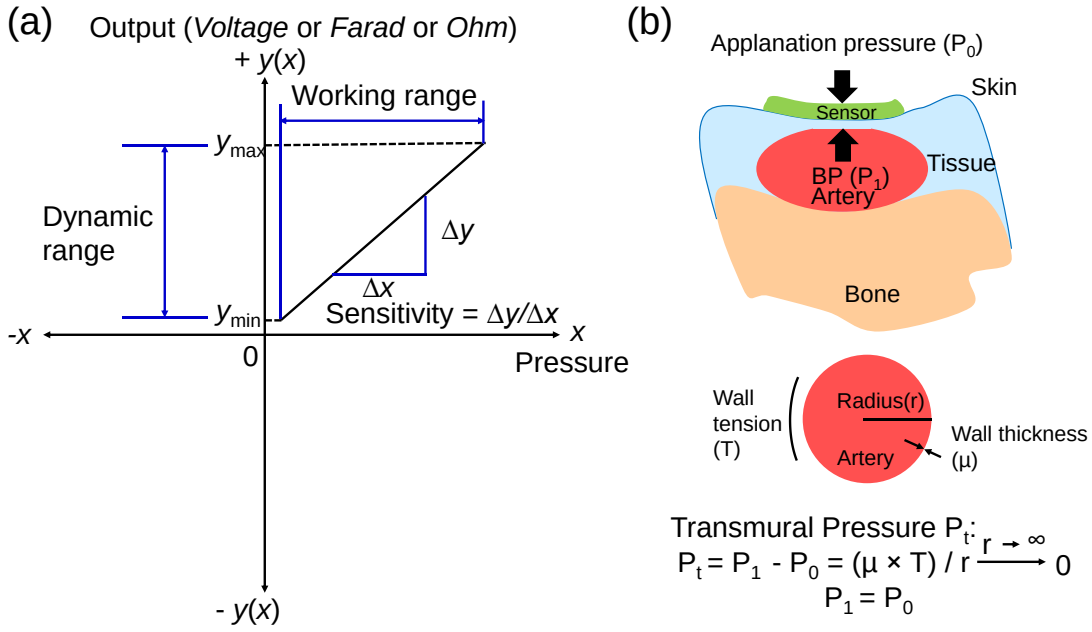

Figure 1.14. The AAT sensor performance metrics and working principles.

1.5 Existing Flexible Pressure Sensors

In this section, various types of flexible mechano-electric sensors including piezoelectric, piezoresistive, piezocapacitive, and supercapacitive iontronic sensors are reviewed. **Figure 1.15** demonstrates the working mechanisms of these various types of flexible pressure sensors. **Table 1.1** provides a summary of characteristics of the reviewed flexible pressure sensors as reported in the literature, including the sensor structure, working range, sensitivity, linearity, limit of detection, and response time.

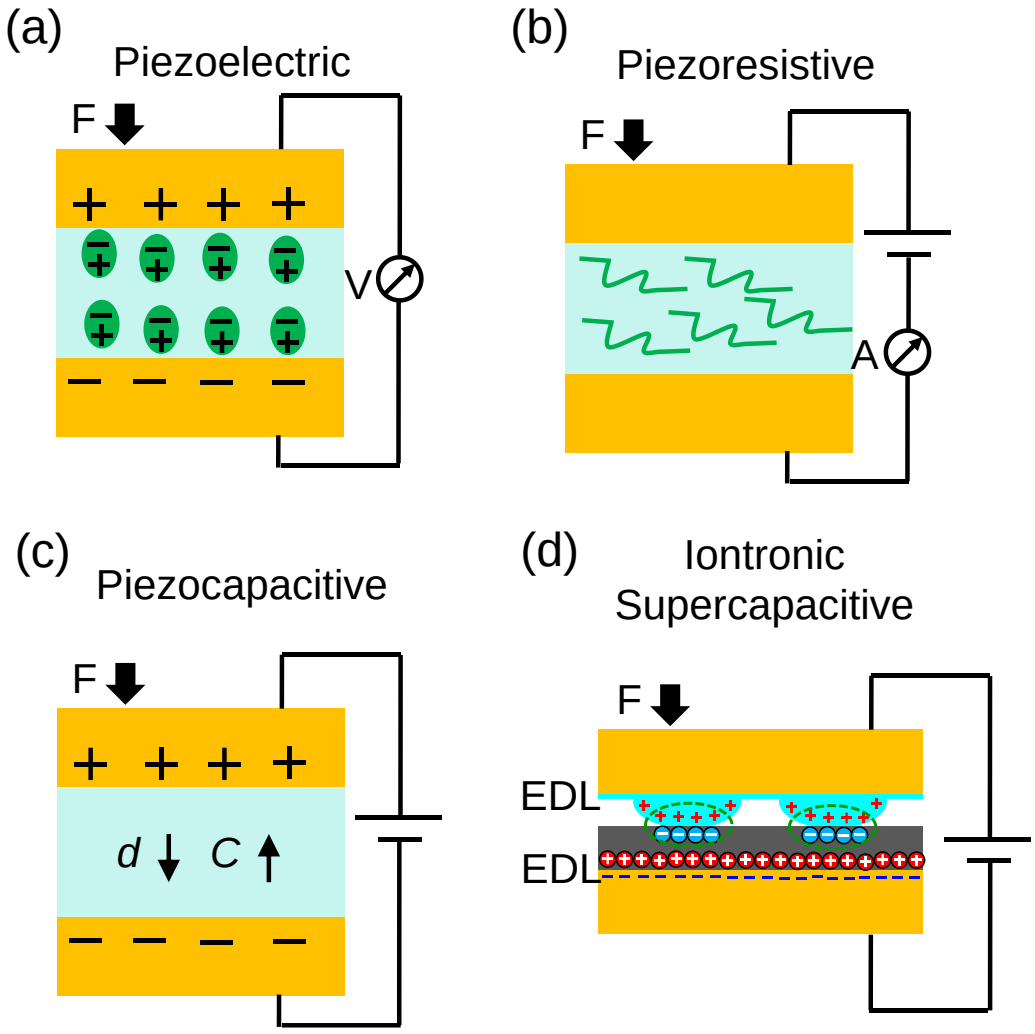

Figure 1.15. Working mechanisms of various types of flexible pressure sensors.

Piezoelectric sensors (Figure 1.15a) take advantage of the characteristics of piezoelectric crystalline materials, which allow them to align dipole moments and generate electric voltages under external mechanical pressure.[127, 135] While piezoelectric sensors are highly sensitive to dynamic pressure changes, they cannot respond to static pressure changes. Also, they exhibit fast response time (0.1 ms) and very small limit of detection (0.005 Pa), but the working range of common piezoelectric sensors is very limited.[127]

Piezoresistive sensors measure the electrical resistance change between two electrodes. Fabrics,[136] foam composites,[137] or microstructures[138] can be utilized as active materials, where external applied pressure induces resistance changes via changing the shape of the active materials or contact areas between electrodes and dielectrics. Piezoresistive sensors (Figure 1.15b) have a simple sensing mechanism, and, unlike Piezoelectric sensors, respond to both dynamic and static pressure and enable linear pressure – resistance responses in a wide working range.[136-138] However, there is a tradeoff between working range and sensitivity. Moreover, the resistive changes are susceptible to thermal and electromagnetic transmission line noise.

Piezocapacitive sensors (Figure 1.15c) have been studied a lot because of their simple device structure, simple sensing mechanism, good response to both static and dynamic pressure, and immunity to thermal and electromagnetic noise. However, most piezocapacitive sensors demonstrate only low to medium sensitivity, [139-144] partly because they rely on the physical distance (*d*) between two electrodes to modulate the capacitance, which is limited by the structural stiffness of the active soft elastomer. Moreover, the limited dielectric constant of the active dielectric soft materials and the small physical distance between electrodes usually renders the capacitive values in the pF cm^{-2} range. This small capacitance value is susceptible to parasitic charges and environmental noises.[145]

Iontronic supercapacitive sensors (Figure 1.15d), as a new type of iontronic device, have demonstrated excellent sensing performance in that they exhibit a broad working range, high sensitivity, medium to high linearity, and low limit of detection. [146-151] Most importantly, leveraging the supercapacitive effects at iontronic/electronic interface results in an ultrahigh unit area capacitance (~ μF cm^{-2}) for iontronic pressure sensors. This ultrahigh capacitance is beneficial to improving the sensing resolution and sensitivity of the sensor, and it helps to obtain high-fidelity output signals without the use of external amplifying elements. Additionally, it provides an excellent immunity from environmental noises and offers strong responses to both dynamic and static pressure changes. One issue for iontronic supercapacitive sensors, however, is their relatively slow response time; the response is likely limited by the low ionic mobility in the ionic dielectric layers. Therefore, materials selection plays an important role in both determining the sensor performance and electrochemical stability.

In the following chapters, the development of a high-fidelity iontronic tonometric sensor (ITS) with high sensitivity, high linearity, and a large dynamic range within a broad working range is discussed. We demonstrate that we can control the initial interfacial contact area and tune the sensitivity of the device by microengineering the contact electrodes that interface with the iontronic film into different micropyramid patterns. We tune the performance of our ITS to meet the requirements for AAT BP monitoring. We further explore the application of our ITS in monitoring real-time beat-to-beat BP by measuring the brachial and radial pulse waveforms. The detected pulse waveforms can be utilized to recognize patients' hemodynamic status and reveal real-time BP levels. Our ITS work provides a rational design for a flexible pressure sensor with high sensitivity, high linearity, and a large dynamic range for real-time CNIBP monitoring.

Table 1.1. The reviewed flexible pressure sensors in the literature.

Type	Device Structure	Working range (kPa)	Linearity	Sensitivity (kPa^{-1})	LOD (Pa)	Response time (ms)	Recovery time (ms)	Ref #
Piezoelectric	PI/PZT/Pt/ SiNM n-MOSFET	0 - 0.01	NA	NA	0.005	0.1	0.1	[127]
	ITO/PET/PTFE woven/PDMS	0 - 1.2	NA	10.3 - 47.5 mV/Pa	2.5	5	5	[135]
Piezoresistive	PEN/Fabric/Au electrode/PI	0 - 35	High	0.585	NA	4	4	[136]
	Au/ Hollow foam composite /Au	0 -60	High	15.9	NA	1.2	NA	[137]
	Elastomer/Liquid metal/ Microbump/Microchannel	0 - 50	High	0.158	16	77	NA	[138]
Piezocapacitive	Ecoflex/CNT/Porous PDMS /CNT/Micropyramid Ecoflex	0 - 30	Low	2.24	2	84	117	[139]
	Si/Al/Micropyramid PDMS/Al/Si	0 - 22	Medium	0.2	NA	NA	NA	[140]
	PET/ITO/Micropyramid PDMS/ITO/PET	0 - 200	Medium	0.02	NA	NA	NA	[141]
	PI/Au/PMMA/Conductive porous nanocomposite/Au/PI	0 - 50	Medium	0.43 - 3.13	7	94	NA	[142]
	Silicone/Wrinkled Au/Dielectric/Wrinkled Au/Silicone	0 - 700	High	0.148	NA	NA	NA	[143]
	Micropyramid PDMS gated organic field-effect transistors	0 - 18	Medium	NA	NA	300	500	[21]
	PET/ITO/Micropyramid PDMS dielectric gated organic field-effect transistors	0 - 56	Low	0.38- 8.2	NA	10	10	[20]

Table 1.1. (continued).

Piezocapacitive	PET/ Au - coated Micropyramid PDMS dielectric gated 2D MoS_2/WSe_2 transistors	0 - 2.15	NA	10^3 - 10^7	NA	40	40	[22]
	PET/ITO/Porous pyramid PDMS/ITO/PET	0 - 35	Medium	0.124 - 44.5	0.14	9	30	[144]
Supercapacitive	PET/ITO/Nafion Ionic film/Skin	0 - 30	Low	0.15 - 5 nF/kPa	NA	NA	NA	[18]
	PI/Au/Fabric IL/Au/PI	0 - 175	High	6.5 - 13.5	7.5	30	30	[146]
	PET/Au/Micropilllar Ionic film/Au/Microdome epoxy resin	0 - 485	High	49.4	NA	0.61	3.63	[147]
	PET/ITO/Micropyramid Ionic film/ITO/PET	0 - 50	Medium	2 - 41.64	NA	21	22	[148]
	Ag-plated fiber/Ionic gel film/Ag-plated fiber	0 - 4	NA	308 nF/kPa	300	272	234	[149]
	Au-coated microstructured PDMS/Ionic nanofibrous membrane/Au-coated microstructured PDMS	0 - 300	High	1.5 - 5.5	2	70.4	92.8	[150]
	PDMS/Cu/Ion gel/Sandpaper molded CNT/PDMS microbump nanocomposite/Ion gel/Copper/PDMS	0 - 8	NA	0.25 - 9.55	5	52	52	[151]
	Conductive fibric/Nanofibrous layer/Conductive fabric	0 - 10	Medium	14.8 - 114 nF/kPa	2.4	4.2	NA	[152]
	PI/Au/Sandpaper molded microstructured ionic gel film/Au/PI	0 - 360	Medium	229.9 - 3302.9	0.08	9	9	[19]

Table 1.1. (continued).

	PET/Graphene/Ionic liquid droplet/Graphene/PET	0 - 15	Medium	31.1	NA	78	78 [153]
	PI/Au/Ionic gel/Au-coated micropillar PDMS electrode	0 - 180	High	7.49 - 33.16	0.9	9	9 [154]
	PI/ITO/Ionic gel/sandpaper molded PDMS-Ppy elastic electrode/PI	0 - 100	Medium	3.65 - 26.6	2.88	NA	NA [155]
Supercapacitive	Au-coated PDMS micropillar/ Skin/Au	0 - 15	Low	0.3 - 11.8	0.2	15	15 [156]
	PI/AgNWs/Calathea zebrine leaf molded microstructured ionic gel/AgNWs/PI	0 -115	Medium	1.03 - 54.31	0.1	29	37 [157]
	PDMS/AgNWs/Sandpaper molded iontronic film/AgNWs/PDMS	0 -33	Medium	11.73 - 131.5	1.12	43	71 [158]

2.0 Dynamic $(Bi_xSb_{1-x})_2Te_3$ (BST) Synapses with Spatio-Temporal Dynamics

2.1 Motivation

Neuromorphic computing has recently emerged as a promising paradigm to overcome the von-Neumann bottleneck and enable orders of magnitude improvement in bandwidth and energy efficiency. However, existing CMOS digital devices, the building block of our computing system, are fundamentally different from the analog synapses, the building block of the biological neural network, rendering the hardware implementation of the ANNs not scalable in terms of area and power, with existing CMOS devices. In addition, the spatio-temporal dynamic, a crucial component for cognitive functions in the neural network, has been difficult to replicate with CMOS devices. Here, we present the first topological insulator (TI) based electrochemical synapse with programmable spatio-temporal dynamics, where long-term and short-term plasticity in the TI synapse are achieved through the charge transfer doping and ionic gating effects, respectively. We also demonstrate basic neuronal functions such as potentiation/depression and paired-pulse facilitation with high precision (>500 states per device), as well as a linear and symmetric weight update. We envision that the dynamic TI synapse, which shows promising scaling potential in terms of energy and speed, can lead to the hardware acceleration of truly neurorealistic ANNs with superior cognitive capabilities and excellent energy efficiency.

2.2 The Structures and Properties of BST Synapses

2.2.1 The Structures of BST Synapses with Electrochemical Effects

Here, we present the first ternary topological insulator $(Bi_{0.2}\ Sb_{0.8})_2Te_3$ based synaptic device – with a programmable spatio-temporal response, a high precision (>500 states per device), and a linear and symmetric weigh update – for the hardware implementation of artificial neural networks. In the BST synapse (**Figure 2.1a**), the channel conductance represents the synaptic weight, which can be reversibly modulated through the ionic gate.[47] We choose the ternary TI compound BST for this work because of its potential in large-scale, high-quality fabrication through molecular beam epitaxy (MBE), its layered structure to accommodate intercalated ions, and its tunable transport properties via band structure engineering.[159] The band structure of BST can be tuned to reach an insulating bulk state with conducting surface states, which is useful for synaptic applications because having this initial insulating bulk state can lead to a larger dynamic range as we increase the channel conductance through Li intercalation. Transport and angle-resolved photoemission spectroscopy (ARPES) measurements from our prior work[159] indicate that the stoichiometry with x = 0.2 in $(Bi_xSb_{1-x})_2Te_3$ leads to a very insulating bulk state at 300 K, with the sheet resistance close to its maximum value, thus eliminating the need to go down to low temperatures for synaptic applications. Moreover, the atomically-flat surfaces from the MBE-grown epitaxial films help promote the strength of the ionic gating effect,[160] which contributes to the short-term synaptic plasticity.

The schematics of our three-terminal BST synaptic device is shown in Figure 2.1a, where BST film grown on sapphire substrate forms the conduction channel (patterned by photolithography combined with dry etching process), representing the synaptic weight. The

source and drain electrodes consist of Cr/Au (20/100 nm); and the ionic gate (as well as the Li+ ion reservoir) is made of lithium iron phosphate (i.e., $Li_{0.6}FePO_4$ or LFP). LFP is a common cathode material in Li-ion batteries because of its safety, nontoxicity, and low cost; and it provides a constant electrochemical reference to ensure stable operations in the BST synapse.[161, 162] Solid polymer electrolyte (prepared by dissolving $LiClO_4$ in polyethylene oxide (PEO))[163] is spin-coated onto the device to facilitate ionic exchange (but electrically insulating) between the LFP gate and the BST channel. The read operation is done by applying a small signal to access the conductance between the source and drain (with the gate open); while the write operation is through programming pulses between the gate and the BST channel.

One of the unique features of our electrochemical BST synapse is its programmable spatio-temporal dynamics – demonstrating tunable long-term and short-term plasticity, which is crucial for implementing a truly neurorealistic ANN and a feature that has been difficult to achieve with conventional CMOS and memory devices. The long-term (non-volatile) effect originates from the charge transfer doping through the intercalated ions.[164] BST has a layered rhombohedral structure (Figure 2.1b), where five covalently bonded atomic sheets (Te-Bi/Sb-Te-Bi/Sb-Te) form one quintuple layer (QL) (~1 nm).[165] We choose to intercalate Li+ ions in this work because of its well-characterized electrochemical behaviors from the LIB industry and its small diameter (1.5 Å)[166] for ease of intercalation, especially since successful intercalation in BST has been demonstrated with slightly larger Cu+ ions (1.8 Å).[167] As positive Li+ ions are electrochemically intercalated into (de-intercalated out of) the van der Waal spacing between the neighboring QLs in BST, the negative electrons enter (leave) the BST conduction band and result in a long-term increase (decrease) in carrier concentration and the channel conductance (synaptic weight).

The short-term (volatile) effect stems from the ionic gating effect[164] (Figure 2.1c), where an electric double-layer is formed at the electrolyte/BST interface and induces strong electrostatic gating in the BST channel. The ionic gating effect is volatile since the EDL and its associated change in carrier concentration in BST dissipate when the programming pulse is removed. Combining these two mechanisms, we have demonstrated synaptic characteristics such as short-term and long-term plasticity, potentiation and depression, and paired-pulse facilitation with the BST synapse in this work. We can also engineer the spatio-temporal response in these electrochemical synapses by manipulating the pulse amplitude, the pulse width, and the device dimensions, as we will detail in the following sections.

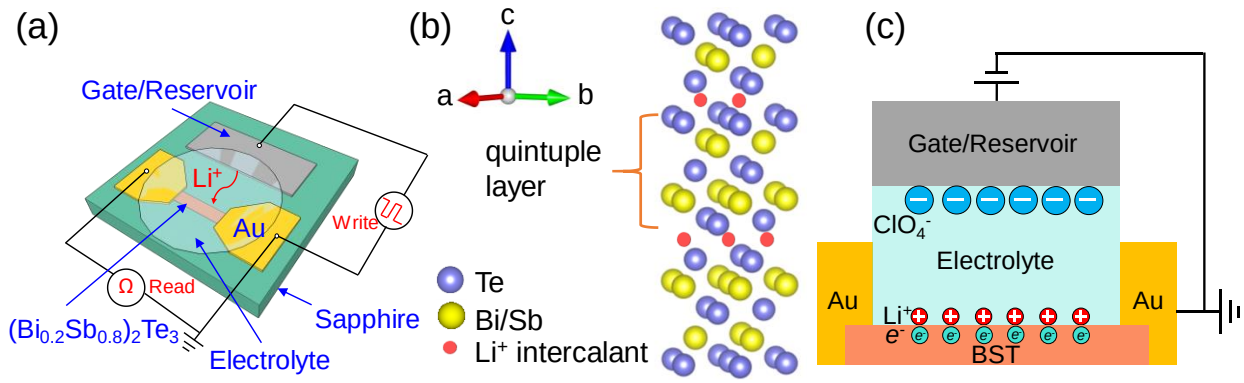

Figure 2.1. TI based dynamic synapse. Schematics of a) $(Bi_{0.2}Sb_{0.8})_2Te_3$ (BST) based synaptic device; b) Charge transfer doping through Li intercalation for long-term plasticity. c) Ionic gating for short-term plasticity.

2.2.2 Materials Characterization of Molecular Beam Epitaxy Grown BST

High-quality epitaxial BST films were grown on (0001) sapphire substrates in an ultra-high vacuum Perkin Elmer MBE system at 200 °C substrate temperature. We performed in-situ reflection high energy electron diffraction (RHEED) to monitor the surface of the growth film.

The periodic intensity oscillation at a single spot during the MBE growth indicates the layer-by-layer growth, where each intensity peak represents the formation of a new QL.[168] Our film thickness is around 6.5 QLs, as indicated in **Figure 2.2a**. The inset RHEED pattern in Figure 2.2a demonstrates the high-quality growth of the atomically flat BST film. To ensure a good crystal structure of the BST film, we performed X-ray diffraction (XRD), as shown in Figure 2.2b, where the characteristic peaks of the grown BST film agreed well with those reported previously.[169]

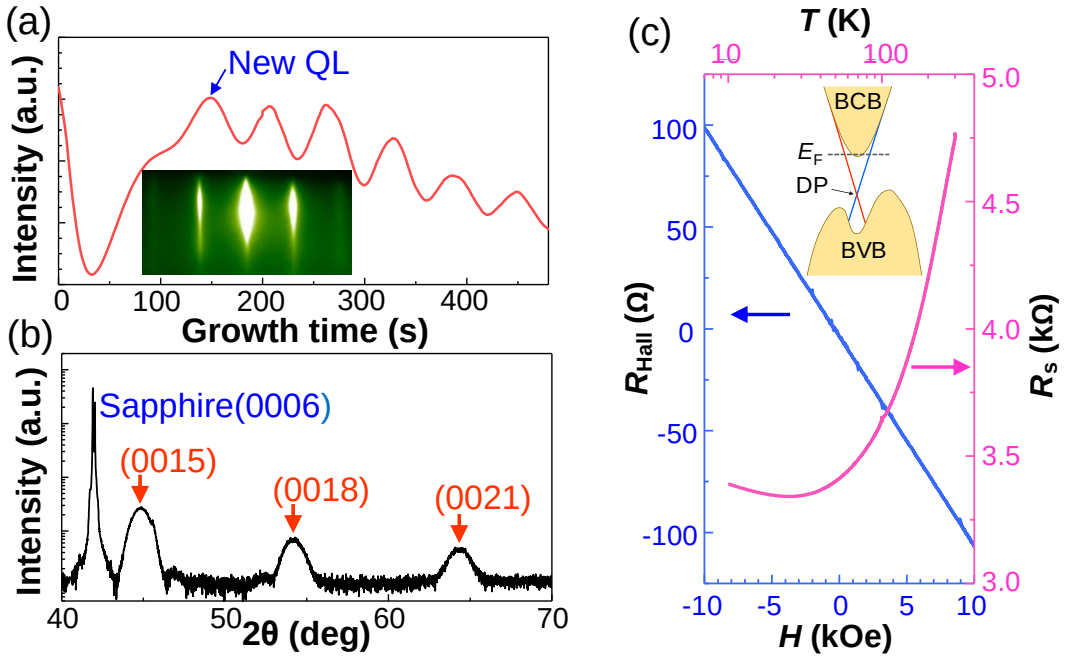

Figure 2.2. Characterization of the MBE grown BST film. a) RHEED oscillations indicating layer-by-layer growth and a film thickness around 6.5 QLs (i.e. ~6.5 nm). The insert is the RHEED pattern, suggesting high quality growth. b) XRD of the BST film on sapphire substrate. c) Transport measurement of the BST Hall-bar structure (0.5×1 mm^2). The red curve shows the sheet resistance R_s as a function of temperature from 300 K down to 10 K and the blue curve shows how the hall resistance R_{Hall} changes as a function of the out-of-plane magnetic field H, where the calculated density of state is $n_{2D} = 6 \times 10^{12}$ cm^{-2}. The insert shows the schematic of the band structure and position of the Fermi level.

2.2.3 Electrical Characterization of BST Film

Ternary $(Bi_xSb_{1-x})_2Te_3$ can exhibit different Dirac band structures with different values of x, and thus manifesting distinctive transport properties.[159] Through the measurement of transport properties (Keithley 6221 and Stanford SR830 amplifier) of the BST film, we can estimate the stoichiometric ratio of Bi to Sb and Dirac band structure for our BST film. Figure 2.2c shows the BST sheet resistance (R_s) as a function of temperature and the relationship between the hall resistance (R_{Hall}) and the out-of-plane magnetic field (H) properties of the patterned Hall-bar BST device (0.5×1 mm^2). By comparing the sheet resistance and hall resistance curve with reported relationships in the literature,[159, 170] we estimated x = 0.2 for our $(Bi_xSb_{1-x})_2Te_3$ sample. The inset in Figure 2.2c shows the Dirac band structure of our BST film, where Dirac Point (DP) and E_F lie within the bulk energy bandgap between the bottom edge of bulk conduction band (BCB) and the top edge of bulk valence band (BVB).[159, 170] We choose x = 0.2 in $(Bi_xSb_{1-x})_2Te_3$ for this work so that the BST synapse can achieve a larger dynamic range with a more insulating initial state.

2.3 Electrochemical Characterization of BST During Li Intercalation

2.3.1 Galvanostatic Discharge of BST Film

The reversible electrochemical intercalation process is illustrated in **Figure 2.3a**, where the polarity of the current flow in the external circuit determines if Li^+ ions are driven into (purple arrows) or out of (red arrows) the BST lattice. An advantage of this approach is that the ionic concentration (and hence the carrier concentration and the synaptic weight) can be precisely

controlled, as the amount of Li^+ ions moving into/out of the BST synapse equals to the amount of electrons (e^-) transferred in the external circuit – as governed by charge neutrality.[47, 171] This can also contribute to a more linear and symmetric weight update, as the amount of increase in carrier concentration from each identical writing pulses will be the same – another desirable trait that can improve the learning accuracy of the artificial neural network.

Figure 2.3b demonstrates the galvanostatic discharge measurement (through a BioLogic SP-200 workstation) of the BST device by applying a constant discharging current (50 nA) for electrochemical Li intercalation. The electrochemical potential of BST first decreased monotonically as Li ions were intercalated into the BST lattice[171] until it reached a plateau at ~-1.15 V vs. LFP. While the physical origin of this plateau in intercalated BST is unclear and requires further theoretical calculations and analysis,[172] voltage plateaus in the galvanostatic discharge measurement are often associated with structural changes for 2D materials such as the stage transformation in graphene[47, 173] and the 2H to 1T phase transformation in MoS_2.[171, 174]

2.3.2 In-Operando Raman Spectra of BST Film during Intercalation

In order to gain a better understanding of the electrochemical intercalation process, we performed in-operando Raman spectroscopy (Horiba LabRam with a 473 nm) on a BST film under different ionic (Li^+) concentrations, as shown in Figure 2.3c. For pristine BST (before Li intercalation), we observed two prominent peaks at ~111 cm^{-1} and 160 cm^{-1}, corresponding to the in-plane (E_g^2) and out-of-plane (A_{1g}^2) vibration modes, respectively, as others have reported in the literature.[167, 169, 175] Upon Li intercalation, we noticed that a new peak (~122 cm^{-1}) started to appear when the BST's electrochemical potential is at -1.15 V vs. LFP, corresponding to the

voltage plateau we observed in the galvanostatic discharge process (Figure 2.3b). Analogously to the new peak observed in Cu-intercalated Bi_2Se_3,[167] we speculate that this new peak likely stems from the formation of extra bonding between intercalated ions and host TI materials though further investigations are needed to identify the exact origin of the peak.

2.3.3 Electrical Conductance Response of BST Film upon Li Intercalation

To characterize the dynamic range of the BST synapse, we monitored the change in BST channel conductance (G_{DS}) during the electrochemical intercalation process by applying a 10 mV read voltage between the source and drain terminals. The read voltage was kept small to minimize any potential inhomogeneity in ionic concentration in the BST channel. The channel conductance showed a steady and linear increase from ~50 μS to 65 μS, as we carried out the Li intercalation (Figure 2.3d). This 130% dynamic range is less than ideal as it would require an intricate peripheral circuitry for readout, potentially negating the advantages of having a high precision synapse. Thus, further investigations need to be carried out to improve the dynamic range of the electrochemical synapse, such as through tuning the stoichiometry in BST or exploring similar layered topological insulators with a more insulating pristine state and/or a higher capacity for intercalated ions. In addition, careful device design (e.g., optimizing the device geometry/resistance and the precision level) are needed to ensure that the resistance difference between adjacent states is sufficiently high to be easily distinguished by the peripheral circuitry.

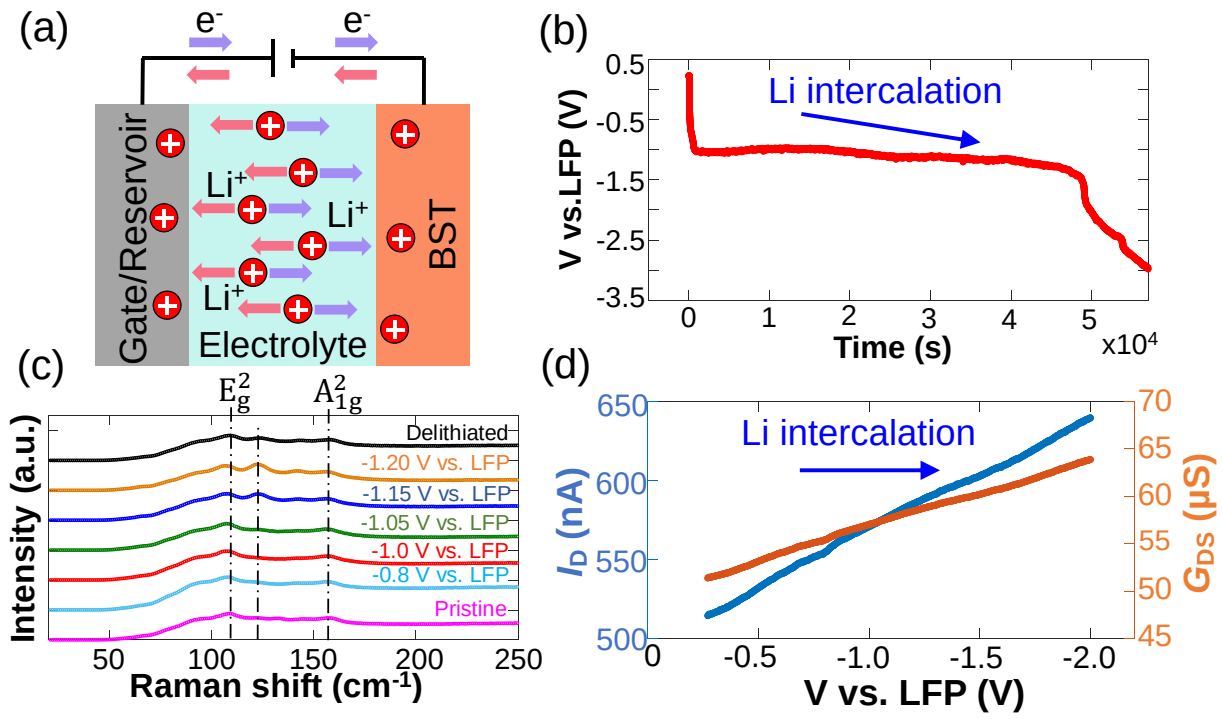

Figure 2.3. In-operando Raman spectra and electrical characterization of BST devices. a) The schematics of the reversible electrochemical Li intercalation/de-intercalation process. b) Galvanostatic discharge of BST with a constant discharging current (50 nA). c) Raman spectra of intercalated BST films at different electrochemical potentials (i.e. ionic concentrations). d) Current and conductance response of the BST film (under a 10 mV read voltage) upon Li intercalation.

2.4 Neuronal Functionality of BST Electrochemical Synapses

2.4.1 Long-Term Plasticity (LTP) and Short-Term Plasticity (STP)

We performed single pulse measurement (Keithley Semiconductor Characterization System 4200A with Pulse Measuring Units) on the BST synapse to demonstrate basic potentiation and depression functions and elucidate the long-term and short-term effects. As shown in **Figure**

2.4a, synaptic potentiation can be achieved by sending a positive current pulse (5 nA, 10 ms) from the gate terminal to the BST channel, which has an initial conductance G_0 at ~50 μS and a channel dimension of ~130 μm (L) × 20 μm (W) × 6.5 nm (t). We observe a significant increase in synaptic weight (ΔG ~1 μS or 2% of G_0) immediately upon the potentiation pulse, due to the combined effect from charge transfer doping and ionic gating (Figure 2.1b and 2.1c). At the end of the programming pulse, the channel conductance gradually decayed as the electric double-layer and its associated doping effect dissipated – analogous to the short-term plasticity behaviors in biological synapses.[176] Unlike the volatile ionic gating effect, the charge transfer doping from the electrochemically intercalated Li^+ ions is non-volatile, as we still observe a long-term increase in the synaptic weight ΔG_{LT} when the channel conductance stabilizes – mimicking the long-term plasticity in biological synapses. We observe similar short-term and long-term dynamics in the depression step (-5 nA, 10 ms), where the time-dependent change in synaptic weight [ΔG(t)] consists of a constant long-term component ΔG_{LT} and a volatile short-term component [ΔG_{ST}(t)] such that $\Delta G(t) = \Delta G_{LT} + \Delta G_{ST}(t)$.

2.4.2 Programmable LTP Using Single Pulse

This built-in temporal component in our electrochemical BST synapse mimics the spatio-temporal dynamics in biological synapses and can be useful to realize causality and logical inference. We further explore how we can engineer the spatio-temporal response by tuning both the amplitude and timing constant of the ΔG(t). The amplitude of the long-term weight change ΔG_{LT} due to charge transfer doping depends on the increase in carrier concentration (Δn), which in turn scales linearly with the increase in ionic concentration that is dictated by the total charge

transferred (= pulse amplitude (I_G) × width (t_w)) in the programming pulse. Indeed, we observed a pseudo-linear increase in ΔG_{LT} as we increased the amplitude of the current pulse from 5 nA to 100 nA (Figure 2.4b), due to the increase in ionic and carrier concentrations in the BST channel. We also varied the pulse width from 10 ms to 60 ms (Figure 2.4c), where we observed a similar pseudo-linear trend in ΔG_{LT} when the pulse width was less than 20 ms. We plot the combined results in Figure 2.4d, where ΔG_{LT} scales almost linearly when the total charge in the programming pulse is less than 1600 pC and gradually saturates beyond that point. This saturation behavior is likely because that with the fixed potential difference between the gate terminal (LFP) and BST during programming, the BST film can only accommodate a limited amount of Li^+ ions, dictated by the electrochemical potential difference, which is in turn set by the pulse amplitude. This linear relationship between ΔG_{LT} and pulse amplitude/width suggests promising tunability for our BST synapses.

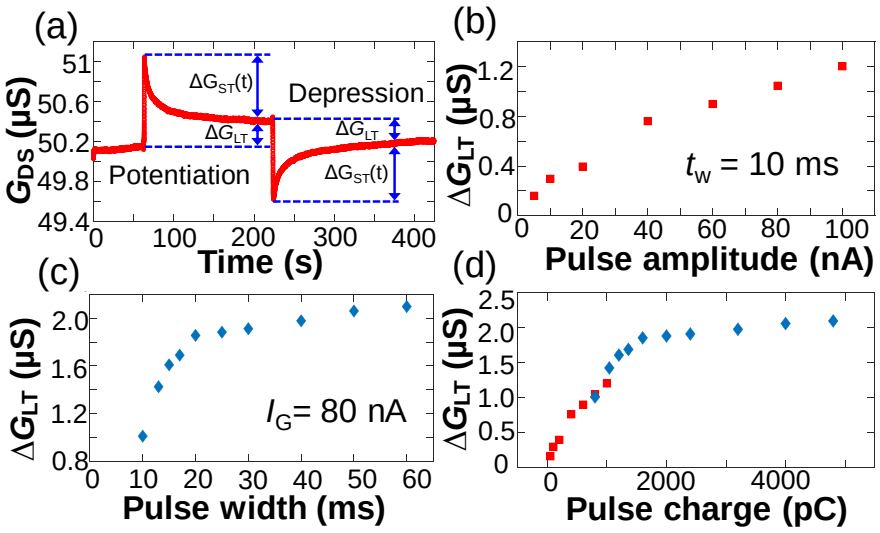

Figure 2.4. Single-pulse response showing programmable short-term and long-term plasticity. a) Potentiation and depression responses from the BST synapse with both short-term and long-term components. The amplitude of the long-term plasticity as a function of b) the pulse amplitude; c) the pulse width; d) the total charge (= pulse amplitude × width).

2.4.3 Paired-Pulse Facilitation (PPF) of BST Synapses

Leveraging the unique dynamics of our BST synapse, we demonstrate paired pulse facilitation, an important neuronal function in biological synapses,[176] through a two-pulse programming scheme. In PPF, two consecutive current pulses are sent to the synapse at a time interval Δt apart, where the increase in synaptic weight upon the second pulse is a function of Δt, as illustrated in **Figure 2.5a** inset. This dynamic is often characterized in the PPF ratio, which is defined as the ratio of the current level after (I_2) and before (I_1) the second programming pulse. We varied the time interval between two identical potentiation pulses (5 nA, 10 ms) from 10 to 1000 ms to investigate how the PPF ratio in our electrochemical synapse changed as a function of Δt, as shown in Figure 2.5a. We observe an exponential decay in the PPF ratio, which can be modeled using a three-term exponential decay function $I_2/I_1 = 1 + C_1\exp(-\Delta t/\tau_1) + C_2\exp(-\Delta t/\tau_2) + C_3\exp(-\Delta t/\tau_3)$.

The three time constants are τ_1 = 50 ms, τ_2 = 310 ms, and τ_3 = 3000 ms for this BST device, similar to previously the time scale in biological synapses[176] and previously reported artificial synapses[12, 47, 177, 178] involving ionic movements. We speculate that the two smaller time constants (τ_1 and τ_2) depend on the BST channel width (20 μm) and length (50 μm), while the larger τ_3, due to the presence of our ionic reservoir (LFP), depend on the distance between the LFP gate and the BST channel (~150 μm), originating from the ion diffusion process. We repeated the PPF measurements on BST synapses with different geometries (from 7 μm to 200 μm) and fit a power law dependence ($\tau \sim L^{2.03}$) between the time constants and the device dimensions (Figure 2.5b), consistent with the diffusion kinetics governed by Einstein's diffusion equation $\tau_D = L^2/2D$, where τ_D, L, and D denote the diffusion time, dimension, and diffusion coefficient,

respectively.[47] This suggests that the temporal dynamics in the PPF ratio and the short-term plasticity in electrochemical synapses depend on the ionic diffusion process, similar to previously reported results. This offers an excellent opportunity for us to engineer the time constants and hence the spatio-dynamics of our BST synapses by changing the device dimensions, and at the same time indicates good scaling potential of the electrochemical synapse, as the switching time scales approximately to L^2.

2.4.4 Scaling Performance of BST Synapses

We further study the scalability of the BST synapse in terms of switching energy, as shown in Figure 2.5c. The switching energy (needed to induce a 0.4% $\Delta G_{LT}/G_0$ change) scales linearly with the channel area (= $L \times W$), since the weight change depends on the ionic concentration, i.e., the amount of charge transferred per unit area. The switching energy for our smallest device (70 μm × 7 μm × 6.5 nm) is 18 pJ. Estimating from scaling trends in switching speed and energy, we project the programming speed and energy for a nanoscale device (25 nm × 25 nm × 6.5 nm) to be ~100 ns and ~28 aJ – providing significantly better energy efficiency than existing CMOS devices.

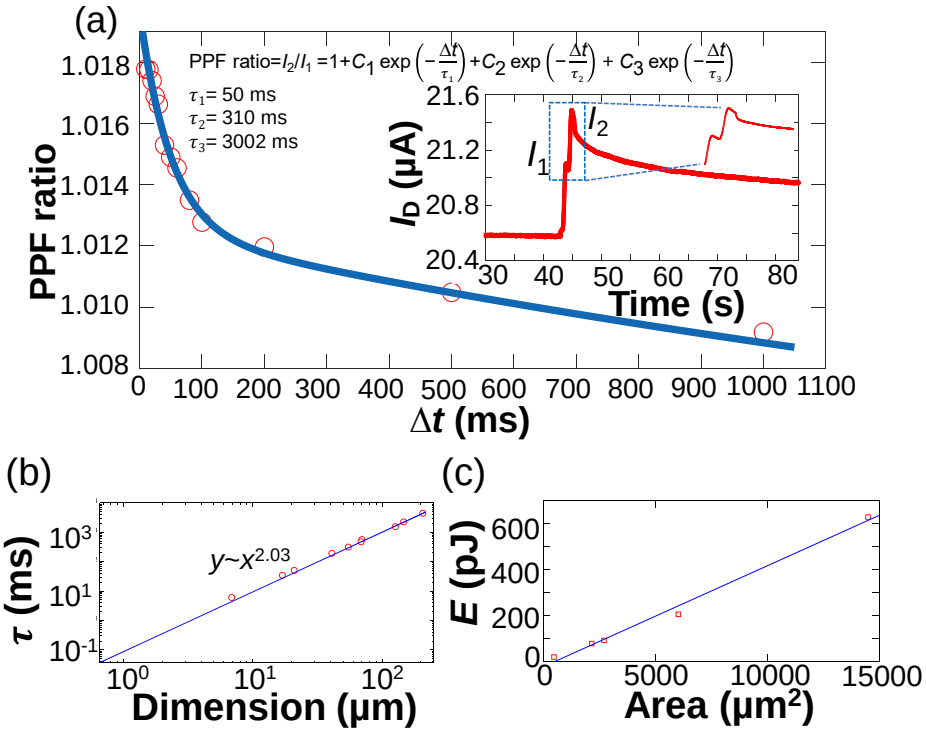

Figure 2.5. Paired-pulse facilitation and the scaling behavior of the BST synapse. a) The PPF response can be fitted with a three-term exponential function with three time constants (50 ms, 310 ms, 3000 ms). The inset demonstrates two consecutive pulses (I_G = 5 nA, t_w = 10 ms, Δt = 10 ms). b) The time constants (τ) show a power law dependence with the device dimension (L) such that $\tau \sim L^{2.03}$. c) The scaling trend of the switching energy as a function of the BST device area.

2.5 Synaptic Device Performance of BST Synapses for ANNs

2.5.1 Long-Term Potentiation and Long-Term Depression

Besides programmable spatio-temporal dynamics and good scaling potential, our BST synapse also exhibits high precision (~500 states per device) as well as a linear and symmetric conductance response – improving the areal density and learning accuracy of ANNs.[33, 179, 180]

Figure 2.6a demonstrates the long term potentiation and depression of our BST synaptic device through consecutive current pulses. We observe decent linearity and symmetry in the conductance response. We employ current pulses for programming because it allows us to achieve precise control over the amount of charge transferred during a single programming pulse and hence enabling a linear conductance response in the BST synapse. In the future, we plan to adopt similar materials for both the gate and the channel materials to minimize the electrochemical potential difference between the two, paving towards the simpler voltage control circuitry for programming while maintaining good linearity.

2.5.2 Tunable Synaptic Precision

By utilizing different current pulses, our BST synapse also demonstrates tunable precision (e.g., 100, 150, and 500 states) and dynamic range (Figure 2.6b). While the dynamic range in the BST synapse needs be improved for us to enjoy the full benefits of a high precision synapse, our proof-of-concept work demonstrates the potential for high precision with good linearity in electrochemical synapses, because its underlying programming mechanism is the controllable charge transfer doping – in contrast to some of the more stochastic and abrupt processes in emerging memory devices (such as filamentary formation in RRAMs[181] and threshold switching in PCMs[182]). We observe a trade-off between dynamic range and linearity/symmetry, where the linearity and symmetry of the synapse deteriorate slightly when we push the synapse to a larger dynamic range, likely associated with the saturation of BST's capacity to accommodate Li^+ ions.

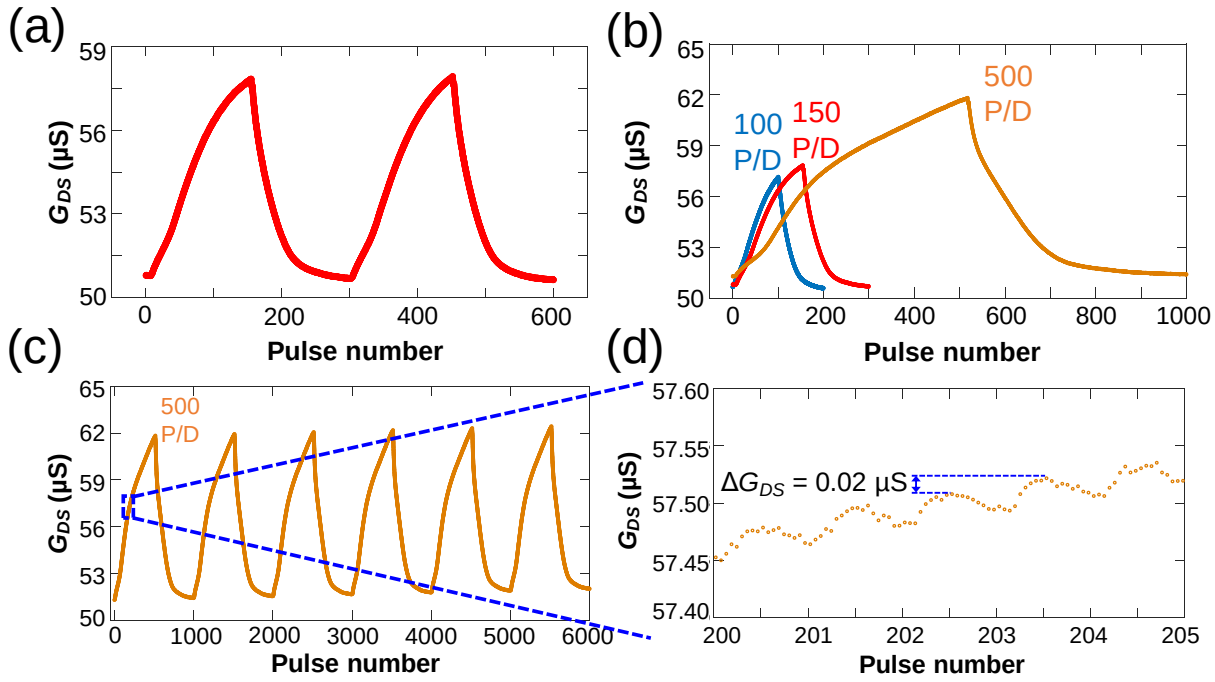

Figure 2.6. BST synapses with good precision, linearity, and distinct states. a) A train of pulses (150 potentiation and depression or (P/D) pulses with $I_G = \pm 1$ nA, $t_w = 10$ ms, $\Delta t = 1$ ms) demonstrating long term potentiation and depression with high precision, good linearity and symmetry. The conductance was measured with a 0.5 V read voltage. b) Tunable synaptic precision in the BST synapse with up to 500 P/D pulses demonstrated (~8-bit precision). c) Consecutive cycles of potentiation and depression pulses, demonstrating potentially low device variations. d) The zoom-in panel indicates distinct conductance states.

2.5.3 Distinct Conductance States

To further explore the device variation, we performed consecutive pulse measurements with over 6000 potentiation and depression pulses (Figure 2.6c), where we observed good reproducibility. The zoom-in panel in (Figure 2.6d) shows distinct conductance states, though a larger difference between adjacent states is preferred to improve the sensitivity and minimize readout errors.

2.5.4 Device Variations

We investigated both the spatial (device-to-device) and temporal (cycle-to-cycle) variations in our BST synapses since device variation plays a vital role in achieving high learning accuracies in high-precision synaptic arrays. In **Figure 2.7a**, we plotted the maximum and minimum conductance states for 20 BST synapses with identical geometries, where we observed an overlapping conductance range for all devices from 53 μS to 60 μS. We further characterized the ΔG in 10 devices upon an identical programming pulse starting from $G_0 = 53$ μS in Figure 2.7b. While the variation in ΔG ($\sigma/\mu = 1.47\%$) for BST synapses need to be improved via better process optimizations to minimize the write noise, we are encouraged by the potential of the electrochemical synapse as high-precision synapses due to its capability of incremental conductance change. In Figure 2.7c, we studied the endurance performance of the BST synapse over 100 cycles, where each cycle consisting of 300 potentiation and depression (P/D) programming pulses ($I_G = \pm 1$ nA, $t_w = 10$ ms), where we observed fairly consistent programming characteristics. We plotted the cycle-to-cycle variations of ΔG ($\sigma/\mu = 0.98\%$) per a single programming pulse ($I_G = 1$ nA, $t_w = 10$ ms) starting from 53 μS in Figure 2.7d, confirming the potential for low device variation in the electrochemical synapse.

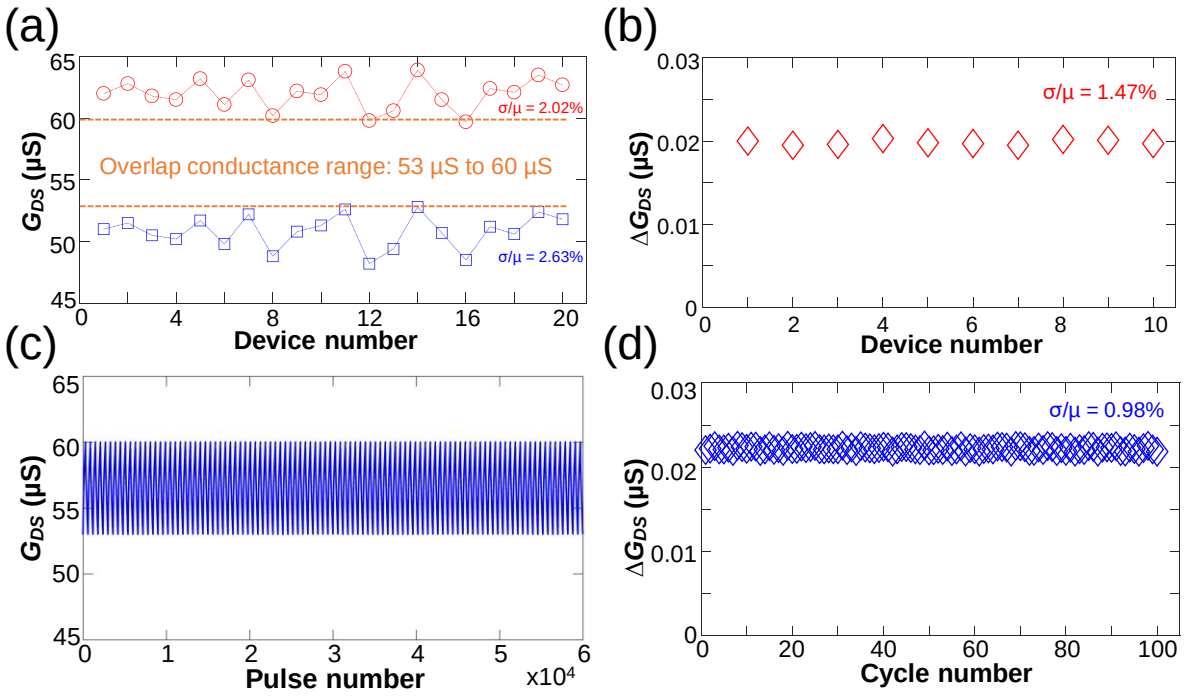

Figure 2.7. BST device variations. a) The distribution of the maximum and minimum conductance states for 20 BST synapses with the same geometry, showing an overlapping conductance range from 53 μS to 60 μS. During programming, 500 P/D pulses with I_G = ±1 nA, t_w = 10 ms, Δt = 1 ms were applied to each device. b) The distribution of ΔG upon a single programming pulse (I_G = 1 nA, t_w = 10 ms) from an initial conductance of 53 μS for 10 BST synapses. c) Endurance performance of a BST synapse over 60, 000 programming pulses (or 100 cycles consisting 300 P/D pulses per cycle) from an initial conductance of 53 μS. d) The cycle-to-cycle variation of ΔG upon a single programming pulse (I_G = 1 nA, t_w = 10 ms) from an initial conductance of 53 μS over 100 cycles.

2.5.5 Benchmark BST Synapses Performance in DNNs

To gain an idea of the performance of our BST synapses, we modelled an idealized 2-layer multilayer perceptron (MLP) crossbar array using MLP simulator (+Neurosim).[38, 183] Due to the ON/OFF ratio required for the program to model analogue synapses, digital synapses with appropriate R_{on} and R_{off} were used with the number of digital bits simulating the number of states per synapse. Due to this compromise, the amount of noise in the system is negligible compared to

what a real network would experience, but this figure of merit is good for a first order approximation. This idealized network achieved a 93% learning accuracy after 125 training epochs when identifying the handwritten MNIST digits[184] as shown in **Figure 2.8**. Although this simulation is only a first order approximation, there is still lots of room for optimization in physical network structure as well as learning algorithm utilization, so while a physical ANN using these devices might not meet the 93% reported here, we have confidence that these BST synapses will still be a promising candidate for future real-world applications.

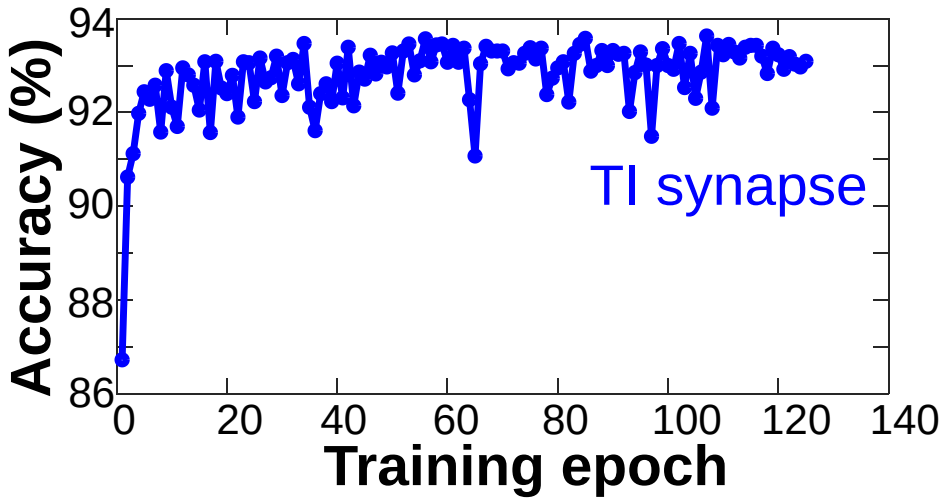

Figure 2.8. Neural netwrok simulation using BST synapses. MNIST simulation results (up to 93% accuracy with 125 epochs) using the BST synapse (with a precision of 100 states per device) in a cross-point 2-layer multilayer perceptron (MLP) neural network.

2.6 Conclusion

In summary, we develop the first electrochemical synapses based on ternary TI $(Bi_{0.2}Sb_{0.8})_2Te_3$ with programmable spatio-temporal dynamics (both amplitude and time constant), suitable for implementing neurorealistic artificial neural networks. We demonstrate basic neuronal

functions such as short-term and long-term plasticity as well as paired-pulse facilitation, utilizing the built-in temporal component in our BST synapse. The BST synapse shows good scaling potential with a projected switching speed and energy at 100 ns and 28 aJ at nanoscale dimensions (∼25 nm). The high precision (500 states per device), decent linearity, and symmetry in the weight update further improve the learning accuracy (93%), when BST synapses are benchmarked with the MNIST dataset. Our work elucidates the fundamental electrical and ionic transport in electrochemically intercalated TI devices and develops an energy efficient dynamic synapse that can potentially lead to the hardware acceleration of the neurorealistic artificial neural network, significantly improving the energy efficiency and cognitive capability of computing systems.

3.0 Low-Voltage Electrochemical Li_xWO_3 Synapses (LiWES) for SNNs

3.1 Motivation

Neuromorphic computing has the great potential to enable faster and more energy-efficient computing by overcoming the von Neumann bottleneck. However, most emerging NVMs based artificial synapses suffer from insufficient precision, nonlinear synaptic weight update, high write voltage, and high switching latency. Moreover, the spatio-temporal dynamics, an important temporal component for cognitive computing in SNNs, are hard to generate with existing CMOS devices or emerging NVMs. Herein, a three-terminal, Li_xWO3-based electrochemical synapse (LiWES) is developed with low programming voltage (0.2 V), fast programming speed (500 ns), and high precision (1024 states) that is ideal for artificial neural networks applications. Time-dependent synaptic functions such as PPF and temporal filtering that are critical for SNNs are also demonstrated. In addition, by leveraging the spike-encoded timing information extracted from the STP behavior in the LiWES, an SNNs model is built to benchmark the pattern classification performance of the LiWES, and the result indicates a large boost in classification performance (up to 128×), compared with those NO-STP synapses.

3.2 Design of Low-Voltage Electrochemical LiWES

In the previous chapter, BST based electrochemical synapses exhibit a programmable spatio-temporal response governed by a combination of long-term charge transfer doping and

short-term ionic gating effects, a high precision (>500 states per device), and a linear and symmetric weight update. However, voltage programming pulses are favored to be implemented for modulating the spatio-temporal dynamics of synapses.[33, 179] Moreover, reducing programming voltage amplitude and increasing programming voltage speed at synaptic device level are necessary to lower the latency and energy consumption during the training and inference of the neural networks.[185]

Thus, in this chapter, we develop a three-terminal LiWES with low-programming voltage (i.e. ~0.2 V enabled by our self-gated design[13] with near-zero open circuit voltages (OCVs) between the gate and the channel), fast programming speed (500 ns), and high precision (1024 states) that is ideal for DNNs. We also demonstrate time-dependent synaptic functions such as paired-pulse facilitation and temporal filtering that are critical for SNNs. In addition, by utilizing the time-encoded spikes in our LiWES dynamic synapses, we build a SNNs model to benchmark the pattern classification performance, which shows a large boost (128× improvement) in classification performance in highly time-dependent scenarios.

3.2.1 Advantages of WO_3-based Li-ion Electrochemical System

Tungsten oxide (WO_3), consisting of corner-sharing [WO_6]-octahedral structures, can be considered as a pseudo-perovskite oxide with absent A-site cations.[186, 187] The absence of A-site cations can be used as interstitial space for ion intercalation and extraction,[188-190] thus making WO_3 a good candidate for electrochemical synapses. Moreover, insulator-to-metal transition has been demonstrated in epitaxial WO_3 film via electrolyte gating,[191-194] which provides a large conductivity modulation window for building high-precision synapses with a large dynamic range that are ideal for neuromorphic computing applications.[195] Another advantage of using WO_3 film

as the channel material is that the high quality epitaxial WO_3 film can be deposited by radio-frequency (RF) magnetron sputtering,[160, 194] providing a route towards scalable fabrications that enable the wide-spread of smart electronics in the era of the Internet of Things (IoTs).

While WO_3-based electrochemical synapses have demonstrated promising potentials in prior pioneering studies,[196-198] more research efforts are necessary to lower the programming voltage (e.g. 4 V[198]) and improve the programming speed (e.g. 70 ms[196]), two key parameters in artificial synapses. In addition, most of the prior works on WO_3-based electrochemical synapses have been focused on improving the precision for DNNs applications with little to no effort devoted to producing time-coded spikes that are critical for SNNs applications.

3.2.2 Epitaxial Growth and Materials Characterization of WO_3 Film

Epitaxial tungsten oxide (WO_3) thin films were deposited on (100) $LaAlO_3$ substrates (MTI Ltd.) using radio-frequency (RF) magnetron sputtering with WO_3 target (99.99% purity from Sigma-Aldrich). A total RF power of 80 W was used. The process pressure was kept at 60 mTorr with a gas ratio of 1:2 for Ar : O_2, while the deposition temperature was kept at 650 °C to achieve a deposition rate at 1 nm per min. The resulting WO_3 film thickness was 60 nm, measured by a surface profiler (KLA-Tencor AlfaStep IQ).

For the characterization of the as-deposited epitaxial WO_3 film, XRD (**Figure 3.1a**) and atomic force microscopy (AFM) (Figure 3.1b) measurements were used to confirm the good crystallinity of the deposited WO_3 film with an atomically-flat surface (root-mean-square roughness < 600 pm). The Bruker D8 Discover instrument was used for XRD measurement. The WO_3 film sample for XRD was annealed at 650 °C in air for 1 hour. The asylum MFP-3D was used for AFM measurement and a scan area of 1 μm × 1 μm was chosen for surface roughness

analysis. Having a high-quality, crystalline thin film with a smooth surface is critical for promoting the conductance modulation efficiency in our electrochemical synapse, which involves the electrolyte gating process that is sensitive to the surface smoothness.[160, 194]

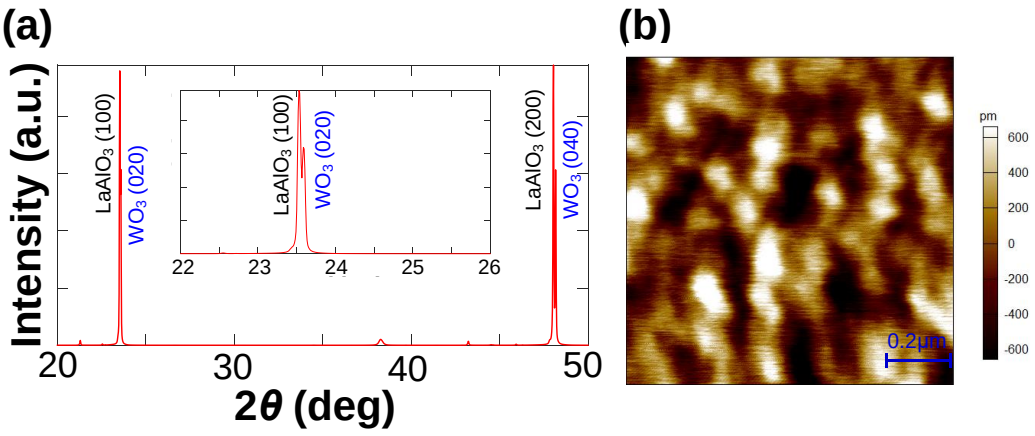

Figure 3.1. Characterization of the epitaxial WO_3 film on $LaAlO_3$ (100) substrate. Characterization of the epitaxial WO_3 film on $LaAlO_3$ (100) substrate. a) XRD of the epitaxial WO_3 film on $LaAlO_3$ (100) substrate. b) AFM image of the epitaxial WO_3 film, showing the atomically flat surface with an rms roughness less than 1 nm.

3.2.3 Low-Voltage Self-Gate Design and Fabrication of LiWES

The structure of our LiWES is similar to that of biologic synapse, as illustrated in **Figure 3.2a**. In a biologic neural network, a synapse is the small gap (20-40 nm) between a pre-synaptic neuron and a post-synaptic neuron. This connection strength is referred to as the synaptic weight, which can be increased (potentiation) or decreased (depression) by modulating the Ca^{2+} concentration. The electrical signal from pre-synaptic neurons activates the opening of calcium channels, triggering the release of neurotransmitters from pre-synaptic neurons into post-synaptic neurons. The schematic of our three-terminal LiWES is shown in Figure 3.2b, where the channel conductance, modulated by the gate terminal, represents the synaptic weight. Tungsten oxide,

which contains a large number of vacant A-sites, is ideal for reversible intercalation and de-intercalation of Li ions (Li^+), as evident in its wide use in commercial electrochromic devices.[199] By intercalating (extracting) Li^+ into (out of) the Li_xWO_3 channel, we can potentiate (depress) the synaptic weight (represented by the channel conductance) of our synapse.[7, 14] An optical image of the electrochemical synapse is shown in Figure 3.2c, depicting a three-terminal planar transistor structure where WO_3 thin films (60 nm) are deposited on $LaAlO_3$ (100) substrate as both the gate and the channel. During the deposition of WO_3 film, a shadow mask was used for patterning. Devices of different channel areas (from 1000 × 200 μm^2 to 200 × 50 μm^2) were fabricated for variation study. For the electrical characterization and pulse measurement, devices of 400 × 200 μm^2 channel area were used. Au contacts (100 nm) with a Ti adhesion layer (5 nm) were deposited using an electron-beam evaporator and patterned by a shadow mask. The deposited Ti/Au metal contacts are on top of the as-grown WO_3 film. Adopting the same material for both the gate and the channel allows us to minimize the OCV between the two terminals,[13] hence achieving a low programming voltage.

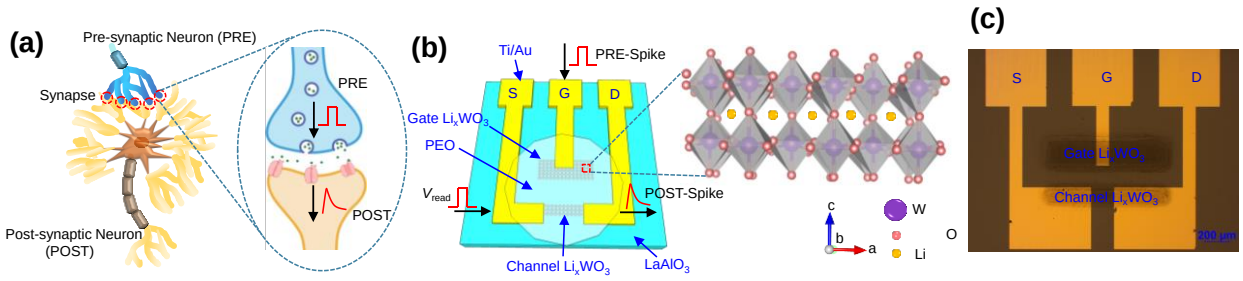

Figure 3.2. Low-voltage self-gate design of LiWES. a) Biologic neuron and synapse structure. b) Schematic of our LiWES and the inset shows the crystal structure of WO_3 octahedrons. c) Optical image of the LiWES without electrolyte coating.

3.3 Electrochemical Characterization of Li_xWO_3 During Li Intercalation

3.3.1 Electrochemical System of LiWES

In **Figure 3.3**, we employ $Li_{0.6}FePO_4$ (LFP) as the Li^+ ion reservoir as well as the reference gate for us to modulate the Li content in both the Li_xWO_3 channel and self-gate, since it provides a near-constant electrochemical window (~3.4 V vs. Li/Li^+ as LFP's Li content changes from $Li_{0.02}FePO_4$ to $Li_{0.9}FePO_4$) to ensure stable operations.[161, 162, 200] The reference gate LFP was placed about 2 mm away from the WO_3 channel. The LFP gate was prepared by manually coating the LFP slurry[13] onto a Au contact pad. The PEO electrolyte was prepared by mixing 30 wt % $LiClO_4$ (Sigma-Aldrich) with poly(ethylene oxide) (molecular weight 600, 000 from Sigma-Aldrich) in acetonitrile solvent. Subsequently, the PEO electrolyte (~ 1 μm)[201] was drop-casted to cover both the WO_3 gate/channel and the LFP reference gate. The PEO serves as an electrolyte for Li^+ ions transport in both cases: Li_xWO_3 self-gate and channel, LFP gate and Li_xWO_3 channel. The difference between self-gate and LFP gate is the OCV between gate and channel as well as the required programming voltage. To remove the residual solvent, the sample was heated at 80 °C on a hot plate overnight. All the chemical preparation and operation steps were performed in an Ar-gas glovebox. We can achieve controllable tuning of the Li_xWO_3 channel conductance (i.e. synaptic weight) via changing the Li content through reversible Li intercalation and de-intercalation, where Li intercalation/de-intercalation is a combination of non-volatile charge transfer doping and the volatile ionic gating effects.[7]

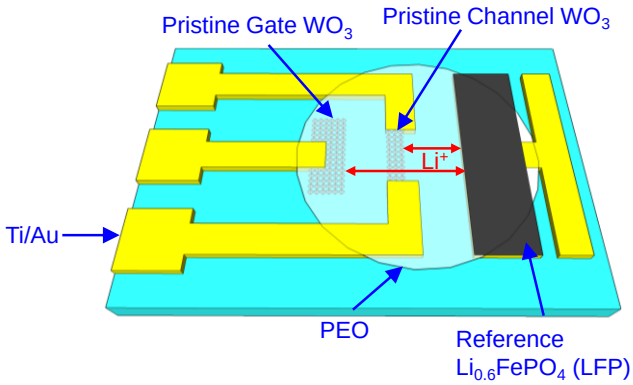

Figure 3.3. The schematic of electrochemical system of LiWES. Inspired by the Li-ion battery system, a all-solid electrochemical synapse is achieved with WO_3 film electrode (anode) and LFP reference (cathode), all covered with PEO polymer electrolyte.

3.3.2 Galvanostatic Discharge of WO_3 film During Li Intercalation

We first performed galvanostatic discharge measurements of WO_3 with a constant current of 0.1 nA to establish how the electrochemical potential of Li_xWO_3 relative to the standard potential of Li/Li^+ electrodes (V vs. Li/Li^+) changes as a function of the Li concentration (**Figure 3.4**). The measurement was carried out with an SP-200 Biologic workstation. A constant discharge/charge current of 0.1 nA was applied with the WO_3 channel connected to the working electrode and the LFP reference gate connected to the counter/reference electrodes. To convert the electrochemical potential of Li_xWO_3 (vs. LFP) to the potential (vs. Li/Li^+), a value of 3.4 V is added to the measured electrochemical potential of Li_xWO_3 (vs. LFP). Consistent with prior studies,[188, 190] the electrochemical potential of Li_xWO_3 decreases as Li content increases. The increase of the Li content in Li_xWO_3 film induces the phase transformation in a WO_3 crystal structure, where the voltage plateaus correspond to the phase separation as shown in M+T and T+C labeled regions in Figure 3.4. The voltage plateau in M+T region is less obvious largely likely

due to the fast discharge/Li intercalation process. An advantage of our electrochemical approach over conventional resistive memory based synapse is that it allows us to control the Li content (and hence the synaptic weight) in the channel accurately, enabling us to build high-precision, analog synapses[33, 195] that are desirable for DNNs applications.

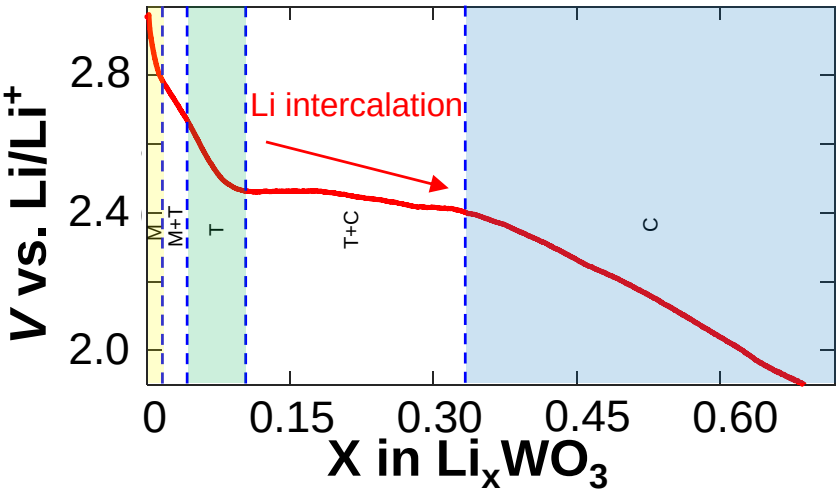

Figure 3.4. Galvanostatic discharge (intercalation) of WO_3 film. A constant current 0.1 nA during in-operando Raman spectra was used. The graph indicates the electrochemical potential of Li_xWO_3 change relative to the standard potential of Li/Li^+ electrodes (V vs. Li/Li^+) as a function of Li concentration.

3.3.3 Phase Transformation of WO_3 film During Li Intercalation

Previous studies suggest that Li intercalation can induce phase transformation in WO_3 crystal structure,[188, 190, 192, 193] where the Li_xWO_3 film goes through phase transformations from monoclinic ($0 < x < 0.01$), tetragonal ($0.05 < x < 0.12$), to cubic ($0.32 < x < 0.7$) with increased crystal symmetry as its Li content increases, partly accounting for the electrical properties change in Li_xWO_3 films.[188, 189, 192] As shown in Figure 3.4, non-linearity behavior exists due to the phase transformation of WO_3 crystal, which is why it is important to lithiate the WO_3 channel and

modulate its electrical conductance during the cubic phase region for obtaining a more linear response. We did in-operando Raman measurements[14] using the Horiba Scientific system with a 633 nm laser (1800 gr mm^{-1} grating). The absorbed laser power was kept low (< 5 mW) to avoid excessive laser heating. The Raman spectra in **Figure 3.5** suggests similar crystal structure changes during the lithiation process. Two strongest peaks in Raman spectra of WO_3 film are located at ~ 715 cm^{-1} and ~ 804 cm^{-1}, corresponding to the asymmetric and symmetric stretching vibrations of W^{6+}-O bonds, while the peak at ~278 cm^{-1} is due to the bridging O-W-O bonds.[202, 203] The intercalation of Li ions induces a larger lattice distortion, forcing the crystal structure to become more symmetric which leads to the gradual diminishing of the peak at 715 cm^{-1} as well as a blue shift of the peak from ~804 cm^{-1} to ~ 806 cm^{-1} resulting from the slightly decreased lattice parameters of Li_xWO_3 bronzes.[190]

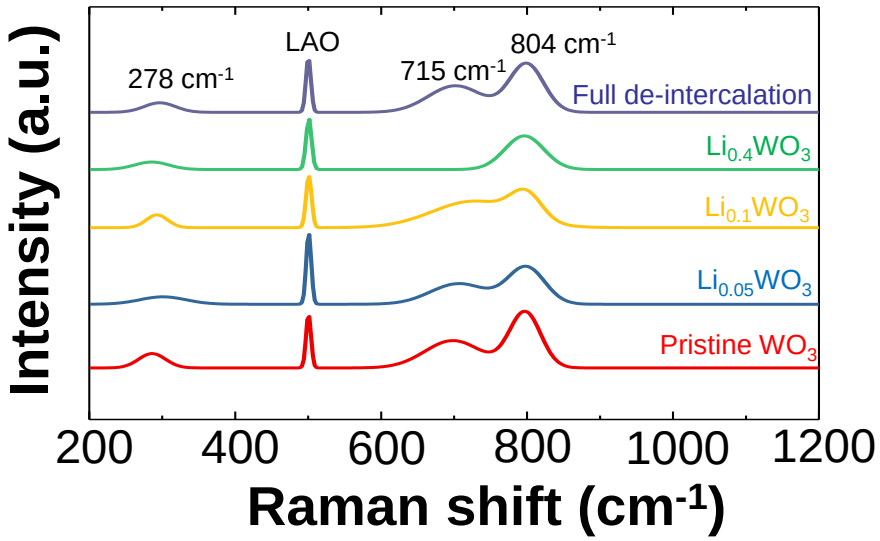

Figure 3.5. In-operando Raman spectra of WO_3 film. The result indicates a relatively reversible Li intercalation and de-intercaltion processes.

3.3.4 Tunable Electrical Conductance of WO_3 film

As illustrated in **Figure 3.6a**, the channel conductance increases monotonically as the Li concentration increases. This is likely because that Li ions can act as n-type dopants, increasing the channel conductance by shifting *s*-band high above the Fermi level with the charge-balancing electrons occupying the *d* conduction band in Tungsten.[189] The channel conductance can be continuously modulated over four orders of magnitude, suggesting a large dynamic range that is necessary for high-precision synapse. We note that the dynamic range becomes slightly smaller after the 1st cycle of intercalation/de-intercalation, likely due to a small amount of Li ions trapped inside the WO_3 host.[199] The conductance modulation windows between the two cycles are fairly consistent, indicating a repeatable dynamic range for synaptic weight updates.

We prepared a new LiWES device ($200 \times 50\ \mu m^2$) for exploring the repeatability of the conductance modulation during the Li intercalation/de-intercalation. During the test, a small DC reading voltage (0.1 V) was applied between the Source and Drain to continuously monitor the current/conductance level, while a gate dual-sweeping voltage ranging from 1.95 V to 2.75 V (*V* vs. Li/Li^+) was applied to the LFP for Li intercalation/de-intercalation. Up to 4 consecutive cycles of the conductance modulation can be seen in Figure 3.6b, further demonstrating the good repeatability of conductance modulation in our LiWES.

We fabricated a control sample without depositing WO_3 film and only deposited the Au (100 nm)/Ti (5 nm) metal contacts for Source and Drain. The reference gate LFP was placed about 2 mm away from the Source/Drain contacts and was manually coated with LFP slurry. PEO electrolyte was prepared[14] and drop-casted to cover both the Source/Drain contacts and LFP reference gate. The sample was heated at 80 °C on a hot plate to remove the residual solvent in Ar-gas glovebox. During the test, the sample was transferred into the vacuum probe station (JANIS

ST-500-UHT) and annealed at 350 K for ~2 hours to eliminate the residual moisture before the electrical measurements. During the test, a small DC reading voltage (0.1 V) was applied between the Source and Drain to continuously monitor the current/conductance level, while a gate dual-sweeping voltage ranging from 1.95 V to 2.82 V (V vs. Li/Li^+) was applied to the LFP for Li intercalation/de-intercalation. As shown in **Figure 3.7**, there is negligible current/conductance change during the gate dual-sweeping processes, which confirms that the 4 orders of magnitudes of conductance changes are due to the Li intercalation into WO_3 films, rather than electrical conductance changes of the PEO electrolyte.

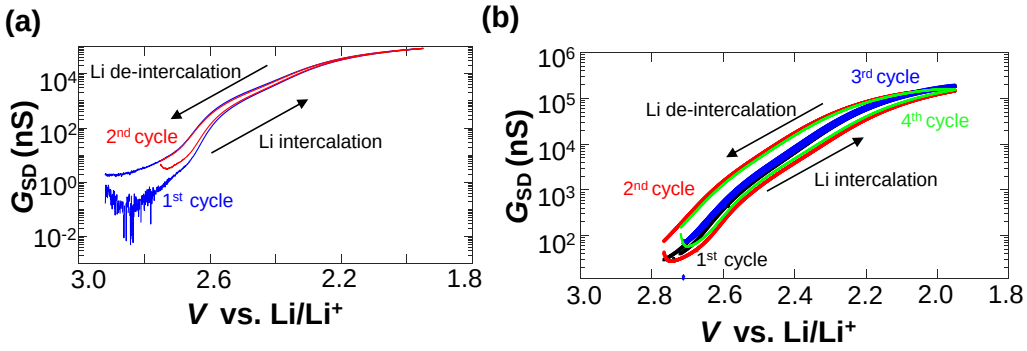

Figure 3.6. Tunable electrical conductance via modulating intercalated Li concentrantion. a) The electrical channel conductance change as a function of the electrochemical potential of Li_xWO_3 change during 2 cycles of Li intercalation/de-intercalation.b) The conductance change as a function of the electrochemical potential of Li_xWO_3 change during 4 consecutive cycles of Li intercalation/de-intercalation, demonstrating good repeatability.

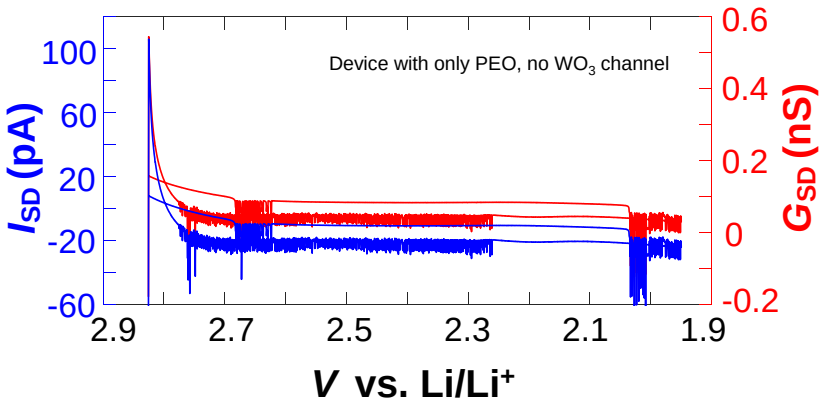

Figure 3.7. Control test without WO_3 channel and only PEO electrolyte. I_{SD} and G_{SD} response as a function of the gate sweeping voltage (V vs. Li/Li^+) when no WO_3 film is deposited as the channel and only PEO electrolyte is coated to cover the LFP reference electrode and channel area.

3.4 Low-Voltage and High-Precision Synapses

3.4.1 Dynamic Range and Precision

While LFP serves as a good reservoir of Li ions due to its stable electrochemical window, it is not an ideal control gate for a three-terminal artificial synapse because it would require a high programming voltage to overcome the electrochemical potential difference (ranging from ~0.45 V to 1.45 V)[190] between the channel (Li_xWO_3) and the gate (LFP). Hence we adopt a self-gate structure, where we use the same material (Li_xWO_3) for both the channel and the control gate and hence minimizing the potential difference[13] as well as achieving sub-1 V operations. We first lithiated both as-deposited WO_3 gate and WO_3 channel to the same lithiation levels ($Li_{0.4}WO_3$) through applying a constant voltage bias V_{LixWO3} = -1.1 V on both the gate and channel while grounding the LFP reference,[13] allowing us to achieve a near-zero OCV (< 0.1 V) between the

gate and the channel as well as a cubic WO_3 crystal structure for obtaining a more linear conductance response via pulse modulation. We envision that only one global LFP gate is needed as the ionic reservoir for a self-gated synaptic array, where pre-charge operations (to charge the self-gate to the desired electrochemical level) are sparingly performed. This will enable low-voltage programming as well as both short- and long-term plasticity while keeping the fabrication and circuity design complexity at a manageable level.

Combining this with the high-precision nature of our synapse originating from the large dynamic range as well as the good tunability enabled by the electrochemical intercalation, we demonstrate both potentiation and depression functions in **Figure 3.8** with low programming voltages (0.5 V) and good precision (1024 distinct states). Electrical characterization and pulse measurement were performed with Keithley Semiconductor Parameter Analyzer (4200-SCS) with pulse measuring units. During the test, the sample was transferred into the vacuum probe station (JANIS ST-500-UHT) and annealed at 350 K for ~2 hours to eliminate the residual moisture before the electrical measurements. We applied 512/1024 potentiation pulses (0.5 V, 10 ms) and 512/1024 depression pulses (-0.5 V, 10 ms) at $Li_{0.4}WO_3$ self-gate, where we observed a relatively linear and symmetric weight updates. We note a trade-off between the dynamic range and linearity/symmetry, where the linearity and symmetry of conductance response are slightly reduced when larger number of pulses are used to push the synapse to a larger dynamic range, likely associated with the saturation of accumulated electric charges at the interface between Li_xWO_3 channel/electrolyte and the asymmetry of electric charges accumulation (potentiation) and release (depression) processes under different directions of electric fields.

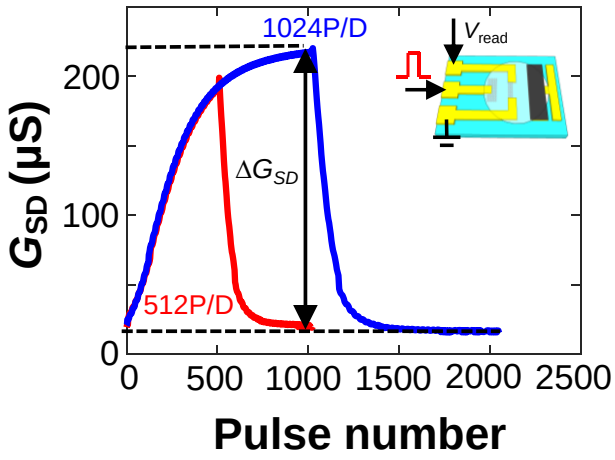

Figure 3.8. Dynamic range and precision of our low-voltage LiWES. Different dynamic ranges and precisions are able to be achieved by using different numbers of programming potentiation pulses (0.5 V, 10 ms) and depression pulses (-0.5 V, 10 ms) at $Li_{0.4}WO_3$ self-gate side (the inset).

3.4.2 Tunable Synaptic Weight via Varying Programming Pulses

In biological synapses, the amount of weight change (represented by the change in channel conductance ΔG_{SD} in our device) often varies for different neuronal signals.[204] We can mimic this behavior in our synapse to achieve different ΔG_{SD} by varying the amplitude, width and numbers of the programming pulse(s) at self-gate $Li_{0.4}WO_3$, as illustrated in **Figure 3.9**. We observed pseudo-linear relationships between ΔG_{SD} with respect to the pulse amplitude (from 0.1 V to 2 V, Figure 3.9a) and width (from 10 ms to 500 ms, Figure 3.9b), respectively. This is likely because the ΔG_{SD} is dependent on the amount of Li ions being transferred into the Li_xWO_3 film during the programming pulse. We observe a similar pseudo-linear relationship between ΔG_{SD} and the pulse number up to 800 pulses, after which ΔG_{SD} starts to become saturated. This saturation behavior is likely due to the limited amount of Li ions that can be transferred into the channel at a given

electrochemical potential between the channel and the gate, which is dictated by the pulse amplitude (i.e., 0.5 V in Figure 3.9c) and the lithiation concentration in the channel).

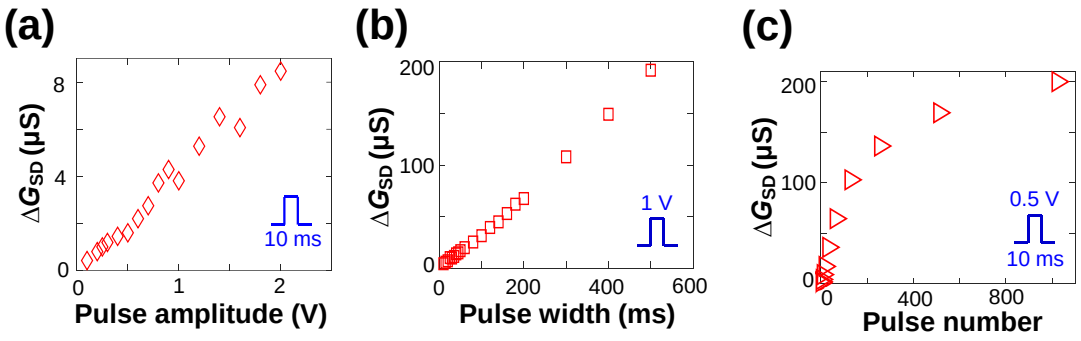

Figure 3.9. Tunable synaptic weight of LiWES via varying programming pulses. a) Synaptic weight change as a function of pulse amplitude. b) Synaptic weight change as a function of pulse width. c) Synaptic weight change as a function of pulse number.

3.4.3 Endurance and Retention Performance

To study the endurance behavior of our synapse, we cycled our synapse over 2000 pulses (20 cycles of 50 potentiation (0.5 V, 10 ms) and 50 depression (-0.5 V, 10 ms) pulses, as shown in **Figure 3.10a**), where we observed reversible and repeatable conductance change with a 500% dynamic range. We also performed long-time endurance LiWES using 1000 cycles of 50 potentiation (0.5 V, 10 ms) and 50 depression (-0.5 V, 10 ms) pulses with a dynamic range ~ 500 % (Figure 3.10b), where the synapse showed no sign of degradation after 10^5 pulses. We carried out thermal stability test for two different states: pristine WO_3 (before lithiation) and $Li_{0.4}WO_3$ (initial conductance state for self-gate and channel after lithiation), where we observed minimal resistance drift over 11 hours at 80 °C for both states **(**Figure 3.10c**)**.

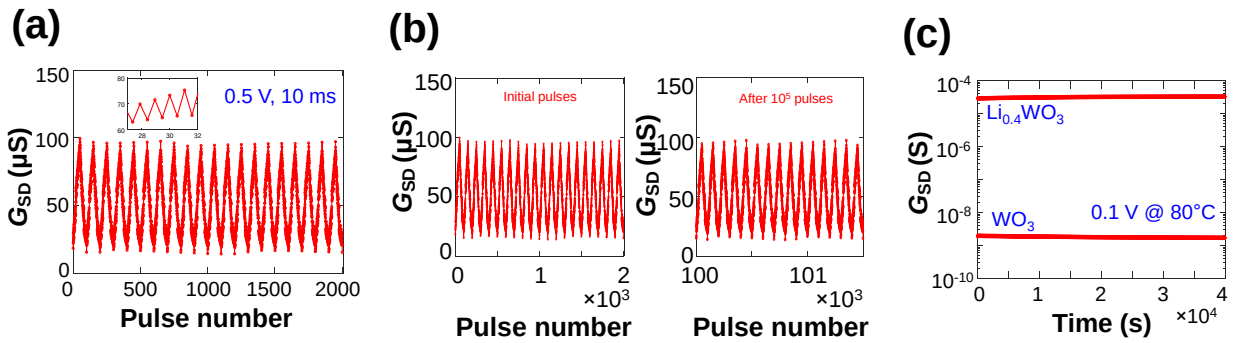

Figure 3.10. Endurance and retention test of our LiWES. a) Endurance test using 20 cycles of 50 potentiation pulses (0.5 V, 10 ms) and 50 depression pulses (-0.5 V, 10 ms) at $Li_{0.4}WO_3$ self-gate side. b) Endurance test for 10^5 pulses on our LiWES using 1000 cycles of 50 potentiation (0.5 V, 10 ms) and 50 depression (-0.5 V, 10 ms). No degradation of the device is found even after the 10^5 pulses. c) Stability test for two different states: pristine WO_3, $Li_{0.4}WO_3$ (initial conductance state for self-gate and channel), using reading voltage of 0.1 V at 80 °C.

3.4.4 Variations

Variations, including cycle-to-cycle (pulse-to-pulse) variation and device-to-device variation, are very important parameters to evaluate the synaptic device performance.[195] Small variations of the synaptic devices can contribute to less noisy and more accurate neural networks training and inference performance.[205, 206] We leveraged the data from Figure 3.10a and statistically analyzed the conductance change ΔG_{SD} per pulse over the whole dynamic range window. As shown in **Figure 3.11a**, we find a relatively small variation ~11% of ΔG_{SD} per pulse for potentiation pulses (red) and ~13% for depression pulses (blue). For device-to-device variation (Figure 3.11b), we fabricated four different devices of the same dimensions (400 × 200 μm^2) in one single batch and applied a single potentiation pulse (0.5 V, 10 ms) to the Li_xWO_3 gate while monitoring the channel conductance change using a small reading voltage (0.1 V) between Li_xWO_3

Source/Drain. We find a small variation of 6.5 %, which demonstrates the good repeatability of our devices.

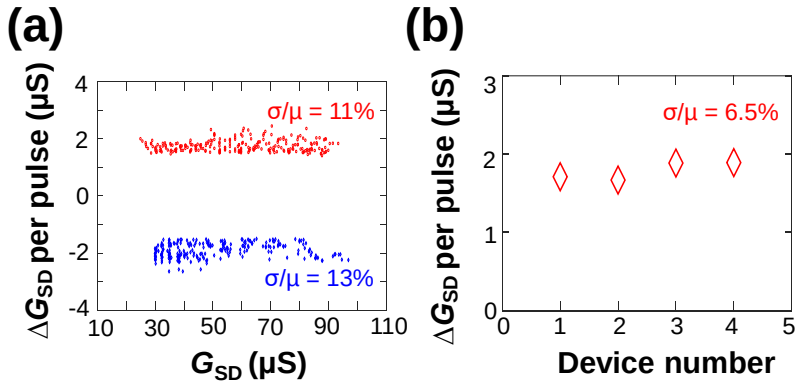

Figure 3.11. Variations of our LiWES. a) Cycle-to-cycle (pulse-to-pulse) variation, plotted using data from Figure 3.10a. Small variation ~11% of ΔG_{SD} per pulse is found for potentiation pulses (red) and ~13% variation of ΔG_{SD} per pulse is found for depression pulses (blue). b) Small device-to-device variation ~6.5% of ΔG_{SD} per pulse using single potentiation pulse (0.5 V, 10 ms).

3.5 Temporal Dynamics

3.5.1 Switching Mechanisms of Short-Term and Long-Term Plasticity

For SNNs, a dynamic synapse with both long-term and short-term plasticity (LTP and STP) is essential for learning applications.[7, 8, 207] However, it has been difficult to implement such temporal dynamics with traditional CMOS devices.[208] Our LiWES naturally possesses both LTP and STP, owing to a combination of the volatile ionic gating (**Figure 3.12a**) and the non-volatile charge transfer doping (Figure 3.12b) effects. Non-volatile charge transfer doping effect results in LTP as intercalated Li ions could stay at vacant A-sites in pseudo-perovskite tungsten oxide for

a long time via the electrochemical reaction as $Li_{0.4}WO_3 + xLi^+ + xe^- \leftrightarrow Li_{0.4+x}WO_3$, while volatile ionic gating effect results in electrical double layer formation. The ionic gating effect is short term because the accumulated electric charges (Li^+ ions in the PEO electroyte) at the interface between Li_xWO_3 channel and electrolyte would quickly diffuse back to the electrolyte when the external applied electric field (gate voltage) is removed.

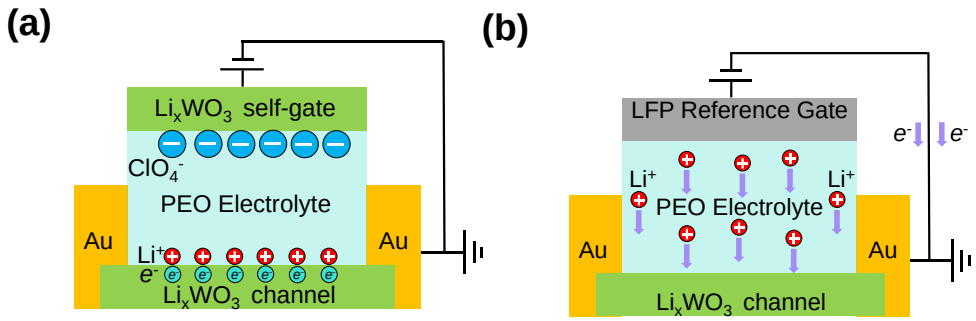

Figure 3.12. Shor-term and long-term plasticity of our LiWES. a) Ionic gating effect for STP. b) Charge transfer doping effect for LTP, where the electrochemical reaction occurs as $Li_{0.4}WO_3 + xLi^+ + xe^- \leftrightarrow Li_{0.4+x}WO_3$.

3.5.2 Short-Term to Long-Term Plasticity Transition

We are able to achieve the transition of STP to LTP by switching from a Li_xWO_3 self-gate to a LFP reference gate. As shown in **Figure 3.13a**, the Li_xWO_3 self-gate is used to apply voltage pulses which enables a low programming voltage (~ 0.2 V) owing to the near-zero OCV between Li_xWO_3 self-gate and channel. We observed a spike in channel conductance after the programming pulse due to ionic gating effects. As the volatile ionic gating effect dissipates after the voltage pulse, the channel conductance returns towards its original value. In this case, we observed no obvious charge transfer doping effect (LTP) likely because the electrochemical reaction driving force (electrochemical potential differences between gate and channel) for LTP is weak since there is a near-zero OCV between Li_xWO_3 self-gate and channel. By switching from the self-gate to a

LFP gate (Figure 3.13b), we observed a spike in channel conductance likely due to combined ionic gating [ΔG_{ST} (t)] and charge transfer doping effects [ΔG_{LT}]. Since the electrochemical OCV between LFP gate and Li_xWO_3 channel is ~ 1.1 V, there is enough electrochemical reaction driving force for charge transfer doping effect and thus the resulting time-dependent channel conductance consists of a long-term component [ΔG_{LT}] and a time-dependent, short-term component [ΔG_{ST} (t)] such that ΔG_{SD} (t) = ΔG_{LT} + ΔG_{ST} (t).

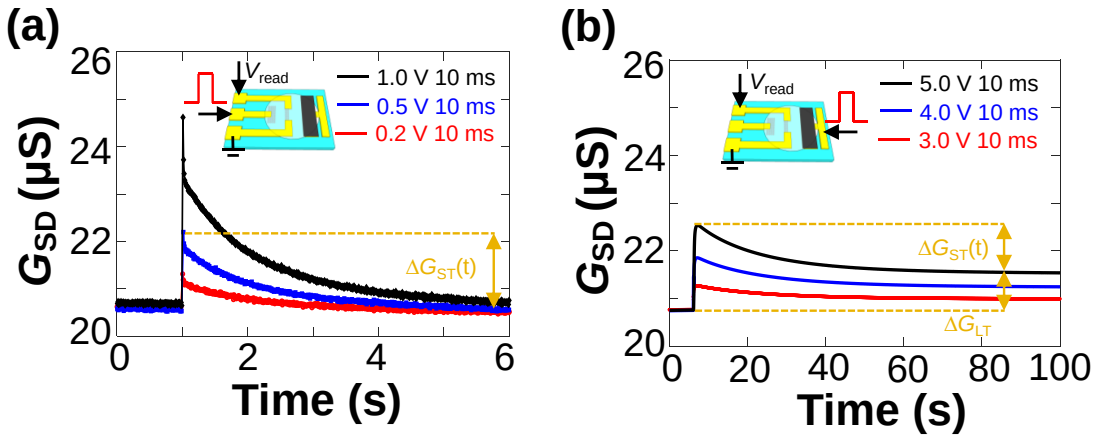

Figure 3.13. Transition from short-term to long-term plasticity via swithing gate. a) STP using $Li_{0.4}WO_3$ gate and $Li_{0.4}WO_3$ channel, controlled by different amplitudes of single pulse at $Li_{0.4}WO_3$ gate side. The inset shows the test setup. b) LTP using LFP gate and $Li_{0.4}WO_3$ channel, controlled by different amplitudes of single pulse at LFP gate. The inset shows the test setup.

3.5.3 Long-Term Potentiation and Depression

We further explored the long-term potentiation and depression by switching to use the LFP gate. For synaptic weight modulation via multiple pulses, we applied 50 potentiation pulses (3 V, 10 ms) and 50 depression pulses (- 1 V, 10 ms) applied at LFP gate as shown in **Figure 3.14a**. A

dynamic range (~ 200 %) was achieved. During the test, a small DC reading voltage (0.1 V) was applied between the Source and Drain to continuously monitor the current/conductance level, while programming pulses were applied at LFP gate. Since the electrochemical OCV between LFP gate and $Li_{0.4}WO_3$ channel is ~ 1.1 V, we need to use potentiation pulses (3 V) and depression pulses (-1 V) at LFP gate to achieve a base voltage level (1 V) that can offset the OCV difference in order to obtain a more linear and symmetric conductance response.

For confirming the intermediate conductance level stability in Figure 3.14a, we applied 5 potentiation pulses (3 V, 10 ms) at LFP gate (Figure 3.14b) and then used a small DC reading voltage (0.1 V) at 80 °C to monitor the channel conductance and observed small gradual stability degradation that is likely due to the slow self-extraction of the pulse-injected Li ions under high temperature at 80 °C. We also studied the long-time stability of the device after applying 5 depression pulses (-1 V, 10 ms) (Figure 3.14c) and no obvious stability degradation was observed.

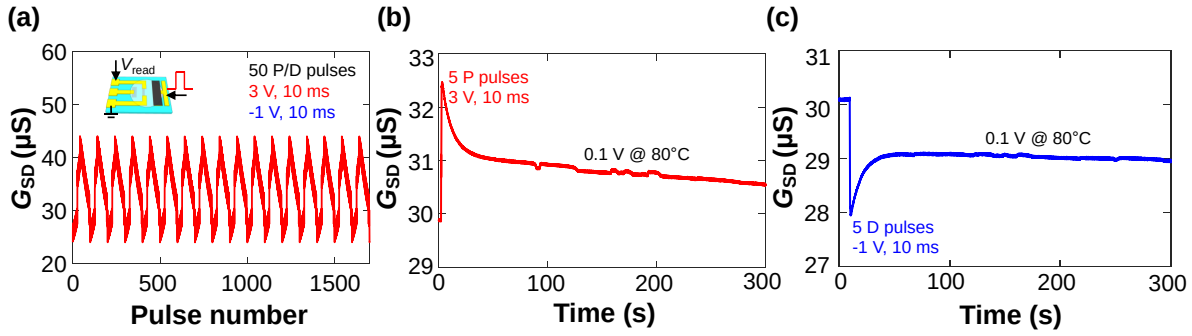

Figure 3.14. Long-term potentiation and depression via LFP gate. a) Synaptic weight modulation via multiple cycles of 50 potentiation pulses (3 V, 10 ms) and 50 depression pulses (- 1 V, 10 ms) applied at LFP gate. b) Long-time stability test of the LiWES device after 5 potentiation pulses (3 V, 10 ms) were applied. There is small gradual stability degradation, likely due to the slow self-extraction of the pulse-injected Li ions under high temperature at 80 °C. c) Long-time stability test of the LiWES device after 5 depression pulses (- 1 V, 10 ms) were applied. No obvious stability degradation was observed.

3.5.4 High-Speed Programming and Low Programming Energy

We also investigate how the pulse duration may affect the amount of weight change using Li_xWO_3 self-gate (**Figure 3.15a**). We still observe STP due to ionic gating with pulses as short as 500 ns, consistent with the time scale reported in the literature for ionic gating and electrical double layer formation.[209] The amount of STP decreases, as the pulse duration decreases, likely because smaller amount of electric charges accumulate at the interface between Li_xWO_3 channel/electrolyte and, thus, induce less electrons inside the Li_xWO_3 channel in shorter pulses. In addition, we are able to achieve consistent weight updates over 20 cycles of 50 potentiation (1 V, 1 μs) and 50 depression (- 1 V, 1 μs) pulses, with similar linearity and symmetry (Figure 3.15b) compared with long pulses (10 ms, Figure 3.10a).

We fabricated devices of different channel areas (from 1000 × 200 μm^2 to 200 × 50 μm^2) and applied single potentiation pulse at Li_xWO_3 gate while monitoring the channel conductance change. We define the programming energy as $E = I \times V \times$ t, which is enough to induce 10% increase of conductance change ($\Delta G_{SD}/ G_0$). Since there is near-zero OCV between our Li_xWO_3 gate and channel, V and t denote the programming voltage pulse amplitude and programming voltage pulse width, respectively, while we define the current I as the average current between our Li_xWO_3 gate and channel. As shown in Figure 3.15c, our smallest device (200 × 50 μm^2) demonstrates a very small programming energy (~ 2 pJ) and it shows a pseudo-linear scalability trend as previously reported.[210]

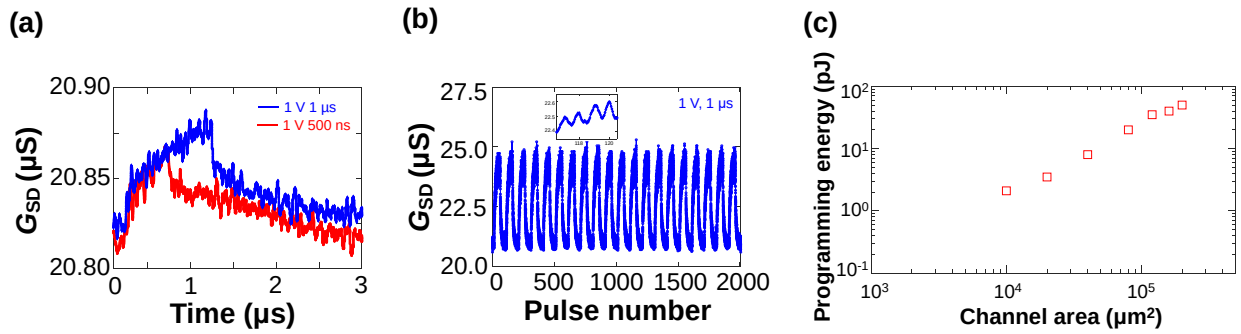

Figure 3.15. High-speed programming and scaling performance of programming energy. a) High-speed switching using different width of single pulse applied at $Li_{0.4}WO_3$ self-gate. b) Synaptic weight modulation via 20 cycles of 50 potentiation pulses (1 V, 1 μs) and 50 depression pulses (- 1 V, 1 μs) applied at $Li_{0.4}WO_3$ self-gate. c) Scaling performance of switching energy as a function of channel area.

3.5.5 Paired-Pulse Facilitation

In addition to LTP and STP, time-encoded spikes containing rich temporal information, which are responsible for learning and logical inference in biological neural network, are also desirable for SNNs applications. To better focus on studying temporal dynamics of our synapses, the benchmark of their performance in DNNs would be omitted here but we believe our LiWES synapses could potentially demonstrate decent DNNs performance because of their small energy consumption (~ 2 pJ) for a single pulse event (Figure 3.15c), fast programming speed, high precision and low variations. Leveraging the natural decay in our synapses, we demonstrate time-dependent synaptic functions such as PPF and temporal filtering in **Figure 3.16**, which have been difficult to implement with traditional CMOS devices. Tunable conductance change ΔG for a pair of pulses can be achieved by adjusting the time interval (Δt) between these two pulses at $Li_{0.4}WO_3$ self-gate (Figure 3.16a), mimicking the short-term, dynamic phenomenon in biological neural network where the amplitude of the second response is dependent on how closely the two pulses

are related.[176] In particular, the incremental effect ($G_2 - G_1$) in our synapse becomes less as the time interval becomes longer, as shown in Figure 3.16b. This resembles the biological learning behavior where the learning effect is better reinforced when two stimulations are more closely related. We also fit two characteristic timescales with a two-term exponential function: $\tau_1 = 19$ ms and $\tau_2 = 433$ ms, which are consistent with those found in biological synapse[176] and other previously reported artificial synapses.[12, 14] Those two characteristic timescales are likely related to the diffusion dynamics of Li ions[12, 14, 196] and can be engineered by changing the device dimension as demonstrated in prior studies.[7, 12]

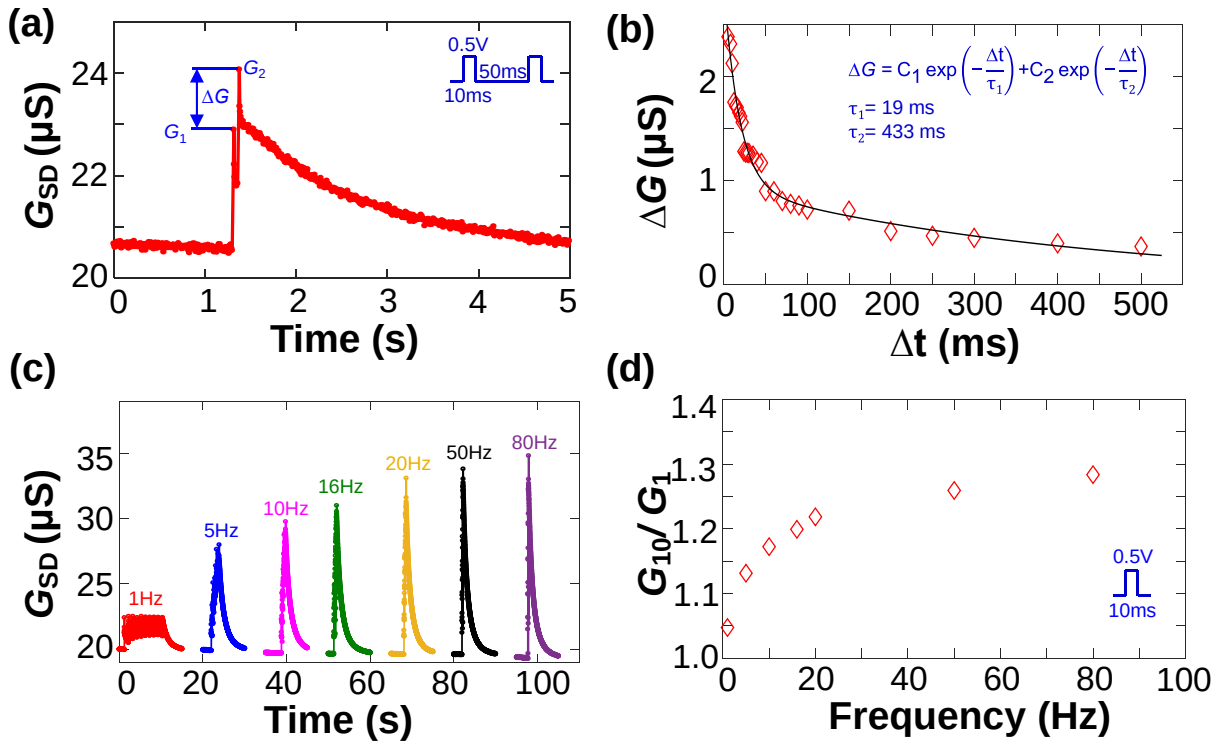

Figure 3.16. Bio-realistic, time-dependent synaptic functions for SNNs. a) Two consecutive pulses (0.5 V, 10 ms, Δt = 50 ms) showing paired-pulse facilitation. b) Paired-pulse facilitation with exponential decay fitting. c) High-pass temporal filtering characteristics of the our LiWES via applying 10 potentiation pulses (0.5 V, 10 ms) with different frequencies (1/Δt). d) The frequency-dependent conductance gain.

3.5.6 Temporal Filtering

STP can be used to generate filtering functions that are used in information processing, e.g. fish view the surrounding environment through the low-pass temporal filtering by which activated patterns of slow frequency (<10 Hz) are passed while repetitive patterns of fast frequency (> 10 Hz) are rejected.[211] The frequency-dependent high-pass temporal filtering can be mimicked by short-term facilitation (STF).[207, 212] By varying the signal frequency (i.e. time interval between pulses), we can modulate the maximum conductance level of our device, mimicking a high-pass temporal filtering. As we increase the frequency of a pulse train consisting of 10 consecutive pulses (0.5 V, 10 ms for each pulse) from 1 Hz to 80 Hz at $Li_{0.4}WO_3$ self-gate (Figure 3.16c), the maximum obtainable conductance level increases.[207] We also studied frequency-dependent gains of high-pass temporal filtering (Figure 3.16d), where the gain is defined as the ratio of the maximum conductance level of the tenth pulse (G_{10}) to the first pulse (G_1), demonstrating our LiWES can act as a high-pass temporal filter for information processing that is highly desirable for temporal computation in SNNs.

3.6 SNNs Computation Implementing Temporal Spiking Information

The goal of this section is to show how our LiWES devices' dynamic behaviors could be used to boost classification performance in highly time-dependent scenarios. The principle behind the proposed computation is that when the LiWES devices receive a set of spikes, their conductance value will change depending on the temporal structure (individual spike timings) of the input spike train (Figure 3.16). Furthermore, in absence of LTP when using Li_xWO_3 self-gate

and channel, the conductance of the device will be uniquely determined by the input spiking pattern and the time of integration,[213, 214] granting the device the ability to integrate temporal information and distinguish between different spike patterns.

In standard neuromorphic SNNs with NO-STP synapses, the synaptic efficacy (or weight), which remains fixed during inference, is used to simply scale current pulses directed towards the post-synaptic neuron. In these models, the temporal integration of stimuli is left solely to the neuron; whereas in STP enabled networks, synapses also encode temporal information through weight changes, enriching network dynamics[207, 215, 216] and increasing the ability of neurons to discriminate between temporal stimuli.[217] For this reason, when compared to NO-STP synapses, a network including the proposed LiWES device should increase its performance in highly time-dependent tasks, such as classification of different spike patterns. In order to test this hypothesis, we propose a test tailored to compare our LiWES to an IDEAL synapse (a noiseless LiWES device) and a standard NO-STP synapse. Here, we connect a post-synaptic neuron, modelled with Leaky Integrate and Fire profile (parametrized with the membrane decay constant τ_m and spiking threshold = ∞), to a pre-synaptic neuron, which is a Poisson Spike generator (**Figure 3.17a**). As shown in Figure 3.13a, the channel conductance response of our LiWES shows a spike profile, where the conductance quickly reaches the maximum conductance level followed by an exponential decay back to initial conductance level, due to ionic-gating governed STP effect. Thus, we are able to model the conductance response of our LiWES with a linear rise equation (gate-pulse applied) and a double exponential decay equation (gate-pulse removed). (See the next section for model build details). Every time the synapse receives a new spike at the time t_i, the parameter G_{off} gets updated to the last conductance value while a set of parameters are drawn to generate a response as the one shown in Figure 3.17b.

In the proposed task, we generate multiple pre-synaptic neuron spike trains with a fixed maximum duration. Since each spike sequence is randomly generated at a fixed frequency, therefore it differs from the others mainly by its temporal characteristics (the timestamps of individual spikes) and it represents a single class of a classification problem. The beginning of each spike train is delimited by t_{onset}. A "sequence end spike" is added at the end of each spike train at a specific time t_{end} (Figure 3.17c) and the post-synaptic neuron membrane potential is read out at t_{read} (Figure 3.17d), representing the output of the system. Each spike train is presented to the synapse multiple times to obtain multiple membrane potential read-outs for the same "class" (or spike pattern). To calculate the class separability of the read-outs, we define a distance metric as the difference between the Euclidean distance of points between different classes (inter-class distance) and the distance of the points within the same class (intra-class distance) in Figure 3.17e. Since the membrane potential of the post-synaptic neuron is always read out at the same time (t_{read}) after the last spike (t_{end}), a neuron unable to integrate temporal information will have similar membrane potential for different spike patterns and therefore it will have an average inter-class distance of zero or close to zero, However, for an STP enabled neuron, its membrane value depends on previous spiking activity, which gives different values of inter-class distance based on different classes. This is the case shown in Figure 3.17f, where a fast spiking neuron (τ_m = 10 ms) is stimulated with Poisson generated spikes at a slow mean 10 Hz frequency. The number of classes used for this simulation was 50, each one presented 10 times (for intra-class measurement), for a total number of 500 points. In this case, class separability (inter-class distance – intra-class distance) is ~3.8×10^{-4} for the NO-STP synapse, ~4.9×10^{-2} for our LiWES device (~128× higher relative to NO-STP synapse), and ~8.6×10^{-2} for the IDEAL synapse (~226× higher compared to NO-STP synapse), with using a synaptic weight *k* of 4.3 (See the next section for model build

details). As both comparison synapses (NO-STP and IDEAL synapses) are totally deterministic, their mean intra-class distance is 0. The same simulation parameters were used in Figure 3.17g for a much slower post-synaptic neuron (τ_m = 100 ms). Even though the post-synaptic neuron is relatively slower to integrate temporal information, a boost in class separation (~1.4× in our LiWES and ~1.7× in the IDEAL synapse, relative to the NO-STP synapse) can still be achieved owing to the natural stochastic STP in our LiWES. The class separability is ~8.4×10^{-2} , ~1.2×10^{-1} , ~1.4×10^{-1} , for the NO-STP synapse, our LiWES device, and the IDEAL synapse respectively, with using a synaptic weight *k* of 16.7. By implementing the temporal spiking information in STP of our LiWES, we improve the pattern classification performance (up to 128× comparted to NO-STP synapse) in highly time-dependent scenarios.

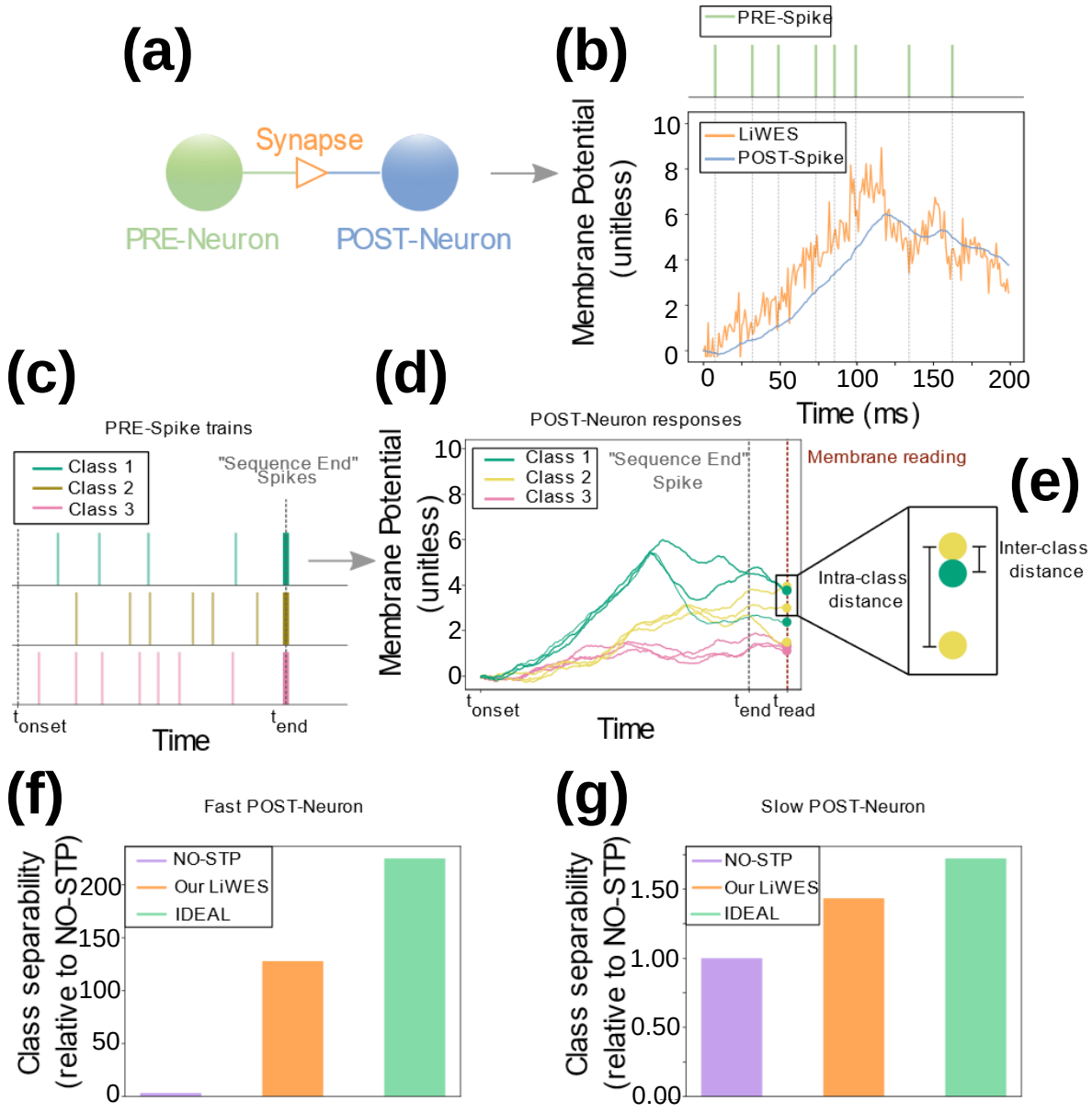

Figure 3.17. SNNs computation based STP of our LiWES. a) The diagram of our network, a Poisson pre-synaptic (PRE) neuron connected to a Leaky and Integrate and Fire post-synaptic (POST) neuron through a synapse (NO-STP, our LiWES or IDEAL synapse). b) An example of a Poisson train spike eliciting activity in our LiWES and the consequently generated membrane potential. c-e) An example of the proposed spike-based SNNs computation model for classification performance benchmark. c) The PRE-Neuron produces multiple random spike trains, at the end of each one we add a "sequence end" spike occurring always at the same timestamp(t_{end}). Each spike train represents a different class in a classification problem. d) We then record multiple POST-Neuron responses (three responses per each spike train), in order to better characterize the device noise and cycle-to-cycle variation,

and finally we save the membrane value after the "sequence end spike" (at t_{read}). e) Lastly, for each point we calculate the inter-class distance between points of different spike trains, and the intra-class distance between points of the same spike train class. These measures indicate how much each point position encodes for temporal information and how well the points are separable in a classification task. f,g) The classification result of the benchmarked synapses. f) The classification comparison for a 10 Hz Poisson PRE-Neuron and a fast POST-Neuron (τ_m= 10 ms). g) The classification comparison for the same 10 Hz Poisson PRE-Neuron but a much slower POST-Neuron (τ_m= 100 ms).

3.6.1 SNNs Computation Model

We model our LiWES device behavior using a linear rise (Equation 3.1) and a double decay exponential model (Equation 3.2), using Equation (3.3) to define the rise and decay parts, respectively.

$$G_{rise}(t) = \left(\widehat{A_1} + \widehat{A_2}\right)\frac{t-t_i}{w} + \eta + G_{off} \tag{3.1}$$

$$G_{decay}(t) = \left(\widehat{A_1} + \frac{G_{off}}{2}\right)e^{-\left(\frac{t-t_i}{\widehat{\tau_1}}\right)} + \left(\widehat{A_2} + \frac{G_{off}}{2}\right)e^{-\left(\frac{t-t_i}{\widehat{\tau_2}}\right)} + \eta \tag{3.2}$$

$$G(\mathrm{t}) = \begin{cases} G_{rise}(t)\ when\ (t-t_i) < w \\ G_{deacy}(t)\ when\ (t-t_i) \geq w \end{cases} \tag{3.3}$$

The model parameters ($\widehat{A_1}, \widehat{A_2}, \widehat{\tau_1}, \widehat{\tau_2}$) are drawn from Gaussian distributions fitted on experimental recordings obtained with a single pulse stimulus of a given amplitude and pulse width *w*. Additive Gaussian noise η with a mean of 0 is also added to simulate device and recording setup noise.

In order to obtain the Gaussian distributions of the LiWES parameters ($\widehat{A_1}, \widehat{A_2}, \widehat{\tau_1}, \widehat{\tau_2}$) and the standard deviation the additive noise, we fit the decay equation (Equation 3.2) on the device

response to a single pulse (1 V, 200 μs) for 20 consecutive trials. Every trial produces a set of parameters (A_1, A_2, τ_1, τ_2, η), which can be then averaged to produce the **Table 3.1**.

Table 3.1. SNN model parameters for a single pulse (1 V, 200 μs). Results of an averaged fit over 20 consecutive recordings. All parameters are presented with their mean ± standard deviation except for η, which is the mean standard deviation of each individual fit.

A_1	τ_1[ms]	A_2	τ_2 [ms]	η
0.57± 0.27	5 ± 2	0.5 ± 0.05	92 ± 18	0.11

When simulating the noise-free, IDEAL synapse, we use the same parameters presented above but set all standard deviations and additive Gaussian noise η to 0. Finally, the NO-STP synapse is modelled as a weighted Dirac pulse centered on the input spike timestamp t_i (Equation 3.4):

$$G(t) = \sum_{t_i} k\delta(t - t_i) \tag{3.4}$$

where *k* is the synaptic weight chosen so that the peak response of the post-synaptic neuron to a single spike is the same to the IDEAL synapse.

3.7 Conclusion

In summary, we develop a WO_3-based, electrochemical synapse with low programming voltage (0.2 V), fast programming speed (500 ns), high precision (1024 levels), low variations, as well as a relatively linear and symmetric response. In addition, our dynamic synapse naturally exhibits both LTP and STP behaviors owing to the combined effects from charge transfer doping

and ionic gating, which is desirable for SNNs applications. We demonstrate various time-dependent synaptic functions such as pair-pulse facilitation and temporal filtering. By leveraging the spike-encoded timing information extracted from the short-term plasticity exponential decay behavior, we build a SNNs model to benchmark the pattern classification performance of our LiWES, which shows a large boost (128× improvement) in classification performance in highly time-dependent scenarios.

4.0 Towards Real-Time BP Monitoring via Iontronic Tonometric Sensors (ITS)

4.1 Motivation

Continuous, non-invasive blood pressure monitoring provides valuable hemodynamic information that renders detection of the early onset of cardiovascular diseases. Wearable mechano-electric pressure sensors that mount on the skin have been great candidates for monitoring continuous BP pulse waveforms due to their excellent conformability, simple sensing mechanisms, and convenient signal acquisition. However, it is challenging to acquire high-fidelity BP pulse waveforms since it requires highly sensitive sensors that respond linearly with pressure change over a large dynamic range. Here, we introduce a high-fidelity iontronic tonometric sensor (ITS) with high sensitivity (4.82 kPa^{-1}), high linearity ($R^2 > 0.995$) and a large dynamic range (up to 180 % output change) over a broad working range (0-38 kPa) that can fully cover the normal BP range (5-25 kPa). Additionally, our ITS demonstrates a low limit of detection at 40 Pa, a fast load response time (35 ms) and release time (35 ms), and a stable response over 5000 load/release cycles. We further explore the application of our ITS in monitoring real-time beat-to-beat BP by measuring the brachial and radial pulse waveforms. Our work provides a feasible design for a wearable pressure sensor with high sensitivity, high linearity and a large dynamic range for real-time CNIBP monitoring.

4.2 Experimental Section

4.2.1 Preparation of Micropyramid Electrodes

First, 1000 nm thermally-grown SiO_2/Si (100) substrates (1.5 × 1.5 cm^2) were patterned via photolithography. A buffered oxide etch (BOE) (7:1) was then applied to form a SiO_2 hard mask used for potassium hydroxide (KOH) etching in subsequent steps. KOH etching is a well-developed anisotropic Si etch process that can be used to form the V-shaped pyramid depth. A mixing solution (47% KOH: isopropyl alcohol (IPA) = 4:1, v/v) was used at 80 °C under vigorous stirring for KOH etch, where IPA was used to facilitate the anisotropy of the V-shaped depth. The KOH etch rate was ~ 1 µm min^{-1}. Si Molds of two different depths were fabricated: 11 µm and 30 µm. The as-fabricated Si molds were then cleaned with acetone, methanol, and IPA in an ultrasonic bath, followed by a N_2 gun blow dry and O_2 plasma clean for 5 mins. The Si molds were silanized with (TRIDECAFLUORO-1,1,2,2-TETRAHYDROOCTYL)TRICHLOROSILANE (Gelest) to facilitate the subsequent release of the drop-casted PDMS film from the Si molds. A 1:10 mixture of curing agent and PDMS elastomer (Sylgard 184, Dow Corning) was prepared and stirred for 10 mins. The solution was then drop-casted onto the Si molds, followed by degassing in a desiccator for at least 1 h until no bubbles were observed. The sample was transferred into the oven and baked at 90 °C for 4 hours to cure the PDMS elastomer. After the cool-down of the sample, the PDMS elastomer film was peeled-off from the Si molds and coated with 70 nm Au via electron beam evaporation in a cleanroom to form the MP-PDMS electrode. We chose to use Au as the conducting layer on the micropyramid PDMS elastomer because of its great ductility and flexibility.

4.2.2 Preparation of IG Film

A polar polymeric matrix Poly(vinylidene fluoride-*co*-hexafluoropropylene) (PVDF-HFP) (Sigma aldrich) and an ionic liquid 1-Ethyl-3-methylimidazolium bis(trifluoromethylsulfonyl)imide ([EMIM] [TFSI]) (Sigma aldrich) was mixed in a weight ratio of 1:4 (ionic liquid : polymer) and then dissolved in acetone solvent in an Ar-filled glovebox. The ionic gel solution was vigorously stirred at 75 °C for 30 mins and then drop-casted onto a clean Si/SiO_2 substrate (~ 400 µL). The substrate coated with the ionic gel solution was annealed at 75 °C overnight to evaporate all the solvent. The prepared ionic gel films were then cut and transferred to the purchased ITO/PET films (Fisher Scientific).

4.2.3 Assembly of the ITS devices

A conductive copper electrode was attached to the prepared MP-PDMS electrode of 1.5 × 1.5 cm^2 using silver conductive epoxy (Ted Pella, Inc). An ITO/PET electrode was tailored to an area of 1.5 × 4 cm^2 to allow for some space for wire contact during the electrical measurement. The ionic gel film was sandwiched by the MP-PDMS electrode and ITO/PET electrode, and then the device was encapsulated using polyimide thin film (Fisher Scientific) and polyimide tape (Fisher Scientific).

4.2.4 Measurement and Characterization

The capacitance of the ITS sensors was measured using a capacitance-voltage unit (CVU) module of a Keithley semiconductor parameter analyzer 4200-SCS under ambient conditions. The

C-f test for characterization of UAC of the ITS was performed by sweeping the AC voltage frequency from 1 to 10 kHz at a fixed DC voltage of 0.5 V. For piezocapacitance measurements of the ITS, an automated test stand (Mark 10, ESM 303) with a digital force gauge (M5-2, 2 lbf) was controlled using a customized LABVIEW program to apply external compressive pressure to the ITS device, while a two-probe *C-t* sampling test (sampling frequency 30 Hz) was conducted to measure the real-time capacitance of the ITS using a fixed AC voltage frequency of 1 kHz and 0.5 V DC voltage. For arterial BP monitoring, instead of using a force gauge, an aneroid sphygmomanometer kit (Dixie EMS on Amazon) was used to apply applanation pressure while a *C-t* sampling test (sampling frequency 30 Hz) was conducted using alligator clips attached to the contact electrodes of the ITS. All experiments related to the human body complied with the necessary medical standards with consents from the tested person. The thickness measurement of the MP-PDMS electrode and IG film was performed using a surface profiler (Bruker DektakXT). The SEM images were taken using a 3 kV accelerating voltage via Zeiss SIGMA VP SEM.

4.3 Design and Fabrication of the ITS

Figure 4.1a demonstrates the fabrication flow of our ITS. First, silicon molds were fabricated via photolithography patterning and wet etch in a cleanroom. They were then silanized to facilitate the peel-off of the cured dielectric elastic elastomer polydimethylsiloxane (PDMS) films from the molds in the following steps. Second, the peeled-off PDMS film on each was coated with 70 nm Au to form the MP-PDMS electrode. The patterns of MP-PDMS electrode duplicate the etched V-shape holes in silicon molds. An ionic gel (IG) film, consisting of a polar polymeric matrix Poly(vinylidene fluoride-co-hexafluoropropylene) (PVDF-HFP) and an ionic liquid 1-

Ethyl-3-methylimidazolium bis(trifluoromethylsulfonyl)imide ([EMIM] [TFSI]), was prepared and transferred via the cut-stick method[23] onto the purchased indium tin oxide coated Polyethylene terephthalate film (ITO/PET) electrode. Lastly, the MP-PDMS electrode, IG film and ITO/PET electrode were all laminated together via encapsulation using polyimide films. A conductive copper electrode was then attached to the MP-PDMS electrode via conductive silver paste.

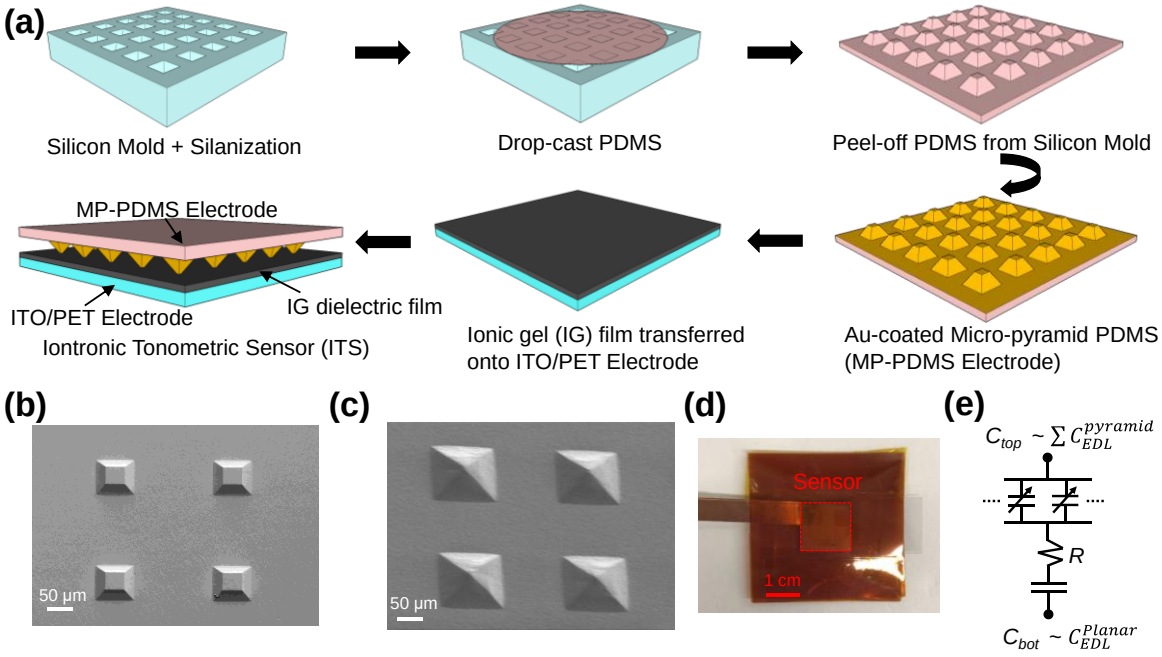

Figure 4.1. The fabrication process and structure of the ITS. a) Schematic illustration of the fabrication process of the ITS. b) 25°-tilt SEM image of 11 μm-height Au-coated (70 nm) MP-PDMS electrode. c) 25°-tilt SEM image of 30 μm-height Au-coated MP-PDMS electrode. d) Optical image of the encapsulated ITS with effective sensing area of 1.5 cm × 1.5 cm. e) Equivalent circuit diagram of the ITS.

We combine the micropyramid electrode with the iontronic interface in our ITS design to achieve high-fidelity, linear and highly sensitive piezocapacitive sensor performance. Our ITS relies on the deformation of an elastic elastomer micropyramid PDMS (MP-PDMS) electrode to transduce the input pressure change into the output capacitance change. Micropyramid structural engineering was first reported by Prof. Bao's group at Stanford, and it was proven to be an effective

way of improving a material's compressibility and thus is useful for enhancing the sensitivity of the traditional piezocapacitive sensor.[21] Iontronic sensing, or interfacial supercapacitive sensing, was first introduced by Prof. Pan's group at UC Davis to achieve high-fidelity capacitance outputs, improved detection resolution and device sensitivity.[17] We will elaborate on the iontronic supercapacitive effects in the next section.

Although there have been studies reporting on creation of microengineered iontronic sensors,[148, 157] the reported sensors demonstrated gradually saturated sensitivity and less than ideal linearity in normal BP range (< 25 kPa). This is likely because they used an ionic gel film as an elastic material. Ionic gel film has a relatively small Young's modulus (~ 1.3 MPa)[23] and thus reaches structural stiffness early in a small pressure region. We utilized a PDMS film as a pressure-sensitive elastic material because of its suitable Young's modulus (~ 3 Mpa)[141] and great compatibility with human skin.[21] Use of this film enabled our ITS to demonstrate a broad working range with decent sensitivity. A unique characteristic of iontronic sensing is that it relies on the interfacial contact area change (ΔA), rather than the physical vertical distance change (ΔD) between two electrodes in traditional two-plate piezocapacitive sensor, to modulate the capacitance output. The usage of MP-PDMS electrodes interfaced with IG film in our ITS design provided us with an effective way of controlling the initial interfacial contact area (A_0). Sensitivity, defined as the minimum input parameter that generates a detectable output change, is one of the most important parameters used to evaluate the accuracy and resolution of a sensor. The sensitivity of a piezocapacitive sensor can be expressed as in Equation 4.1:

$$S = \frac{\partial\left(\frac{\Delta C}{C_0}\right)}{\partial P} \tag{4.1}$$

where C_0 denotes the initial capacitance, $\Delta C = C - C_0$ denotes the capacitance change and P denotes the external pressure. In iontronic sensors, the relationship between EDL capacitance C_{EDL} and interfacial contact area A is defined[145] asin Equation 4.2:

$$C_{EDL} = \text{UAC} \bullet A \tag{4.2}$$

Thus, controlling the A_0 allows for an effective tuning of the initial capacitance C_0 and the sensitivity. Figure 4.1b and 4.1c indicate the SEM images of two different height designs for MP-PDMS electrodes, 11 µm and 30 µm respectively. The top-view and cross-sectional SEM images of the silicon molds are shown in **Figure 4.2**, where two different patterns are achieved, 11 µm and 30 µm depth. The 25°-tilt SEM images of an array of MP-PDMS electrodes are indicated in **Figure 4.3**, confirming the successful pattern duplication of MP-PDMS electrodes from the silicon mold. We expect a smaller A_0 and a higher sensitivity in our 30 µm-ITS than in the 11 µm-ITS. Figure 4.1d is a photo of our prepared ITS with an effective sensor area of 1.5 × 1.5 cm^2. The thickness of the prepared MP-PDMS electrode and IG film are 1178 µm and 171 µm, respectively (**Figure 4.4**). A 130 nm ITO coated PET film (127 µm, purchase from Sigma Aldrich) was used as the bottom electrode. Two contact electrodes consisting of a copper electrode (yellow) and an ITO/PET electrode (transparent) were used for electrical capacitance measurements. Figure 4.1e shows an equivalent circuit diagram of the ITS, where C_{top} is a summation of EDL capacitance for an individual micropyramid/IG film capacitor and C_{bot} is the EDL capacitance for a planar ITO/IG capacitor. Since the total A between the arrays of micropyramid electrodes and IG film is much smaller than that between the bottom planar ITO/PET electrode and IG film, i.e., $\sum C_{EDL}^{pyramid} \ll C_{EDL}^{Planar}$, the measured capacitance between top and bottom electrode can be expressed in Equation 4.3:

$$C_{meas} = \left[\frac{1}{C_{top}} + \frac{1}{C_{bot}}\right]^{-1} = \left[\frac{1}{\sum C_{EDL}^{pyramid}} + \frac{1}{C_{EDL}^{Planar}}\right]^{-1} \cong \sum C_{EDL}^{pyramid} \quad (4.3)$$

Under external pressure, the deformation of MP-PDMS induces a change in the $\sum C_{EDL}^{pyramid}$. In a nutshell, our design provides a reproductive way of achieving high-fidelity, large-dynamic-range wearable sensors with tunable sensitivity.

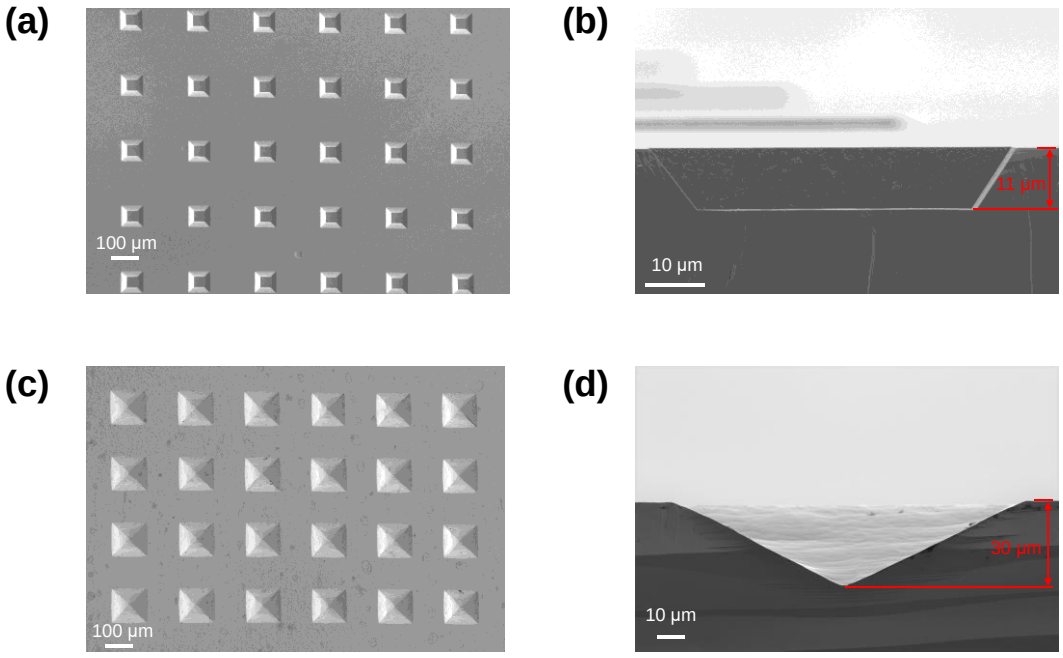

Figure 4.2. The SEM images of as-fabricated silicon mold of two different patterns. a) The top-view SEM image of a 11 μm-depth silicon mold. b) The cross-sectional SEM image of one single micro-pyramid with etched depth of 11 μm. c) The top-view SEM image of a 30 μm-depth silicon mold. d) The cross-sectional SEM image of one single micro-pyramid with etched depth of 30 μm.

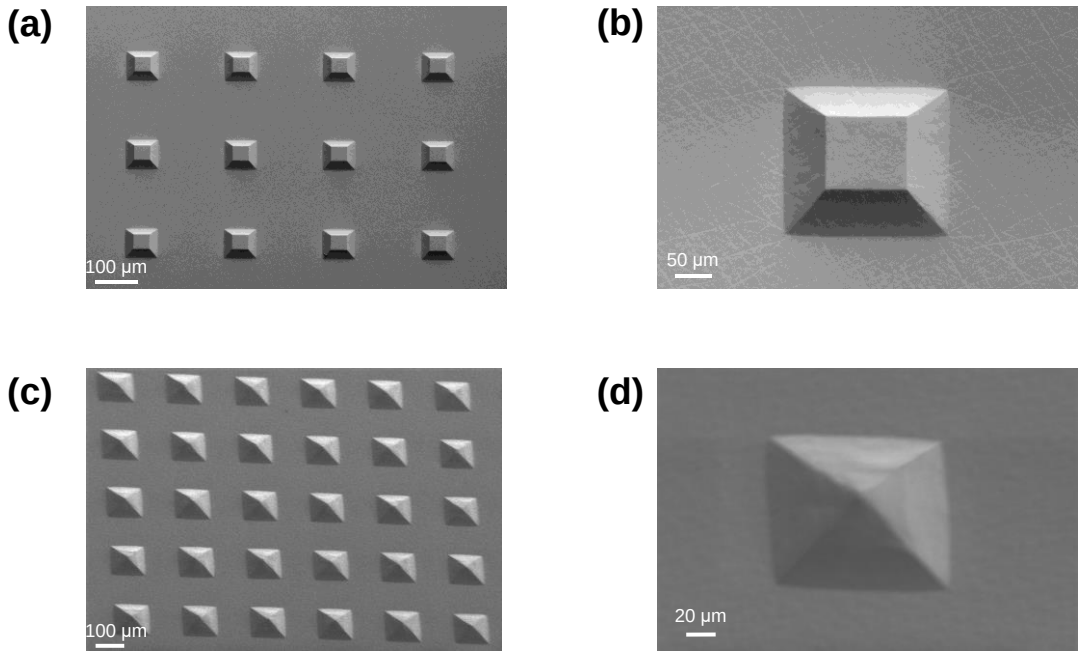

Figure 4.3. SEM images of MP-PDMS electrodes of two different heights. a-b) 25°-tilt SEM image of 11 µm-height MP-PDMS. c-d) 25°-tilt SEM image of 30 µm-height MP-PDMS.

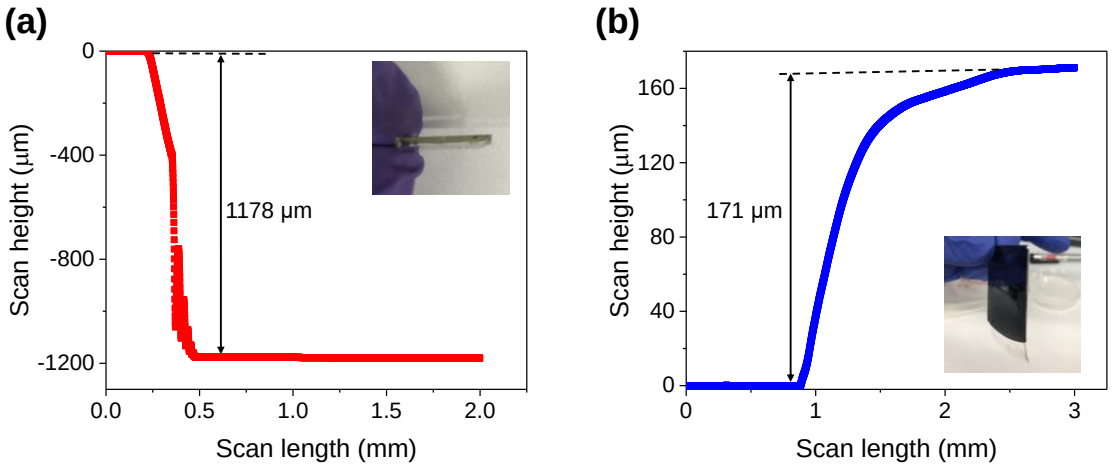

Figure 4.4. The measured thickness of the MP-PDMS electrode and IG film. a) The measured thickness of the MP-PDMS electrode is 1178 µm. b) The measured thickness of the IG film is 171 µm.

4.4 Iontronic Supercapacitive Effects

Iontronics is an emerging interdisciplinary field that studies the electronic properties controlled by the ionic motion at an ionic conductor/electronic conductor interface.[1, 3] An intriguing characteristic in iontronics is the EDL at the interface, where an accumulation of space charges is prompted by ionic motion at the interface under an external applied electric field, also known as a Helmholtz layer, with a thickness of ~ 1 nm determined by the shortest distance of the nearest ionic molecules in the ionic electrolyte.[218] At the iontronic interface, the EDL can work as a nanogap supercapacitor with an ultrahigh UAC, which value can be experimentally determined. **Figure 4.5a** indicates the schematics of the proposed working mechanism of our ITS under external mechanical compressive pressure at a fixed applied DC voltage. Increasing the external pressure induces the deformation of the MP-PDMS, accompanied by a larger interfacial contact area *A* between the MP-PDMS and the IG film, which increases the amount of accumulated charge pairs and the $\sum C_{EDL}^{pyramid}$. Thus, the resulting measured capacitance output C_{meas} is expected to increase with larger applied pressure. We fabricated a flat PET/ITO/IG film (weight ratio of PVDF-HFP : [EMIM] [TFSI] : Acetone = 1:4:7) /ITO/PET iontronic device to experimentally determine the UAC value of the EDL capacitance. A fixed DC voltage of 0.5 V was applied between two electrodes and the capacitance was measured as the test AC voltage frequency was swept from 1 kHz to 10 kHz. Figure 4.5b shows an ultrahigh UAC of 2.1 μF cm-^{2} at 1 kHz AC voltage, which is 1000 times higher than that of traditional piezocapacitive sensors (several pF cm-^{2}).[141] This further confirms the high-fidelity of our designed ITS. Figure 4.5c indicates the initial capacitance C_0 of two height designs of ITS: 11 μm and 30 μm MP-PDMS. Owing to the introduction of micropyramid structures, the C_0 at 1 kHz AC voltage can be scaled down to 670

nF in 11 µm-ITS and 13 nF in 30 µm-ITS, which agrees well with our design prediction in the previous section. Also, according to Equation 4.2 and 4.3, we could deduce a predicted maximum dynamic range for our 11 µm-ITS (670 nF to 2360 nF) and 30 µm-ITS (13 nF to 2360 nF) at a fixed 0.5 V DC voltage and 1 kHz test frequency using an effective sensor area of 1.5 × 1.5 cm^2 in Equation 4.4, based on the assumption that the top electrode and bottom electrode will completely interface with each other under an extremely high compressive pressure, i.e., C_{top} = C_{bot} = C_{EDL}^{Planar}:

$$C_{max} = \left[\frac{1}{C_{top}} + \frac{1}{C_{bot}}\right]^{-1} \cong \left[\frac{2}{C_{EDL}^{Planar}}\right]^{-1} = \left[\frac{2}{\text{UAC} \times A_{bot}^{Planar}}\right]^{-1} = 2360\ nF \qquad (4.4)$$

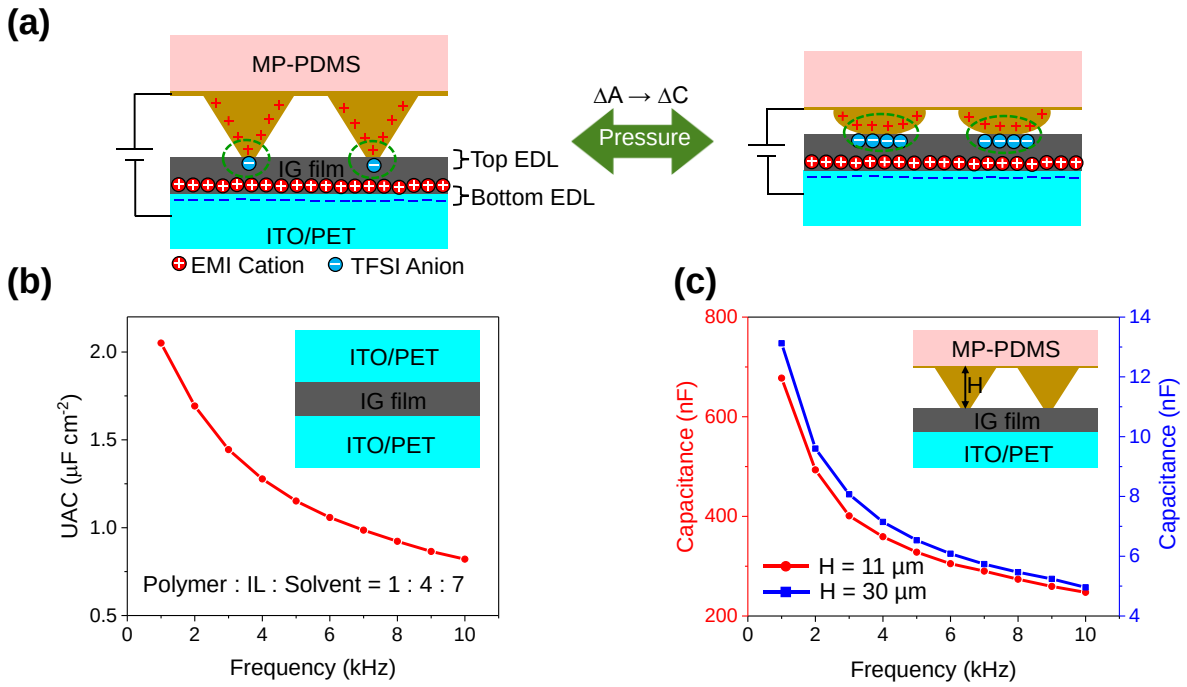

Figure 4.5. Supercapacitive effects in the ITS. a) Supercapacitive effects governed by the electric-double layer, which allows ions to self-fill the interfacial contact area between the Au-coated MP-PDMS electrode and IG film. b) UAC-voltage frequency response at V_{DC} = 0.5 V for a flat PET/ITO/IG/ITO/PET device. c) Capacitance-voltage frequency response at V_{DC} = 0.5 V for the ITS with two different pyramid heights, 11 µm and 30 µm.

Overall, our ITS demonstrates a high-fidelity capacitance output benefiting from the simple iontronic sensing design. We believe our ITS can more accurately capture the real-time, continuous BP signals because the high-fidelity output is immune to the transmission line and environmental electromagnetic noises which lie in the pF capacitance level.[145]

4.5 Sensing Performance

Sensor sensitivity, dynamic range, pressure working range, linear response between input pressure and output capacitance, hysteresis, response time and durability are important parameters for sensing performance evaluation. To confirm that our designs enables tunable sensitivity through its use of micropyramid engineering, we first investigated the dynamic range, sensitivity, and linearity of our ITS. **Figure 4.6a** shows the results of the dynamic range and sensitivity analysis for 3 different ITS devices: flat, 11 μm MP-PDMS, and 30 μm MP-PDMS. Figure 4.6b shows the zoom-in of the flat and 11 μm MP-PDMS ITS devices. External compressive pressure ranging from 0 to 38 kPa was applied by a digital force gauge mounted on an automated test stand (See Experimental Section for details on electrical characterization). The maximum force limit of our used digital force gauge is 2 lbf, i.e., 40 kPa for our ITS. To avoid damage to our force gauge, we chose a maximum pressure range from 0 to 38 kPa, but we believe our ITS could still respond in a high pressure region larger than 38 kPa. From the linear fitting analysis of our ITS devices, 30 μm MP-PDMS shows a large dynamic range, up to 180 % of the normalized output change, with a high sensitivity of 4.82 kPa^{-1} within the 0-38 kPa working range. A normalized capacitance output change was used to get a better benchmark across various types of sensors. The measured real-time capacitance output as a function of the applied pressure is shown in **Figure 4.7**. This

large dynamic range confirms the high-fidelity of our designed ITS, and this high sensitivity allows for a more accurate capture of the BP values. With the benefit of micropyramid engineering, the sensitivity can be boosted by ~ 30 × from 0.0016 kPa^{-1} (flat) to 0.05 kPa^{-1} (11 μm-ITS). Furthermore, increasing the pyramid heights from 11 μm to 30 μm resulted in sensitivity enhancement from 0.05 kPa^{-1} to 4.82 kPa^{-1} (~ 100 ×), largely owing to the smaller initial capacitance C_0 of the 30 μm-ITS. Figure 4.6c indicates a linear response between capacitance output and input pressure upon three repeatable pressure loading cycles for 30 μm-ITS. The correlation coefficient (R^2) of the curve linear fitting is as high as 0.99, demonstrating good linearity between input pressure and output capacitance change. This good linearity results from the unique interfacial contact area A dependent sensing mechanism of the iontronic interface, where the structural stiffening of the elastic elastomer PDMS can be gradually compensated for by incremental changes in the contact area. Other iontronic sensors also reported similarly good linearity.[147] We benchmarked the sensitivity and linearity of our ITS with other reported sensors[136, 138, 142, 144, 146, 148, 151, 154-157] in the BP normal range, from 5-25 kPa, in Figure 4.6d. Our work demonstrates a fairly high sensitivity with a good linearity, which is desired for CNIBP monitoring.[117, 119]

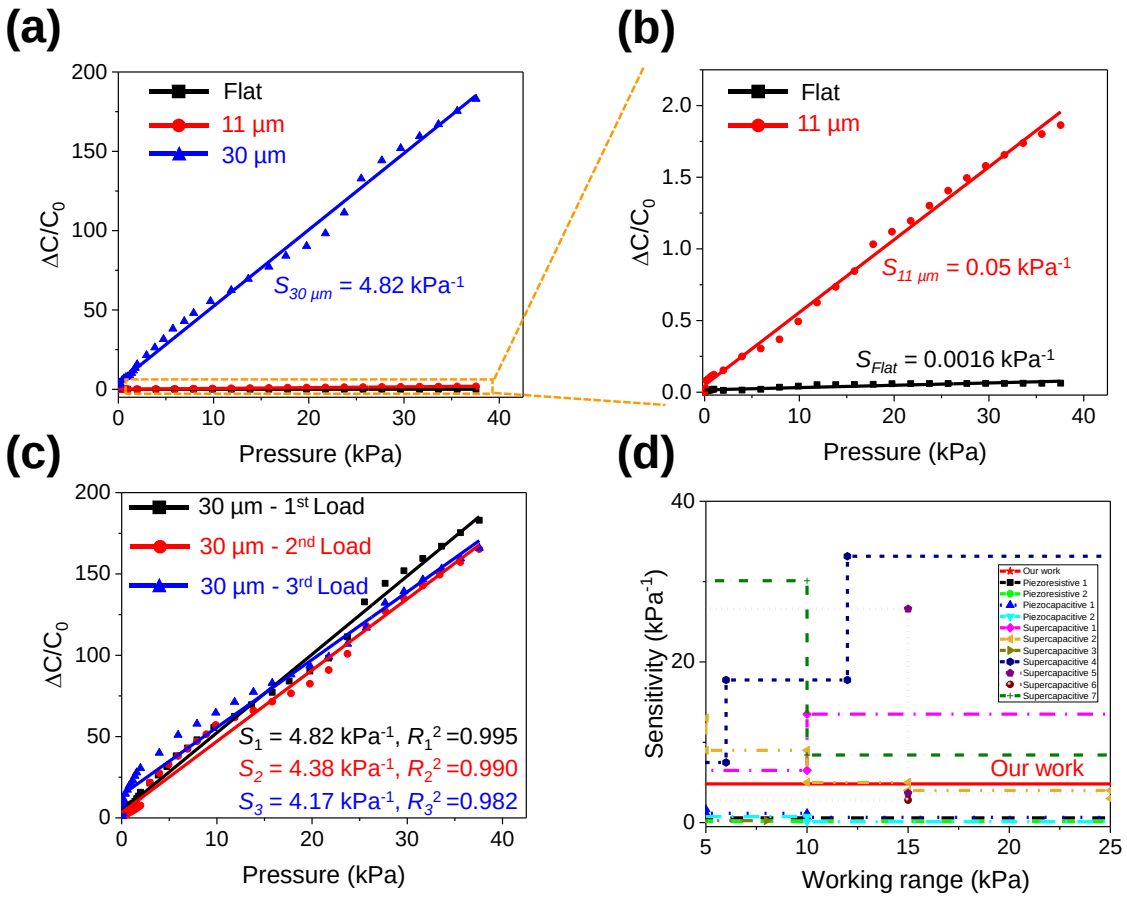

Figure 4.6. Sensitivity and dynamic range for our ITS. a) Comparison of the sensitivity between Au-coated flat-PDMS/IG/ITO/PET (flat), 11 μm MP-PDMS/IG/ITO/PET (11 μm - ITS), and 30 μm MP-PDMS/IG/ITO/PET (30 μm - ITS) from 0-38 kPa. b) The zoom-in of the sensitivity response for flat and 11 μm ITS devices. c) Sensitivity analysis for 3 different cycles of loading for 30 μm-ITS. d) Benchmark of the sensitivity and linearity of our 30 μm - ITS with other reported pressure sensors[136, 138, 142, 144, 146, 148, 151, 154-157] within normal BP range, from 5-25 kPa.

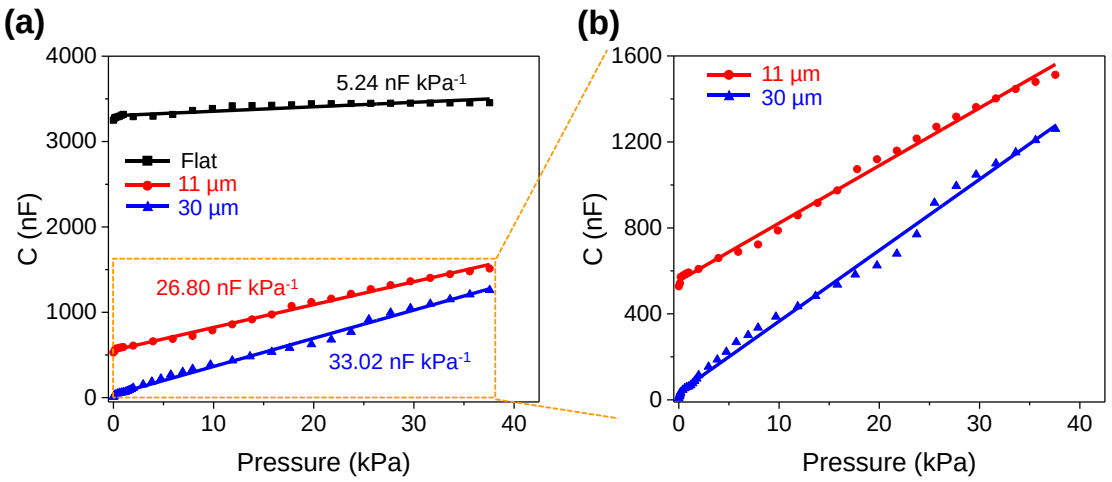

Figure 4.7. The measured capacitance-pressure response for our ITS. aCapacitance range comparison of flat, 11 µm, and 30 µm ITS and the linear fitting analysis. b) Zoom-in of the capacitance range for 11 µm, and 30 µm heights ITS.

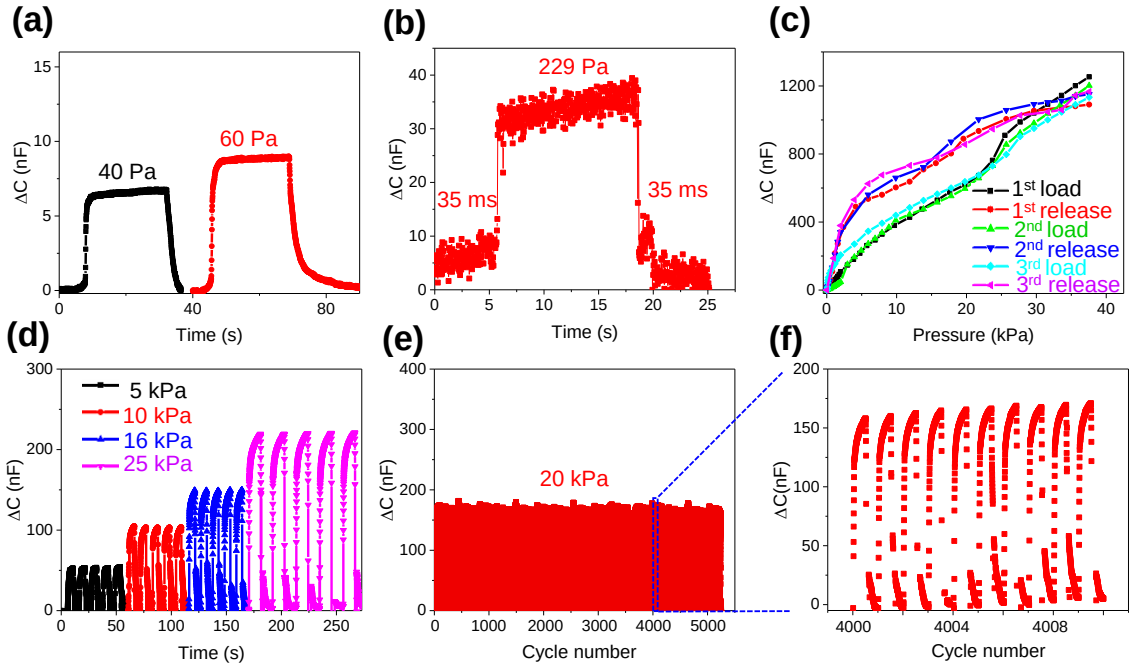

Figure 4.8. Sensing performance for 30 µm-ITS. a) Limit of detection as low as 40 Pa. b) Sensing response time for load (35 ms) and release (35 ms) of external pressure of 229 Pa. c) Hysteresis of 3 cycles of load and release of external pressure in the range 0-38 kPa. d) Dynamic pressure sensing response upon 5 consecutive external pressure pulses (0.1 Hz force alternating frequency) at different pressure levels. e) Endurance test of > 5000 cycles under load and release of external pressure 20 kPa (0.1 Hz force alternating frequency). f) Zoom-in of 10 cycles of load and release of external pressure 20 kPa.

Our 30 μm-ITS also exhibited a small limit of detection at 40 Pa (0.3 mmHg)(**Figure 4.8a**), which enables a sensitive response of our ITS in low pressure regions and a great potential of our ITS in electronic skin and human-machine interface applications.[133] Microengineering the elastic elastomer PDMS has been demonstrated to accelerate response time of the sensor since the voids in the microstructures help the elastomer to more quickly store and release energy reversibly and minimize the issues related to the viscoelastic behavior of the elastic polymer.[21] Our 30 μm-ITS responded to the applied pressure of 229 Pa in the milliseconds range (35 ms) (Figure 4.8b) due to the limit of the capacitance readout instrument sampling rate (~ 30 Hz). Although the response time of our ITS is not ideal, our ITS is still fast enough to detect BP fluctuations (normal heart rate is 60-100 beats/min) and reveal the important hemodynamic parameters such as arterial stiffness, which is extracted from the BP peak-to-peak timescale differences (normally ~ 0.2 s).[127, 219]

The PDMS elastomer has viscoelasticity and thus our ITS indicates a hysteresis loop when the applied compressive pressure loads and releases. Figure 4.8c shows the measured hysteresis behavior of our ITS upon 3 different cycles of load and release. Admittedly, there are certain sensing variations at fixed static pressure level, particularly at high pressure. These variations are most likely due to the increasing shear stress at the MP-PDMS and IG film interface under high pressure. Adding a lamination layer[141] or building an interlinked interface[220] have the potential to mitigate the sensing variations.

We applied different pressure levels (5 kPa, 10 kPa, 16 kPa, 25 kPa) at an external force alternating frequency of 0.1 Hz to our 30 μm-ITS to evaluate its response upon dynamic pressure (Figure 4.8d). We also observed a linear relationship between the capacitance change and the applied pressure, which means our ITS can easily be calibrated in the further developed BP sensing system. Durability is one essential parameter to evaluate the working lifetime of the sensor. After

we applied over 5000 cycles of dynamic pressure 20 kPa at 0.1 Hz force alternating frequency to our ITS (Figure 4.8e), our ITS still worked well although certain variations in maximum capacitance change did exist. Figure 4.8f shows a zoom-in of the 10 cycles of dynamic pressure loads and releases, where each cycle is clear and distinguishable, showing the successful sensing functionality of our ITS. We believe that the excellent sensor performance of our developed ITS could lead to a detection of real-time, high-fidelity BP waveform signals in a continuous and non-invasive way.

4.6 Arterial Pulse Monitoring

Arterial applanation tonometry relies on the skin-mounted pressure sensor to transduce the BP pressure from the applanated underlying artery.[117] **Figure 4.9a** demonstrates the working principle of the applanation tonometry, where a hold-down applanation pressure P_0 is applied to flatten the surface of the underlying artery. The usage of external applanation pressure decreases the intervening tissue damping effects and maximizes the amplitude of the detected pulse pressure.[128] An appropriate applanation pressure must be chose to flatten a smaller portion of the artery but not completely occlude the artery. As with the traditional cuff-based oscillometric device, the maximum arterial BP signal occurs where the applanation pressure is close to the mean arterial blood pressure in the human body (70-100 mmHg, i.e., 9-13 kPa).[117, 118, 128] We mounted our ITS on the skin surface with polyimide tape at two different body locations: upper arm and wrist, aiming at monitoring of brachial and radial arterial BP waveform signals. An aneroid sphygmomanometer, i.e., inflatable cuff, was wrapped around the tested arm or wrist to apply applanation pressure. Figure 4.9b indicates the measured brachial BP waveform under a P_0 of 80

mmHg for a 25-year-old adult, who was seated with the left upper arm and heart at the same height level. The inset shows images of the mounted ITS on the upper arm with and without external cuff. Figure 4.9c shows a zoom-in of two continuous brachial BP waveforms in the dashed box from Figure 4.9b, where the human heart rate can be calculated as 70 beats/min. This tested human heart rate is normal for a 25-year-old adult, whose resting heart rate is expected to be 60-100 beats/min.[116, 120] Figure 4.9d and 4.9e indicate the radial BP waveforms obtained by placing the ITS sensor at the left wrist of the same tested person, where a resting heart rate of 67 beats/min can be estimated. More importantly, from the zoom-in brachial and radial BP raw pulse waveforms shown in Figure 4.9c and 4.9e, two characteristic peaks P_1 and P_2 can be observed, as previously reported.[20, 127] These two peaks originate from the superposition of the incident blood wave ejected by the left ventricular contraction and the reflected wave from the periphery.[20] Two important hemodynamic parameters for arterial stiffness diagnosis, the augmentation index and time delay between the first two peaks, can be estimated from the magnitude and timescale of the two peaks $P_1(t_1)$ and $P_2(t_2)$. The artery augmentation index, defined as $AI_r = P_2 / P_1$, is estimated to be 58 % (left upper arm) and 66 % (left wrist); while the time delay, defined as $\Delta T_{DVP} = t_2 - t_1$, is estimated to be 300 ms (left upper arm) and 375 ms (left wrist). The BP waveform signals using our skin surface mounted ITS were weaker than the real intra-arterial BP values, due to the intervening tissues and body muscle. To transfer our tested BP waveforms into real-time BP pressure values, we need to do BP waveform scaling (Figure 4.9f) using correction functions or algorithms. In our future work, we will collaborate with other researchers to develop a BP scaling method so that a direct BP pressure can be obtained for the users. Overall, we can capture clear and distinguishable brachial and radial BP waveforms continuously, owing to the high-fidelity, high sensitivity and large dynamic ranges of our designed ITS.

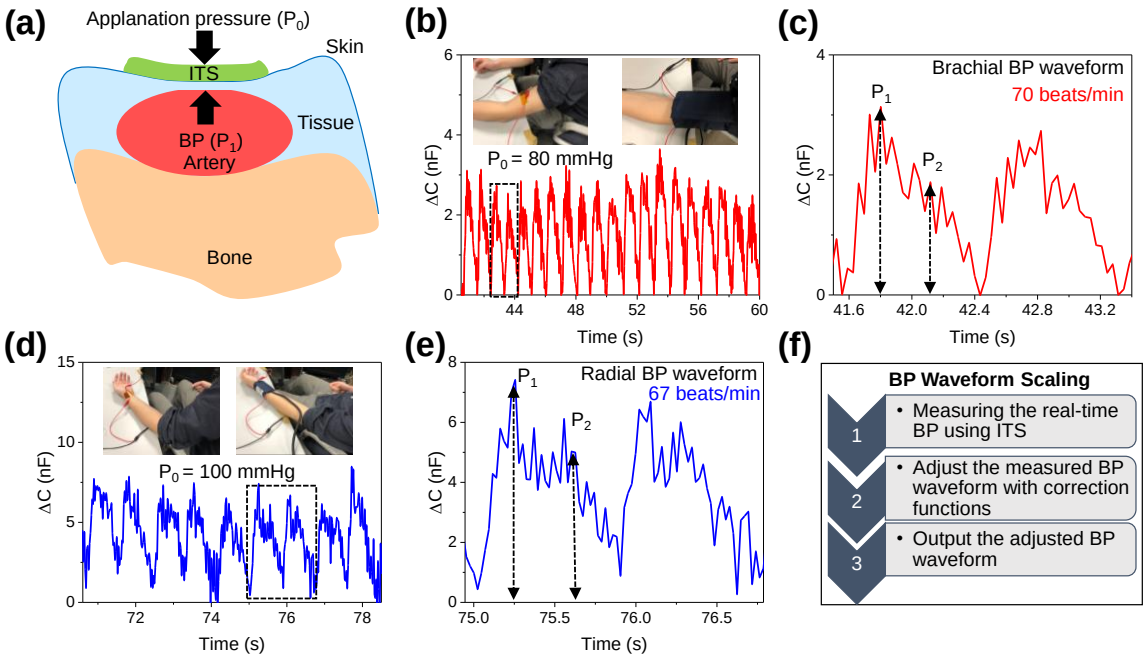

Figure 4.9. Real-time BP waveform monitoring at the arm and wrist using our 30 μm-ITS. a) The test principle of arterial applanation tonometry. b) Measured capacitance response vs. time when ITS is mounted at the left arm of the tested person under an applanation cuff pressure of 80 mmHg. c) Zoom-in of two brachial BP waveforms from the dashed box in panel b). d) Measured capacitance response vs. time when ITS is mounted at the left wrist of the tested person under an applanation cuff pressure of 100 mmHg. e) Zoom-in of two radial BP waveforms from the dashed box in panel d). f) Further steps of BP waveform scaling.

4.7 Conclusion

Our designed wearable ITS demonstrates the ability to non-invasively capture the continuous, real-time BP waveforms at the upper arm and wrist positions. Combining microengineering with iontronic sensing, our ITS offers high-fidelity piezocapacitive outputs with high sensitivity (4.82 kPa^{-1}), good linearity ($R^2 > 0.995$), and large dynamic ranges (up to 180%) over a broad working range (0-38 kPa) that can fully cover the normal BP range (5-25 kPa).

Moreover, our ITS exhibits a low limit of detection at 40 Pa, a fast response time (35 ms), and a good durability after over 5000 load/release cycles. Our work provides a feasible design for wearable sensors that could lead to real-time CNIBP monitoring and potential applications in electronic skin and human-machine interfaces.

5.0 Summary and Future Work

In summary, two major branches of solid-state iontronic devices have been explored, electrochemical synapses and supercapacitive pressure sensors, based on the electrochemical ion intercalation/deintercalation and EDL effects. Our developed iontronic devices exhibit great potential as artificial synapses for neuromorphic computing and pressure sensors for continuous non-invasive BP monitoring. Research outcomes of this dissertation include 5 peer-reviewed journal publications (4 first-authored).

We develop the first electrochemical synapses based on ternary TI $(Bi_{0.2}\,Sb_{0.8})_2Te_3$ with programmable spatio-temporal dynamics (both amplitude and time constant), suitable for implementing neuro-realistic ANNs. We demonstrate basic neuronal functions such as short-term and long-term plasticity as well as paired-pulse facilitation, utilizing the built-in temporal component in our BST synapse. The BST synapse shows good scaling potential, with a projected switching speed and energy at 100 ns and 28 aJ at nanoscale dimensions (~25 nm). Our work elucidates the fundamental electrical and ionic transport in electrochemically intercalated TI devices and develops an energy-efficient dynamic synapse that can potentially lead to the hardware acceleration of neuro-realistic ANNs which significantly improves the energy efficiency and cognitive capability of computing systems.

Moreover, we propose WO_3-based electrochemical synapses with a low programming voltage (0.2 V), fast programming speed (500 ns), high precision (1024 levels), and low variation, as well as a relatively linear and symmetric response. In addition, our dynamic synapses naturally exhibit both LTP and STP behaviors owing to the combined effects from charge transfer doping (via electrochemical redox reactions) and ionic gating (via EDL effects), which is desirable for

SNNs applications. We demonstrate various time-dependent synaptic functions such as pair-pulse facilitation and temporal filtering. Leveraging the spike-encoded timing information extracted from the short-term plasticity exponential decay behavior, we were able to build an SNN model to benchmark the pattern classification performance of our LiWES, which shows a large boost (128× improvement) in classification performance in highly time-dependent scenarios.

Lastly, we take full advantage of pure EDL effects in iontronics and develop a high-fidelity iontronic tonometric sensor (ITS) with high sensitivity (4.82 kPa^{-1}), high linearity ($R^2 > 0.995$) and a large dynamic range (up to 180%) within a broad working range of 0-38 kPa that can fully cover the normal BP range (5-25 kPa). By microengineering the contact electrodes that interface with the iontronic film into different micropyramid patterns (11 μm and 30 μm height), we can control the initial interfacial contact area and tune the sensitivity from 0.05 kPa^{-1} (11 μm) to 4.82 kPa^{-1} (30 μm), reaching ~ 100 × improvement. Benefiting from our design, our ITS demonstrates a low limit of detection at 40 Pa, a fast load response time (35 ms) and release time (35 ms), and a stable response after 5000 load/release cycles. We further explore the application of our ITS in monitoring real-time beat-to-beat BP by measuring the brachial and radial pulse waveforms, which can be used to recognize patients' hemodynamic status and reveal real-time BP levels. Our work provides a feasible design for a flexible pressure sensor with high sensitivity, high linearity, and a large dynamic range for real-time CNIBP monitoring.

Our future work can be summarized as the following: 1) exploring new solid-state electrolytes via low-cost fabrication methods to provide more flexible design solutions for our iontronic devices; 2) building a synaptic array based on our developed electrochemical synapses to move a step closer to truly brain-inspired neuromorphic hardware; 3) developing innovative neuromorphic circuitry and computation algorithms to fully implement the spatio-temporal

dynamics and cognitive capability of our developed electrochemical synapses; 4) scaling down the iontronic supercapacitive sensors and building a sensing array to more accurately capture the spatial distribution of blood vessels and detect stronger BP signals; and 5) exploring the possibility of combining our developed synapses and sensors into artificial afferent nerve systems.

Bibliography

[1] S. Z. Bisri, S. Shimizu, M. Nakano, Y. Iwasa, *Advanced Materials* **2017**, *29*, 1607054.

[2] J. Leger, M. Berggren, S. Carter, *Iontronics: Ionic carriers in organic electronic materials and devices*, CRC Press, Boca Raton, FL, USA **2016**.

[3] T. Arbring Sjöström, M. Berggren, E. O. Gabrielsson, P. Janson, D. J. Poxson, M. Seitanidou, D. T. Simon, *Advanced Materials Technologies* **2018**, *3*, 1700360.

[4] T. Li, K. Xiao, *Advanced Materials Technologies* **2022**, *n/a*, 2200205.

[5] A. Sood, A. D. Poletayev, D. A. Cogswell, P. M. Csernica, J. T. Mefford, D. Fraggedakis, M. F. Toney, A. M. Lindenberg, M. Z. Bazant, W. C. Chueh, *Nature Reviews Materials* **2021**, *6*, 847.

[6] J. Liang, *PhD Dissertation, University of Pittsburgh*, **2021**.

[7] Q. Wan, P. Zhang, Q. Shao, M. T. Sharbati, J. R. Erickson, K. L. Wang, F. Xiong, *APL Materials* **2019**, *7*, 101107.

[8] Q. Wan, M. T. Sharbati, J. R. Erickson, Y. Du, F. Xiong, *Advanced Materials Technologies* **2019**, *4*, 1900037.

[9] Q. Wan, P. Zhang, Q. Shao, M. T. Sharbati, J. R. Erickson, K. L. Wang, F. Xiong, presented at *2019 Device Research Conference (DRC)*, 23-26 June, **2019**.

[10] Q. Wan, M. Rasetto, M. T. Sharbati, J. R. Erickson, S. R. Velagala, M. T. Reilly, Y. Li, R. Benosman, F. Xiong, *Advanced Intelligent Systems* **2021**, *3*, 2100021.

[11] E. J. Fuller, F. E. Gabaly, F. Léonard, S. Agarwal, S. J. Plimpton, R. B. Jacobs-Gedrim, C. D. James, M. J. Marinella, A. A. Talin, *Advanced Materials* **2017**, *29*, 1604310.

[12] Y. van de Burgt, E. Lubberman, E. J. Fuller, S. T. Keene, G. C. Faria, S. Agarwal, M. J. Marinella, A. Alec Talin, A. Salleo, *Nature Materials* **2017**, *16*, 414.

[13] Y. Li, E. J. Fuller, S. Asapu, S. Agarwal, T. Kurita, J. J. Yang, A. A. Talin, *ACS Applied Materials & Interfaces* **2019**, *11*, 38982.

[14] M. T. Sharbati, Y. Du, J. Torres, N. D. Ardolino, M. Yun, F. Xiong, *Advanced Materials* **2018**, *30*, 1802353.

[15] M. T. Sharbati, S. Y. Cho, G. N. Tomaraei, Q. Wan, J. Schlea, M. Bedewy, F. Xiong, presented at *2019 Device Research Conference (DRC)*, 23-26 June **2019**.

[16] R. Waser, R. Dittmann, G. Staikov, K. Szot, *Advanced Materials* **2009**, *21*, 2632.

[17] B. Nie, S. Xing, J. D. Brandt, T. Pan, *Lab on a Chip* **2012**, *12*, 1110.

[18] Z. Zhu, R. Li, T. Pan, *Advanced Materials* **2018**, *30*, 1705122.

[19] N. Bai, L. Wang, Q. Wang, J. Deng, Y. Wang, P. Lu, J. Huang, G. Li, Y. Zhang, J. Yang, K. Xie, X. Zhao, C. F. Guo, *Nature Communications* **2020**, *11*, 209.

[20] G. Schwartz, B. C. K. Tee, J. Mei, A. L. Appleton, D. H. Kim, H. Wang, Z. Bao, *Nature Communications* **2013**, *4*, 1859.

[21] S. C. B. Mannsfeld, B. C. K. Tee, R. M. Stoltenberg, C. V. H. H. Chen, S. Barman, B. V. O. Muir, A. N. Sokolov, C. Reese, Z. Bao, *Nature Materials* **2010**, *9*, 859.

[22] Y.-C. Huang, Y. Liu, C. Ma, H.-C. Cheng, Q. He, H. Wu, C. Wang, C.-Y. Lin, Y. Huang, X. Duan, *Nature Electronics* **2020**, *3*, 59.

[23] K. H. Lee, M. S. Kang, S. Zhang, Y. Gu, T. P. Lodge, C. D. Frisbie, *Advanced Materials* **2012**, *24*, 4457.

[24] I. Boybat, M. Le Gallo, S. R. Nandakumar, T. Moraitis, T. Parnell, T. Tuma, B. Rajendran, Y. Leblebici, A. Sebastian, E. Eleftheriou, *Nature Communications* **2018**, *9*, 2514.

[25] K. Bourzac, *Nature* **2017**, *551*, 554.

[26] P. Huang, J. Kang, Y. Zhao, S. Chen, R. Han, Z. Zhou, Z. Chen, W. Ma, M. Li, L. Liu, X. Liu, *Advanced Materials* **2016**, *28*, 9758.

[27] M. S. Komar, *Automatic Control and Computer Sciences* **2017**, *51*, 701.

[28] G. Indiveri, S. Liu, *Proceedings of the IEEE* **2015**, *103*, 1379.

[29] M. Koziarski, B. Cyganek, *Integrated Computer-Aided Engineering* **2017**, *24*, 337.

[30] Z. Ansari, S. A. Seyyedsalehi, *Neural Computing and Applications* **2017**, *28*, 1177.

[31] J. Zhang, C. Zong, *IEEE Intelligent Systems* **2015**, *30*, 16.

[32] D. Silver, A. Huang, C. J. Maddison, A. Guez, L. Sifre, G. van den Driessche, J. Schrittwieser, I. Antonoglou, V. Panneershelvam, M. Lanctot, S. Dieleman, D. Grewe, J. Nham, N. Kalchbrenner, I. Sutskever, T. Lillicrap, M. Leach, K. Kavukcuoglu, T. Graepel, D. Hassabis, *Nature* **2016**, *529*, 484.

[33] G. W. Burr, R. M. Shelby, A. Sebastian, S. Kim, S. Kim, S. Sidler, K. Virwani, M. Ishii, P. Narayanan, A. Fumarola, L. L. Sanches, I. Boybat, M. Le Gallo, K. Moon, J. Woo, H. Hwang, Y. Leblebici, *Advances in Physics: X* **2017**, *2*, 89.

[34] D. Kuzum, S. Yu, H. S. Philip Wong, *Nanotechnology* **2013**, *24*, 382001.

[35] S. Kim, M. Ishii, S. Lewis, T. Perri, M. BrightSky, W. Kim, R. Jordan, G. W. Burr, N. Sosa, A. Ray, J. Han, C. Miller, K. Hosokawa, C. Lam, presented at *IEEE International Electron Devices Meeting (IEDM)*, 7-9 Dec., **2015**.

[36] Z. Dong, Z. Zhou, Z. Li, C. Liu, P. Huang, L. Liu, X. Liu, J. Kang, *IEEE Transactions on Electron Devices* **2019**, *66*, 793.

[37] B. Pérez-Sánchez, O. Fontenla-Romero, B. Guijarro-Berdiñas, *Artif. Intell. Rev.* **2018**, *49*, 281.

[38] P. Chen, X. Peng, S. Yu, presented at *2017 IEEE International Electron Devices Meeting (IEDM)*, 2-6 Dec., **2017**.

[39] A. L. Caterini, D. E. Chang, *Deep Neural Networks in a Mathematical Framework*, Springer, **2018**.

[40] S. Yu, *Neuro-inspired computing using resistive synaptic devices*, Springer, **2017**.

[41] A. Azizimazreah, Y. Gu, X. Gu, L. Chen, presented at *2018 IEEE International Conference on Networking, Architecture and Storage (NAS)*, 11-14 Oct., **2018**.

[42] Q. Yu, R. Yan, H. Tang, K. C. Tan, H. Li, *IEEE Transactions on Neural Networks and Learning Systems* **2016**, *27*, 621.

[43] M. Giulioni, X. Lagorce, F. Galluppi, R. B. Benosman, *Frontiers in Neuroscience* **2016**, *10*.

[44] H. Markram, W. Gerstner, P. J. Sjöström, *Frontiers in Synaptic Neuroscience* **2011**, *3*.

[45] S. Lowel, W. Singer, *Science* **1992**, *255*, 209.

[46] Y. Dan, M.-M. Poo, *Physiological Reviews* **2006**, *86*, 1033.

[47] M. T. Sharbati, Y. Du, J. Torres, N. D. Ardolino, M. Yun, F. Xiong, *Advanced Materials* **2018**, *30*, 1870273.

[48] D. S. Jeong, *Journal of Applied Physics* **2018**, *124*, 152002.

[49] F. Akopyan, J. Sawada, A. Cassidy, R. Alvarez-Icaza, J. Arthur, P. Merolla, N. Imam, Y. Nakamura, P. Datta, G. Nam, B. Taba, M. Beakes, B. Brezzo, J. B. Kuang, R. Manohar, W. P. Risk, B. Jackson, D. S. Modha, *IEEE Transactions on Computer-Aided Design of Integrated Circuits and Systems* **2015**, *34*, 1537.

[50] K. Boahen, *Computing in Science & Engineering* **2017**, *19*, 14.

[51] S. B. Furber, F. Galluppi, S. Temple, L. A. Plana, *Proceedings of the IEEE* **2014**, *102*, 652.

[52] A. D. Brown, J. E. Chad, R. Kamarudin, K. J. Dugan, S. B. Furber, *IEEE Transactions on Multi-Scale Computing Systems* **2018**, *4*, 450.

[53] S. R. Ovshinsky, *Physical Review Letters* **1968**, *21*, 1450.

[54] S. Lai, presented at *IEEE International Electron Devices Meeting 2003*, 8-10 Dec., **2003**.

[55] M. H. R. Lankhorst, B. W. S. M. M. Ketelaars, R. A. M. Wolters, *Nature Materials* **2005**, *4*, 347.

[56] J. H. Oh, J. H. Park, Y. S. Lim, H. S. Lim, Y. T. Oh, J. S. Kim, J. M. Shin, J. H. Park, Y. J. Song, K. C. Ryoo, D. W. Lim, S. S. Park, J. I. Kim, J. H. Kim, J. Yu, F. Yeung, C. W. Jeong, J. H. Kong, D. H. Kang, G. H. Koh, G. T. Jeong, H. S. Jeong, K. Kim, presented at *2006 International Electron Devices Meeting*, 11-13 Dec., **2006**.

[57] R. Bez, presented at *2009 IEEE International Electron Devices Meeting (IEDM)*, 7-9 Dec., **2009**.

[58] G. Servalli, presented at *2009 IEEE International Electron Devices Meeting (IEDM)*, 7-9 Dec. , **2009**.

[59] H. P. Wong, S. Raoux, S. Kim, J. Liang, J. P. Reifenberg, B. Rajendran, M. Asheghi, K. E. Goodson, *Proceedings of the IEEE* **2010**, *98*, 2201.

[60] S. R. Ovshinsky, *Journal of Non-Crystalline Solids* **1970**, *2*, 99.

[61] M. Wuttig, N. Yamada, *Nature Materials* **2007**, *6*, 824.

[62] N. Yamada, E. Ohno, K. Nishiuchi, N. Akahira, M. Takao, *Journal of Applied Physics* **1991**, *69*, 2849.

[63] T. Tuma, A. Pantazi, M. Le Gallo, A. Sebastian, E. Eleftheriou, *Nature Nanotechnology* **2016**, *11*, 693.

[64] J. Gasia, M. Martin, A. Solé, C. Barreneche, F. L. Cabeza, *Applied Sciences* **2017**, *7*.

[65] G. Nicolescu, I. O'Connor, C. Piguet, *Design technology for heterogeneous embedded systems*, Springer, **2012**.

[66] D. Kuzum, R. G. D. Jeyasingh, B. Lee, H. S. P. Wong, *Nano Letters* **2012**, *12*, 2179.

[67] C. D. Wright, P. Hosseini, J. A. V. Diosdado, *Advanced Functional Materials* **2013**, *23*, 2248.

[68] Y. Zhong, Y. Li, L. Xu, X. Miao, *physica status solidi (RRL)–Rapid Research Letters* **2015**, *9*, 414.

[69] A. Redaelli, D. Ielmini, A. L. Lacaita, F. Pellizzer, A. Pirovano, R. Bez, presented at *IEEE InternationalElectron Devices Meeting, 2005. IEDM Technical Digest.*, 5-5 Dec., **2005**.

[70] G. W. Burr, M. J. Breitwisch, M. Franceschini, D. Garetto, K. Gopalakrishnan, B. Jackson, B. Kurdi, C. Lam, L. A. Lastras, A. Padilla, B. Rajendran, S. Raoux, R. S. Shenoy, *Journal of Vacuum Science & Technology B* **2010**, *28*, 223.

[71] C. Ahn, B. Lee, R. G. D. Jeyasingh, M. Asheghi, G. A. M. Hurkx, K. E. Goodson, H. S. Philip Wong, *Journal of Applied Physics* **2011**, *110*, 114520.

[72] S. Braga, A. Cabrini, G. Torelli, *IEEE Transactions on Electron Devices* **2011**, *58*, 517.

[73] Y. Shi, L. Nguyen, S. Oh, X. Liu, F. Koushan, J. R. Jameson, D. Kuzum, *Nature Communications* **2018**, *9*, 5312.

[74] S. H. Jo, T. Chang, I. Ebong, B. B. Bhadviya, P. Mazumder, W. Lu, *Nano Letters* **2010**, *10*, 1297.

[75] M. N. Kozicki, P. Mira, M. Mitkova, *IEEE Transactions on Nanotechnology* **2005**, *4*, 331.

[76] X. Xu, H. Lv, H. Liu, Q. Luo, T. Gong, M. Wang, G. Wang, M. Zhang, Y. Li, Q. Liu, S. Long, M. Liu, *Nanoscale Research Letters* **2015**, *10*, 61.

[77] M. Prezioso, F. Merrikh-Bayat, B. D. Hoskins, G. C. Adam, K. K. Likharev, D. B. Strukov, *Nature* **2015**, *521*, 61.

[78] R. Berdan, E. Vasilaki, A. Khiat, G. Indiveri, A. Serb, T. Prodromakis, *Scientific Reports* **2016**, *6*, 18639.

[79] S. Yu, Y. Wu, R. Jeyasingh, D. Kuzum, H. P. Wong, *IEEE Transactions on Electron Devices* **2011**, *58*, 2729.

[80] S. Ambrogio, S. Balatti, F. Nardi, S. Facchinetti, D. Ielmini, *Nanotechnology* **2013**, *24*, 384012.

[81] S. Ambrogio, S. Balatti, V. Milo, R. Carboni, Z. Wang, A. Calderoni, N. Ramaswamy, D. Ielmini, *IEEE Transactions on Electron Devices* **2016**, *63*, 1508.

[82] G. Pedretti, V. Milo, S. Ambrogio, R. Carboni, S. Bianchi, A. Calderoni, N. Ramaswamy, A. S. Spinelli, D. Ielmini, *Scientific Reports* **2017**, *7*, 5288.

[83] T. Chang, S.-H. Jo, W. Lu, *ACS Nano* **2011**, *5*, 7669.

[84] R. Yang, K. Terabe, Y. Yao, T. Tsuruoka, T. Hasegawa, J. K. Gimzewski, M. Aono, *Nanotechnology* **2013**, *24*, 384003.

[85] S. Kim, S. Choi, W. Lu, *ACS Nano* **2014**, *8*, 2369.

[86] S. Kim, C. Du, P. Sheridan, W. Ma, S. Choi, W. D. Lu, *Nano Letters* **2015**, *15*, 2203.

[87] H. P. Wong, H. Lee, S. Yu, Y. Chen, Y. Wu, P. Chen, B. Lee, F. T. Chen, M. Tsai, *Proceedings of the IEEE* **2012**, *100*, 1951.

[88] R. Waser, R. Dittmann, G. Staikov, K. Szot, *Advanced Materials* **2009**, *21*, 2632.

[89] P. Huang, Y. Wang, H. Li, B. Gao, B. Chen, F. Zhang, L. Zeng, G. Du, J. Kang, X. Liu, *IEEE Transactions on Nanotechnology* **2014**, *13*, 1127.

[90] J. Jang, S. Park, G. W. Burr, H. Hwang, Y. Jeong, *IEEE Electron Device Letters* **2015**, *36*, 457.

[91] S. Park, M. Chu, J. Kim, J. Noh, M. Jeon, B. Hun Lee, H. Hwang, B. Lee, B.-g. Lee, *Scientific Reports* **2015**, *5*, 10123.

[92] Y.-F. Wang, Y.-C. Lin, I. T. Wang, T.-P. Lin, T.-H. Hou, *Scientific Reports* **2015**, *5*, 10150.

[93] J. Zhu, Y. Yang, R. Jia, Z. Liang, W. Zhu, Z. U. Rehman, L. Bao, X. Zhang, Y. Cai, L. Song, R. Huang, *Advanced Materials* **2018**, *30*, 1800195.

[94] D. Ielmini, A. L. Lacaita, *Materials Today* **2011**, *14*, 600.

[95] C. Gong, D. Ruzmetov, A. Pearse, D. Ma, J. N. Munday, G. Rubloff, A. A. Talin, M. S. Leite, *ACS Applied Materials & Interfaces* **2015**, *7*, 26007.

[96] N. J. Dudney, *Materials Science and Engineering: B* **2005**, *116*, 245.

[97] K. F. Mak, J. Shan, *Nature Photonics* **2016**, *10*, 216.

[98] X. Duan, C. Wang, A. Pan, R. Yu, X. Duan, *Chemical Society Reviews* **2015**, *44*, 8859.

[99] C. Muratore, V. Varshney, J. J. Gengler, J. J. Hu, J. E. Bultman, T. M. Smith, P. J. Shamberger, B. Qiu, X. Ruan, A. K. Roy, A. A. Voevodin, *Applied Physics Letters* **2013**, *102*, 081604.

[100] Q. H. Wang, K. Kalantar-Zadeh, A. Kis, J. N. Coleman, M. S. Strano, *Nature Nanotechnology* **2012**, *7*, 699.

[101] F. Xia, H. Wang, Y. Jia, *Nature Communications* **2014**, *5*, 4458.

[102] M.-H. Bae, Z. Li, Z. Aksamija, P. N. Martin, F. Xiong, Z.-Y. Ong, I. Knezevic, E. Pop, *Nature Communications* **2013**, *4*, 1734.

[103] C. Chiritescu, D. G. Cahill, N. Nguyen, D. Johnson, A. Bodapati, P. Keblinski, P. Zschack, *Science* **2007**, *315*, 351.

[104] A. A. Soluyanov, D. Gresch, Z. Wang, Q. Wu, M. Troyer, X. Dai, B. A. Bernevig, *Nature* **2015**, *527*, 495.

[105] I. G. Lezama, A. Arora, A. Ubaldini, C. Barreteau, E. Giannini, M. Potemski, A. F. Morpurgo, *Nano Letters* **2015**, *15*, 2336.

[106] W. Jin, P.-C. Yeh, N. Zaki, D. Zhang, J. T. Sadowski, A. Al-Mahboob, A. M. van der Zande, D. A. Chenet, J. I. Dadap, I. P. Herman, P. Sutter, J. Hone, R. M. Osgood, *Physical Review Letters* **2013**, *111*, 106801.

[107] H. Tian, W. Mi, X.-F. Wang, H. Zhao, Q.-Y. Xie, C. Li, Y.-X. Li, Y. Yang, T.-L. Ren, *Nano Letters* **2015**, *15*, 8013.

[108] Y. Shi, X. Liang, B. Yuan, V. Chen, H. Li, F. Hui, Z. Yu, F. Yuan, E. Pop, H. S. P. Wong, M. Lanza, *Nature Electronics* **2018**, *1*, 458.

[109] K. Ba, W. Jiang, J. Cheng, J. Bao, N. Xuan, Y. Sun, B. Liu, A. Xie, S. Wu, Z. Sun, *Scientific Reports* **2017**, *7*, 45584.

[110] M. Xu, T. Liang, M. Shi, H. Chen, *Chemical Reviews* **2013**, *113*, 3766.

[111] V. Tran, R. Soklaski, Y. Liang, L. Yang, *Physical Review B* **2014**, *89*, 235319.

[112] L. Sun, Y. Zhang, G. Hwang, J. Jiang, D. Kim, Y. A. Eshete, R. Zhao, H. Yang, *Nano Letters* **2018**, *18*, 3229.

[113] A. J. Arnold, A. Razavieh, J. R. Nasr, D. S. Schulman, C. M. Eichfeld, S. Das, *ACS Nano* **2017**, *11*, 3110.

[114] H. Tian, Q. Guo, Y. Xie, H. Zhao, C. Li, J. J. Cha, F. Xia, H. Wang, *Advanced Materials* **2016**, *28*, 4991.

[115] H. Tian, X. Cao, Y. Xie, X. Yan, A. Kostelec, D. DiMarzio, C. Chang, L.-D. Zhao, W. Wu, J. Tice, J. J. Cha, J. Guo, H. Wang, *ACS Nano* **2017**, *11*, 7156.

[116] G. Ogedegbe, T. Pickering, *Cardiology Clinics* **2010**, *28*, 571.

[117] K. Lakhal, S. Ehrmann, T. Boulain, *CHEST* **2018**, *153*, 1023.

[118] A. S. Meidert, B. Saugel, *Frontiers in Medicine* **2018**, *4*, 231.

[119] S. Rastegar, H. GholamHosseini, A. Lowe, *Physical and Engineering Sciences in Medicine* **2020**, *43*, 11.

[120] B. Saugel, K. Kouz, A. S. Meidert, L. Schulte-Uentrop, S. Romagnoli, *Critical Care* **2020**, *24*, 172.

[121] J. Kim, A. Salvatore Giovanni, H. Araki, M. Chiarelli Antonio, Z. Xie, A. Banks, X. Sheng, Y. Liu, W. Lee Jung, K.-I. Jang, Y. Heo Seung, K. Cho, H. Luo, B. Zimmerman, J. Kim, L. Yan, X. Feng, S. Xu, M. Fabiani, G. Gratton, Y. Huang, U. Paik, A. Rogers John, *Science Advances* **2016**, *2*, e1600418.

[122] T. Yokota, P. Zalar, M. Kaltenbrunner, H. Jinno, N. Matsuhisa, H. Kitanosako, Y. Tachibana, W. Yukita, M. Koizumi, T. Someya, *Science Advances* **2016**, *2*, e1501856.

[123] K. Lakhal, M. Martin, S. Faiz, S. Ehrmann, Y. Blanloeil, K. Asehnoune, B. Rozec, T. Boulain, *Anesthesia & Analgesia* **2016**, *123*.

[124] P. Schramm, I. Tzanova, T. Gööck, F. Hagen, I. Schmidtmann, K. Engelhard, G. Pestel, *Journal of Neurosurgical Anesthesiology* **2017**, *29*.

[125] F. Balzer, M. Habicher, M. Sander, J. Sterr, S. Scholz, A. Feldheiser, M. Müller, C. Perka, S. Treskatsch, *The Journal of international medical research* **2016**, *44*, 832.

[126] A. Chandrasekhar, C.-S. Kim, M. Naji, K. Natarajan, J.-O. Hahn, R. Mukkamala, *Science Translational Medicine* **2018**, *10*, eaap8674.

[127] C. Dagdeviren, Y. Su, P. Joe, R. Yona, Y. Liu, Y.-S. Kim, Y. Huang, A. R. Damadoran, J. Xia, L. W. Martin, Y. Huang, J. A. Rogers, *Nature Communications* **2014**, *5*, 4496.

[128] R. Dueck, O. Goedje, P. Clopton, *Journal of Clinical Monitoring and Computing* **2012**, *26*, 75.

[129] W.-Q. Lin, H.-H. Wu, C.-S. Su, J.-T. Yang, J.-R. Xiao, Y.-P. Cai, X.-Z. Wu, G.-Z. Chen, *Journal of Neurosurgical Anesthesiology* **2017**, *29*.

[130] C. Wang, X. Li, H. Hu, L. Zhang, Z. Huang, M. Lin, Z. Zhang, Z. Yin, B. Huang, H. Gong, S. Bhaskaran, Y. Gu, M. Makihata, Y. Guo, Y. Lei, Y. Chen, C. Wang, Y. Li, T. Zhang, Z. Chen, A. P. Pisano, L. Zhang, Q. Zhou, S. Xu, *Nature Biomedical Engineering* **2018**, *2*, 687.

[131] G. L. Pressman, P. M. Newgard, *IEEE Transactions on Bio-medical Electronics* **1963**, *10*, 73.

[132] O. Kemmotsu, M. Ueda, H. Otsuka, T. Yamamura, Dean C. Winter, Joseph S. Eckerle, *Anesthesiology* **1991**, *75*, 333.

[133] Y. Huang, X. Fan, S.-C. Chen, N. Zhao, *Advanced Functional Materials* **2019**, *29*, 1808509.

[134] H. Miyashita, *Current Hypertension Reviews* **2012**, *8*, 80.

[135] K. Meng, J. Chen, X. Li, Y. Wu, W. Fan, Z. Zhou, Q. He, X. Wang, X. Fan, Y. Zhang, J. Yang, Z. L. Wang, *Advanced Functional Materials* **2019**, *29*, 1806388.

[136] N. Luo, W. Dai, C. Li, Z. Zhou, L. Lu, C. C. Y. Poon, S.-C. Chen, Y. Zhang, N. Zhao, *Advanced Functional Materials* **2016**, *26*, 1178.

[137] N. Luo, Y. Huang, J. Liu, S.-C. Chen, C. P. Wong, N. Zhao, *Advanced Materials* **2017**, *29*, 1702675.

[138] K. Kim, J. Choi, Y. Jeong, I. Cho, M. Kim, S. Kim, Y. Oh, I. Park, *Advanced Healthcare Materials* **2019**, *8*, 1900978.

[139] Z. Zhang, X. Gui, Q. Hu, L. Yang, R. Yang, B. Huang, B.-R. Yang, Z. Tang, *Advanced Electronic Materials* **2021**, *7*, 2100174.

[140] B. C. K. Tee, A. Chortos, R. R. Dunn, G. Schwartz, E. Eason, Z. Bao, *Advanced Functional Materials* **2014**, *24*, 5427.

[141] S. R. A. Ruth, L. Beker, H. Tran, V. R. Feig, N. Matsuhisa, Z. Bao, *Advanced Functional Materials* **2020**, *30*, 1903100.

[142] K.-H. Ha, W. Zhang, H. Jang, S. Kang, L. Wang, P. Tan, H. Hwang, N. Lu, *Advanced Materials* **2021**, *33*, 2103320.

[143] J. Kim, E.-F. Chou, J. Le, S. Wong, M. Chu, M. Khine, *Advanced Healthcare Materials* **2019**, *8*, 1900109.

[144] J. C. Yang, J.-O. Kim, J. Oh, S. Y. Kwon, J. Y. Sim, D. W. Kim, H. B. Choi, S. Park, *ACS Applied Materials & Interfaces* **2019**, *11*, 19472.

[145] Y. Chang, L. Wang, R. Li, Z. Zhang, Q. Wang, J. Yang, C. F. Guo, T. Pan, *Advanced Materials* **2021**, *33*, 2003464.

[146] Q. Lin, J. Huang, J. Yang, Y. Huang, Y. Zhang, Y. Wang, J. Zhang, Y. Wang, L. Yuan, M. Cai, X. Hou, W. Zhang, Y. Zhou, S. G. Chen, C. F. Guo, *Advanced Healthcare Materials* **2020**, *9*, 2001023.

[147] N. Bai, L. Wang, Y. Xue, Y. Wang, X. Hou, G. Li, Y. Zhang, M. Cai, L. Zhao, F. Guan, X. Wei, C. F. Guo, *ACS Nano* **2022**, *16*, 4338.

[148] S. H. Cho, S. W. Lee, S. Yu, H. Kim, S. Chang, D. Kang, I. Hwang, H. S. Kang, B. Jeong, E. H. Kim, S. M. Cho, K. L. Kim, H. Lee, W. Shim, C. Park, *ACS Applied Materials & Interfaces* **2017**, *9*, 10128.

[149] K. Keum, J. Eom, J. H. Lee, J. S. Heo, S. K. Park, Y.-H. Kim, *Nano Energy* **2021**, *79*, 105479.

[150] S. Sharma, A. Chhetry, S. Zhang, H. Yoon, C. Park, H. Kim, M. Sharifuzzaman, X. Hui, J. Y. Park, *ACS Nano* **2021**, *15*, 4380.

[151] S. G. Yoon, B. J. Park, S. T. Chang, *ACS Applied Materials & Interfaces* **2017**, *9*, 36206.

[152] R. Li, Y. Si, Z. Zhu, Y. Guo, Y. Zhang, N. Pan, G. Sun, T. Pan, *Advanced Materials* **2017**, *29*, 1700253.

[153] J. S. Kim, S. C. Lee, J. Hwang, E. Lee, K. Cho, S.-J. Kim, D. H. Kim, W. H. Lee, *Advanced Functional Materials* **2020**, *30*, 1908993.

[154] P. Lu, L. Wang, P. Zhu, J. Huang, Y. Wang, N. Bai, Y. Wang, G. Li, J. Yang, K. Xie, J. Zhang, B. Yu, Y. Dai, C. F. Guo, *Science Bulletin* **2021**, *66*, 1091.

[155] Y. Zheng, T. Lin, N. Zhao, C. Huang, W. Chen, G. Xue, Y. Wang, C. Teng, X. Wang, D. Zhou, *Nano Energy* **2021**, *85*, 106013.

[156] P. Zhu, H. Du, X. Hou, P. Lu, L. Wang, J. Huang, N. Bai, Z. Wu, N. X. Fang, C. F. Guo, *Nature Communications* **2021**, *12*, 4731.

[157] Z. Qiu, Y. Wan, W. Zhou, J. Yang, J. Yang, J. Huang, J. Zhang, Q. Liu, S. Huang, N. Bai, Z. Wu, W. Hong, H. Wang, C. F. Guo, *Advanced Functional Materials* **2018**, *28*, 1802343.

[158] A. Chhetry, J. Kim, H. Yoon, J. Y. Park, *ACS Applied Materials & Interfaces* **2019**, *11*, 3438.

[159] J. Zhang, C.-Z. Chang, Z. Zhang, J. Wen, X. Feng, K. Li, M. Liu, K. He, L. Wang, X. Chen, Q.-K. Xue, X. Ma, Y. Wang, *Nature Communications* **2011**, *2*, 574.

[160] X. Leng, J. Pereiro, J. Strle, A. T. Bollinger, I. Božović, *APL Materials* **2015**, *3*, 096102.

[161] Y. Li, *Solid State Ionics* **2018**, *323*, 142.

[162] H. Matsui, T. Nakamura, Y. Kobayashi, M. Tabuchi, Y. Yamada, *Journal of Power Sources* **2010**, *195*, 6879.

[163] S. K. Fullerton-Shirey, J. K. Maranas, *Macromolecules* **2009**, *42*, 2142.

[164] H. Yuan, H. Wang, Y. Cui, *Accounts of Chemical Research* **2015**, *48*, 81.

[165] D. Kong, W. Dang, J. J. Cha, H. Li, S. Meister, H. Peng, Z. Liu, Y. Cui, *Nano Letters* **2010**, *10*, 2245.

[166] R. D. Shannon, *Acta Crystallographica Section A* **1976**, *32*, 751.

[167] J. Zhang, J. Sun, Y. Li, F. Shi, Y. Cui, *Nano Letters* **2017**, *17*, 1741.

[168] M. Lang, L. He, X. Kou, P. Upadhyaya, Y. Fan, H. Chu, Y. Jiang, J. H. Bardarson, W. Jiang, E. S. Choi, Y. Wang, N.-C. Yeh, J. Moore, K. L. Wang, *Nano Letters* **2013**, *13*, 48.

[169] C. Weyrich, M. Drögeler, J. Kampmeier, M. Eschbach, G. Mussler, T. Merzenich, T. Stoica, I. E. Batov, J. Schubert, L. Plucinski, B. Beschoten, C. M. Schneider, C. Stampfer, D. Grützmacher, T. Schäpers, *Journal of Physics: Condensed Matter* **2016**, *28*, 495501.

[170] D. Kong, Y. Chen, J. J. Cha, Q. Zhang, J. G. Analytis, K. Lai, Z. Liu, S. S. Hong, K. J. Koski, S.-K. Mo, Z. Hussain, I. R. Fisher, Z.-X. Shen, Y. Cui, *Nature Nanotechnology* **2011**, *6*, 705.

[171] F. Xiong, H. Wang, X. Liu, J. Sun, M. Brongersma, E. Pop, Y. Cui, *Nano Letters* **2015**, *15*, 6777.

[172] H. Yang, S. W. Kim, M. Chhowalla, Y. H. Lee, *Nature Physics* **2017**, *13*, 931.

[173] W. Bao, J. Wan, X. Han, X. Cai, H. Zhu, D. Kim, D. Ma, Y. Xu, J. N. Munday, H. D. Drew, M. S. Fuhrer, L. Hu, *Nature Communications* **2014**, *5*, 4224.

[174] X. Zhu, D. Li, X. Liang, W. D. Lu, *Nature Materials* **2019**, *18*, 141.

[175] Y. Guo, J. Zhou, Y. Liu, X. Zhou, F. Yao, C. Tan, J. Wu, L. Lin, K. Liu, Z. Liu, H. Peng, *Advanced Materials* **2017**, *29*, 1703424.

[176] R. S. Zucker, W. G. Regehr, *Annual Review of Physiology* **2002**, *64*, 355.

[177] C.-S. Yang, D.-S. Shang, N. Liu, E. J. Fuller, S. Agrawal, A. A. Talin, Y.-Q. Li, B.-G. Shen, Y. Sun, *Advanced Functional Materials* **2018**, *28*, 1804170.

[178] J. T. Yang, C. Ge, J. Y. Du, H. Y. Huang, M. He, C. Wang, H. B. Lu, G. Z. Yang, K. J. Jin, *Advanced Materials* **2018**, *30*, 1801548.

[179] Q. Wan, M. T. Sharbati, J. R. Erickson, Y. Du, F. Xiong, *Adv. Mater. Technol.* **2019**, *4*, 1900037.

[180] T. Gokmen, Y. Vlasov, *Front. Neurosci.* **2016**, *10*, 333.

[181] C.-L. Tsai, F. Xiong, E. Pop, M. Shim, *ACS Nano* **2013**, *7*, 5360.

[182] F. Xiong, A. D. Liao, D. Estrada, E. Pop, *Science* **2011**, *332*, 568.

[183] P. Chen, X. Peng, S. Yu, *IEEE Transactions on Computer-Aided Design of Integrated Circuits and Systems* **2018**, *37*, 3067.

[184] Y. LeCun, L. Bottou, Y. Bengio, P. Haffner, *Proceedings of the IEEE* **1998**, *86*, 2278.

[185] E. J. Fuller, S. T. Keene, A. Melianas, Z. Wang, S. Agarwal, Y. Li, Y. Tuchman, C. D. James, M. J. Marinella, J. J. Yang, A. Salleo, A. A. Talin, *Science* **2019**, *364*, 570.

[186] H. Zheng, J. Z. Ou, M. S. Strano, R. B. Kaner, A. Mitchell, K. Kalantar-zadeh, *Advanced Functional Materials* **2011**, *21*, 2175.

[187] J.-t. Yang, C. Ma, C. Ge, Q.-h. Zhang, J.-y. Du, J.-k. Li, H.-y. Huang, M. He, C. Wang, S. Meng, L. Gu, H.-b. Lu, G.-z. Yang, K.-j. Jin, *Journal of Materials Chemistry C* **2017**, *5*, 11694.

[188] Q. Zhong, J. R. Dahn, K. Colbow, *Physical Review B* **1992**, *46*, 2554.

[189] A. Hjelm, C. G. Granqvist, J. M. Wills, *Physical Review B* **1996**, *54*, 2436.

[190] S.-H. Lee, M. J. Seong, H. M. Cheong, E. Ozkan, E. C. Tracy, S. K. Deb, *Solid State Ionics* **2003**, *156*, 447.

[191] P. M. Wu, S. Ishii, K. Tanabe, K. Munakata, R. H. Hammond, K. Tokiwa, T. H. Geballe, M. R. Beasley, *Applied Physics Letters* **2015**, *106*, 042602.

[192] K. Yoshimatsu, T. Soma, A. Ohtomo, *Applied Physics Express* **2016**, *9*, 075802.

[193] S. Nishihaya, M. Uchida, Y. Kozuka, Y. Iwasa, M. Kawasaki, S. Nishihaya, M. Uchida, Y. Kozuka, Y. Iwasa, M. Kawasaki, Y. Iwasa, M. Kawasaki, *ACS Applied Materials & Interfaces* **2016**, *8*, 22330.

[194] X. Leng, J. Pereiro, J. Strle, G. Dubuis, A. T. Bollinger, A. Gozar, J. Wu, N. Litombe, C. Panagopoulos, D. Pavuna, I. Božović, *npj Quantum Materials* **2017**, *2*, 35.

[195] G. Cristiano, M. Giordano, S. Ambrogio, L. P. Romero, C. Cheng, P. Narayanan, H. Tsai, R. M. Shelby, G. W. Burr, *Journal of Applied Physics* **2018**, *124*, 151901.

[196] J.-T. Yang, C. Ge, J.-Y. Du, H.-Y. Huang, M. He, C. Wang, H.-B. Lu, G.-Z. Yang, K.-J. Jin, *Advanced Materials* **2018**, *30*, 1801548.

[197] J. Tang, D. Bishop, S. Kim, M. Copel, T. Gokmen, T. Todorov, S. Shin, K. Lee, P. Solomon, K. Chan, W. Haensch, J. Rozen, presented at *2018 IEEE International Electron Devices Meeting (IEDM)*, San Francisco, CA, USA, 1-5 December, **2018**.

[198] S. Kim, T. Todorov, M. Onen, T. Gokmen, D. Bishop, P. Solomon, K. Lee, M. Copel, D. B. Farmer, J. A. Ott, T. Ando, H. Miyazoe, V. Narayanan, J. Rozen, presented at *2019 IEEE International Electron Devices Meeting (IEDM)*, San Francisco, CA, USA, 7-11 December, **2019**.

[199] R.-T. Wen, C. G. Granqvist, G. A. Niklasson, *Nature Materials* **2015**, *14*, 996.

[200] F. La Mantia, C. D. Wessells, H. D. Deshazer, Y. Cui, *Electrochemistry Communications* **2013**, *31*, 141.

[201] H. Xu, S. Fathipour, E. W. Kinder, A. C. Seabaugh, S. K. Fullerton-Shirey, *ACS Nano* **2015**, *9*, 4900.

[202] S. Poongodi, P. S. Kumar, Y. Masuda, D. Mangalaraj, N. Ponpandian, C. Viswanathan, S. Ramakrishna, *RSC Advances* **2015**, *5*, 96416.

[203] V. I. Shapovalov, A. E. Lapshin, A. G. Gagarin, L. P. Efimenko, *Glass Physics and Chemistry* **2014**, *40*, 553.

[204] H. Sakamoto, T. Ariyoshi, N. Kimpara, K. Sugao, I. Taiko, K. Takikawa, D. Asanuma, S. Namiki, K. Hirose, *Nature Neuroscience* **2018**, *21*, 41.

[205] N. K. Upadhyay, S. Joshi, J. J. Yang, *Science China Information Sciences* **2016**, *59*, 061404.

[206] Y. LeCun, Y. Bengio, G. Hinton, *Nature* **2015**, *521*, 436.

[207] H. Anwar, X. Li, D. Bucher, F. Nadim, *Current Opinion in Neurobiology* **2017**, *43*, 71.

[208] K. Roy, A. Jaiswal, P. Panda, *Nature* **2019**, *575*, 607.

[209] K. Xu, M. M. Islam, D. Guzman, A. C. Seabaugh, A. Strachan, S. K. Fullerton-Shirey, *ACS Applied Materials & Interfaces* **2018**, *10*, 43166.

[210] A. Melianas, T. J. Quill, G. LeCroy, Y. Tuchman, H. v. Loo, S. T. Keene, A. Giovannitti, H. R. Lee, I. P. Maria, I. McCulloch, A. Salleo, *Science Advances* **2020**, *6*, eabb2958.

[211] E. S. Fortune, G. J. Rose, *Trends in Neurosciences* **2001**, *24*, 381.

[212] L. Q. Zhu, C. J. Wan, L. Q. Guo, Y. Shi, Q. Wan, *Nature Communications* **2014**, *5*, 3158.

[213] X. Lagorce, G. Orchard, F. Galluppi, B. E. Shi, R. B. Benosman, *IEEE Transactions on Pattern Analysis and Machine Intelligence* **2017**, *39*, 1346.

[214] H. Akolkar, C. Meyer, X. Clady, O. Marre, C. Bartolozzi, S. Panzeri, R. Benosman, *Neural Computation* **2015**, *27*, 561.

[215] Y. Mi, X. Lin, S. Wu, *Frontiers in Computational Neuroscience* **2016**, *10*.

[216] L. Li, Y. Mi, W. Zhang, D.-H. Wang, S. Wu, *Frontiers in Computational Neuroscience* **2018**, *12*.

[217] D. Buonomano, T. Carvalho, *Frontiers in Integrative Neuroscience* **2011**, *5*.

[218] H. Helmholtz, *Annalen der Physik* **1853**, *165*, 211.

[219] C.-H. Chen, C.-T. Ting, A. Nussbacher, E. Nevo, D. A. Kass, P. Pak, S.-P. Wang, M.-S. Chang, F. C. P. Yin, *Hypertension* **1996**, *27*, 168.

[220] Y. Zhang, J. Yang, X. Hou, G. Li, L. Wang, N. Bai, M. Cai, L. Zhao, Y. Wang, J. Zhang, K. Chen, X. Wu, C. Yang, Y. Dai, Z. Zhang, C. F. Guo, *Nature Communications* **2022**, *13*, 1317.